

Computer Simulation Study of Ventricular Fibrillation based on Whole-Heart Model

Yi Zheng

A DISSERTATION
SUBMITTED IN PARTIAL FULFILLMENT OF THE REQUIREMENTS
FOR THE DEGREE OF DOCTOR OF PHILOSOPHY
IN COMPUTER SCIENCE AND ENGINEERING

Graduate Department of Computer Systems

The University of Aizu

2015



© Copyright by Yi Zheng 2015

All Rights Reserved

The dissertation titled

*Computer Simulation Study of Ventricular Fibrillation based on
Whole-Heart Model*

by

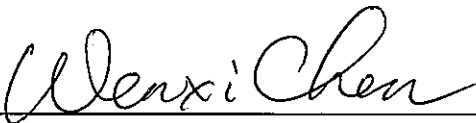

Yi Zheng

was reviewed and approved by:

Main referee

Professor

Wenxi Chen

Professor

Tuan D. Pham

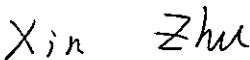

Associate Professor

Yasuhiro Hisada

Associate Professor

Xin Zhu

Contents

Contents	I
List of Figures	V
List of Tables.....	IX
Abstract	XI
List of Publications	XIII
Chapter 1 Introduction	1
1.1 Background	1
1.2 The human heart.....	3
1.3 Reentry and hypotheses of ventricular fibrillation	10
1.4 Simulation of arrhythmias on whole-heart models	15
1.5 Layout of the dissertation	16
Chapter 2 The whole-heart models	19
2.1 Introduction	19
2.2 Heart models of different scales	20
2.2.1 The single-cell model.....	20
2.2.2 The cell-network model	21
2.2.3 The whole-heart model	24
2.3 The Wei–Harumi whole-heart model	25
2.3.1 A general description of the Wei–Harumi model	26
2.3.2 Electrophysiological parameters	27
2.3.3 Anisotropic property	30
2.3.4 Propagation strategy.....	33
2.3.5 Anisotropic cardiac source.....	34
2.3.6 Calculation of surface ECG potential distribution.....	37
2.4 Studies based on the Wei–Harumi whole-heart model.....	39

Chapter 3 Effect of Action Potential Duration Restitution Slope on the Vulnerability to Ventricular Fibrillation Induction	41
3.1 Background and research target	41
3.2 Electrophysiological parameters used in the model	42
3.3 VF-induction method	44
3.4 Quantity of minimal stimuli required to induce VF	45
3.5 Discussion and conclusions.....	46
Chapter 4 Effects of Ventricular Fibrillation Induction Configurations on Induced Ventricular Fibrillation Organizations	49
4.1 Ventricular fibrillation induction protocols	49
4.2 Model settings and VF-induction configurations	50
4.2.1 VF-induction protocols and sites	50
4.2.2 APD and CV restitution	51
4.3 Results of induction by different configurations	52
4.4 Induction configurations and VF patterns	55
4.5 The induction configurations and the probability of inductions	56
4.6 Summary and conclusions.....	56
Chapter 5 Effects of Cardiac Restitutions on Ventricular Fibrillation	59
5.1 Mechanisms of ventricular fibrillation revisiting	59
5.2 Simulation method	60
5.2.1 Electrophysiological settings	61
5.2.2 The effective refractory period	63
5.2.3 Models with different restitutions	64
5.2.4 VF induction	65
5.2.5 Measurements of analysis	65
5.3 Results of induced VF in different models.....	66
5.3.1 Effects of APDR in the time-invariant models	66
5.3.2 Effect of CVR in the time-invariant models	69

5.3.3	Effect of heterogeneity in the time-invariant models	71
5.3.4	Evolution of VF in the time-variant model	72
5.4	Discussion	75
5.4.1	Effects of restitution on VF dynamics	75
5.4.2	Effects of restitution changes and heterogeneity on VF changes	77
5.4.3	The feasibility of using a rule-based model for the current study ...	78
5.5	Summary and conclusions.....	78
Chapter 6	Effects of Action Potential Duration Gradients on the Genesis of the Concordant T wave	79
6.1	Background	79
6.1.1	T wave and APD dispersion.....	79
6.1.2	Researches on mechanisms of concordant T wave	80
6.2	Electrophysiological settings.....	81
6.2.1	The APD gradient in the transmural dimension.....	81
6.2.2	The APD gradients in other dimensions	83
6.2.3	The APD of different model cells	83
6.2.4	Models with different gradients	84
6.3	Analysis of the simulation results	85
6.3.1	Simulation results of Models 1 and 2	85
6.3.2	Simulation results of Model 3.....	86
6.3.3	Simulation results of Model 4.....	87
6.3.4	Simulation results of Model 5.....	88
6.3.5	Optimized combinations of gradient in different dimensions.....	89
6.4	Discussion	91
6.4.1	The transmural gradient in the heart	91
6.4.2	Roles of the apicobasal, interventricular and anteroposterior gradients.....	92
6.4.3	The necessity of including the anteroposterior gradient	93

6.4.4 Comparing simulation results with clinical studies	94
6.5 Conclusions	94
Chapter 7 Conclusions	95
7.1 Contributions of this dissertation	95
7.2 Limitations and and future work	96
Acknowledgements.....	99
References.....	101

List of Figures

Figure 1.1 Trends in death rates for leading causes of death from 1947 to 2008 in Japan	1
Figure 1.2 The location and structure of the heart	4
Figure 1.3 Four images of a canine ventricular myocyte	4
Figure 1.4 An illustration of the electrical conduction system of the heart	5
Figure 1.5 An action potential generated by a simulation of a human ventricular epicardial cell model	7
Figure 1.6 A general scheme of human ventricular myocyte representing the major membrane ionic currents mediating the ventricular action potential	8
Figure 1.7 The PQRST complex and its relevant electrical activities	9
Figure 1.8 The mechanism of reentry formation and simultaneously exited reentrant circuits.....	11
Figure 1.9 Relationship between APDR slope and APD dynamics.....	13
Figure 2.1 Hierarchy of electrophysiological cardiac models of different scales.....	19
Figure 2.2 The logo of the Cellular Open Resource	21
Figure 2.3 Forms of reentry in cell-network models of different dimensions	23
Figure 2.4 Spatial configuration of model cells in an inclined 3D coordinate system with equal axial angles of 60°	26
Figure 2.5 Definition of the action potential of a model cell and illustration of its related parameters	28
Figure 2.6 A phase response curve used in simulating PVC	29
Figure 2.7 A strip of bigeminy ECG simulated from a heart model with a left ventricle located ectopic focus.....	30
Figure 2.8 One horizontal cross section showing the layered structure	31
Figure 2.9 Rotating fiber directions at three representative layers and a sketch showing	

the relationship between fiber plane and fiber plane direction	32
Figure 2.10 Three snapshots of epicardial transmembrane potentials distributions during a sinus rhythm.....	35
Figure 2.11 An example of the transmembrane potential of an epicardial model cell.	36
Figure 2.12 The heart–torso model	37
Figure 2.13 The simulated body surface potential maps (BSPM) of a sinus rhythm and its ECG.....	39
Figure 3.1 An endocardial APDR derived from ten Tusscher’s cellular model.....	42
Figure 3.2 Location of the VF-induction ectopy	45
Figure 3.3 Lead II ECG of sinus rhythm and VF-like rhythm.....	46
Figure 3.4 Insufficient ectopic stimuli led to failure of VF induction.....	46
Figure 4.1 An illustration of VF-induction sites	51
Figure 4.2 A representative ECG strip showing that S1S2 protocol failed to induce VF	53
Figure 4.3 A representative ECG strip showing induced unsustainable VF	53
Figure 4.4 ECG waveforms and spectra of four induced VF episodes.....	54
Figure 5.1 The APDR and CVR curves adopted	62
Figure 5.2 An illustration of consecutive simulated action potentials triggered by repetitive extrastimuli	63
Figure 5.3 Illustrations of VF dynamics in models with different APDR	68
Figure 5.4 ECG characteristics of VF induced in the homogeneous models	70
Figure 5.5 The behavior of VF induced in the heterogeneous models	72
Figure 5.6 The simulation of restitution changes.....	73
Figure 5.7 Situation of a modified “third stage” that reduces the excitability and heterogenizes the APDR	74
Figure 6.1 Schematics of gradients in different dimensions.....	82
Figure 6.2 The simulated ECG using Models 1 and 2 and the clinical ECG.	85
Figure 6.3 The simulated T waves using Model 3	86

Figure 6.4 The simulated T waves using Model 487

Figure 6.5 The simulated T waves using Model 588

Figure 6.6 The simulated T waves using Models 6 and 7 and the clinical T wave.89

Figure 6.7 The APD distribution in Model 791

List of Tables

Table 3.1 Parameters of piecewise restitution.....	44
Table 4.1 Parameters of exponential restitution.....	52
Table 4.2 Overview of the induction results	52
Table 5.1 Restitution settings of defined time-invariant models	64
Table 6.1 The gradient settings of models	84
Table 6.2 The ratios of simulated T-wave amplitudes to clinical values	90

Abstract

Mechanisms of ventricular fibrillation (VF) remain poorly understood. The “restitution hypothesis” is considered as a promising one that may lead to a breakthrough in understanding VF. It was hypothesized that VF organization was associated with action potential duration (APD) restitution and conduction velocity (CV) restitution based on animal experiments by Wu *et al.* Although this hypothesis was verified by simulations on a cardiac tissue slab, it is obviously necessary to further investigate it with computer simulations on whole-heart models.

However, so far few simulations have been done to study the effects of synergy of APD restitution (APDR) and CV restitution (CVR) on VF organization. In this dissertation, different diastolic-interval-dependent APDR and CVR settings were incorporated into the Wei–Harumi whole-heart model and VF was induced to check its responses to alternations of the restitution configurations.

Because a virtual heart does not have spontaneous VF, we have to induce VF before we study VF dynamics. Hence we first studied the relationship between cardiac vulnerability to VF induction and APDR slope to check the feasibility of inducing VF in the Wei–Harumi model with diastolic-interval-dependent APDR. Simulation results suggested that a steeper APDR slope was related with a higher VF-induction risk.

Secondly, we investigated the effects of VF-induction configuration by inducing VF at different heart sites with different induction protocols, and found that the VF organization was neither correlated with induction protocols nor induction sites.

As the major work of this dissertation, we carefully studied effects of synergy of the APDR and CVR on VF dynamics. The conversion from multiple-wavelet VF to ventricular tachycardia (VT) and the degeneration from VT to mother-rotor VF were both successfully simulated in the Wei–Harumi whole-heart model. Through analyses

of simulation outcomes, we concluded that it is likely that the conventional VF mechanisms can all be explained by the restitution mechanism. In addition, this simulation work supports the hypothesis that the synergy between the APDR (both its slope and heterogeneity) and CVR contributes to the transitions between multiple-wavelet and mother-rotor VF mechanisms.

T wave is important for studying VF mechanism. We obtained some interesting findings concerning the relationship between APD dispersion and the T wave, and based on these findings we proposed a hypothesis that the anteroposterior APD gradient contributes to the T-wave genesis.

The major contributions made by this dissertation are summarized below:

- a) Our work demonstrated that a steeper APDR slope is related to a higher VF-induction risk.
- b) Our simulations suggested that VF-induction methods and sites had little influence on VF patterns, which were simply manifestations of different intrinsic electrophysiological characteristics.
- c) Our work supported the hypothesis that both APDR (its slope and heterogeneity) and CVR contributes to the transitions between multiple-wavelet VF and mother-rotor VF. It is likely that both VF mechanisms can be explained by the restitution mechanism.
- d) Through simulations, we hypothesized that the anteroposterior APD gradient was an essential component in accounting for the concordant T wave.

List of Publications

1. **Yi Zheng**, Daming Wei, Xin Zhu, Wenxi Chen, Koji Fukuda and Hiroaki Shimokawa. “Ventricular fibrillation mechanisms and cardiac restitutions: An investigation by simulation study on whole-heart model”, *Computers in Biology and Medicine*, in press, published online on July 24th, 2014, Elsevier, 8 pages.
(DOI: <http://dx.doi.org/10.1016/j.compbiomed.2014.06.014>)
2. **Yi Zheng**, Daming Wei, Zuxiang Fang, and Xin Zhu, “Influences of Sites and Protocols on Inducing Ventricular Fibrillation: a Computer Simulation Study”, *Proceedings of 32nd Annual International Conference of the IEEE Engineering in Medicine and Biology Society*, August 31 – September 4, 2010, Buenos Aires, Argentina, pp 2005-2008. (EI: 20110113553681)
(DOI: <http://dx.doi.org/10.1109/IEMBS.2010.5627858>)
3. **Yi Zheng**, Daming Wei, Zuxiang Fang, “Steeper Action Potential Duration Restitution Slope Increases Risk of Ventricular Fibrillation: A Simulation Study”, *Proceedings of the 4th International Conference on Bioinformatics and Biomedical Engineering*, June 18 – 20, 2010, Chengdu, China, Paper ID:1011178. , CDROM, 4 pages. (EI: 20103613207038)
(DOI: 10.1109/ICBBE.2010.5515680)

Chapter 1 Introduction

1.1 Background

Sudden cardiac death (SCD) is a major clinical and public health problem in many countries [1]. A widely accepted concept of the SCD is an unexpected death within an hour from the sign of symptoms when the death is witnessed, or within a day of being seen alive and well when it is unwitnessed [2]. It annually claims over 300,000 lives in the United State alone [3]. In Japan, heart diseases have been the second main cause of death in the 21st century (see Figure 1.1 [4]), and killed 181,928 people in 2008 [4] among whom 60,382 died of SCD (in Japanese, it is called “pokkuri”) [5]. It is generally thought that most SCD result from ventricular fibrillation (VF) [3, 6], the most malignant arrhythmia. According to an authoritative report on SCD in 2010 [7], although the incident of VF as the causative rhythm disturbance has dramatically declined recently, it is still one of the most common killers responsible for SCD.

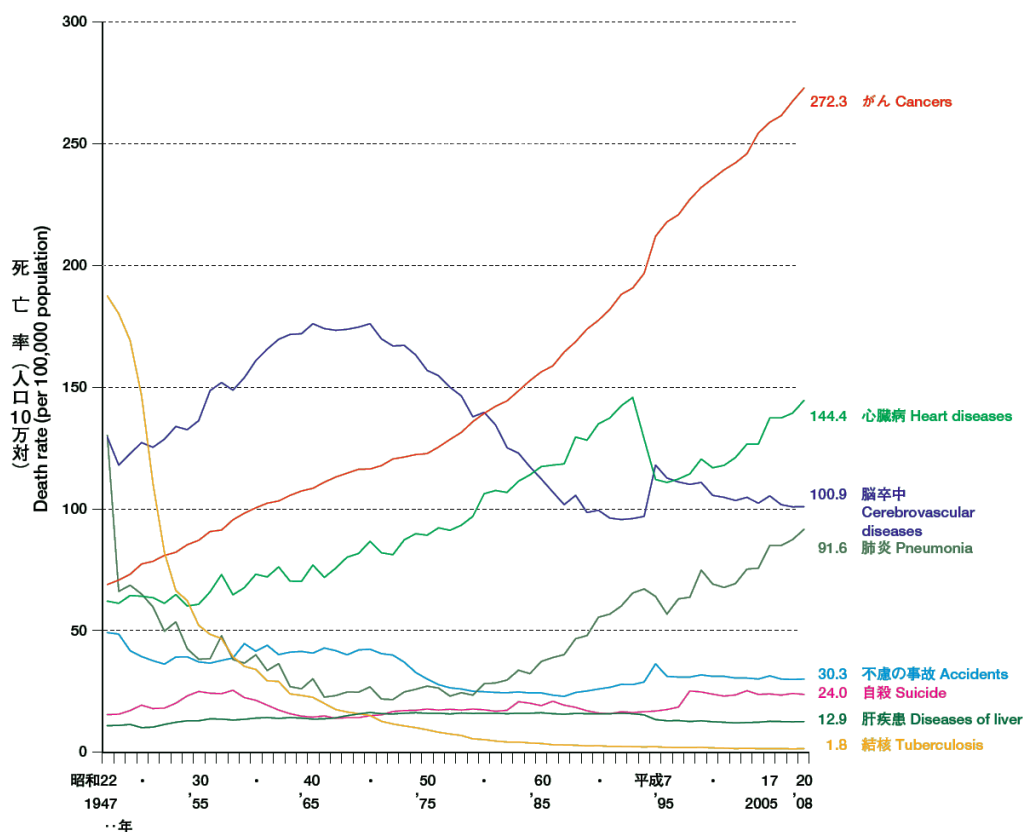


Figure 1.1 Trends in death rates for leading causes of death from 1947 to 2008 in Japan [4].

VF is a "turbulent, disorganized electrical activity of the heart in such a way that the recorded electrocardiographic deflections continuously change in shape, magnitude and direction" [8], whereby normal cardiac electrical propagation is severely disrupted, with consequent inability of myocardium to contract accordantly, and this disorganized activity deprives the heart of pumping function. If this deadly phenomenon is not remedied promptly, death usually ensues in a short time. This disease was firstly described by Erichsen as early as 1842 [9], yet knowledge about its underlying mechanisms remains incomplete [10] and naturally has been the topic of intense research for a long time [11].

Computer modeling and simulation are fruits of synergy between increasing availability of detailed experimental data and high performance computation. They greatly facilitate investigating various aspects of the heart functions and dysfunctions [12] and have become important techniques in electrophysiological and electrocardiographic studies [13]. In this dissertation, the model is defined as the heart model, and the simulation refers to the study run on heart models that attempts to reproduce experimental or clinical cardiac activities.

Every heart model is merely an abstract (or simplified) picture of the true cardiac anatomy and electrophysiology, and each simulation is only an approximation of the electrical activity ongoing in the real heart. This is because regardless of the dramatic development of computing hardware following the Moore's Law, the heart is still too complicated to be described and understood taking all virtually infinite substructures, interactions and effects into account.

Nevertheless, computer simulation is an effective tool complement to experimental studies and human trials because of several obvious advantages. First, studies on computer are economic and handy; while experiments or trials require a lot of resources and are restricted by practical and ethical constraints [14]. Second, simulation studies are free of noises and complications of data acquisition because values of all variables are known at all locations throughout the simulation domain [15]. Third, simulations can provide panoramic three-dimensional (3D) vision of intramural cardiac excitation propagation; while mapping techniques now available

are normally confined to the epicardium [16], endocardium [17] or both [18]. Although several advents of novel technologies, like the panoramic epicardial mapping [19], the 3D transmural electrode-array [20] and the transmural optrodes [21], have greatly facilitated and improved the understanding of VF organizations, resolutions of these technologies are still disappointing. Thus, mathematical simulation is considered as a useful technique for investigating electrical activities of the heart [22] including VF [15].

Roles of computer simulation in heart research include but are not limited to understanding cardiac mechanics, mechanisms of arrhythmias, mechanisms of defibrillation, improving diagnostic tools by solving forward and inverse problems of electrocardiography [12] as well as testing electrocardiological hypotheses. Besides, computer simulations can be applied for educational purposes [23].

1.2 The human heart

The heart is one of the most delicate and vital organs in the human body. It is located largely to the left of the midline in the chest cavity (see Figure 1.2A [24]). It consists of four chambers that are enclosed by thick, muscular walls (see Figure 1.2B [25]): the right atrium (RA), the left atrium (LA), the right ventricle (RV) and the left ventricle (LV). The oxygen-depleted blood from the body enters the RA through the vena cave, and then exits to the RV. From here blood is propelled into the pulmonary circulation for exchanging oxygen. After the oxygenation process, the blood returns back to the LA through the pulmonary veins, and later fills the LV from which fresh blood is ejected to the systemic circulation through the aorta. In this manner, the blood continuously runs inside blood vessels, delivers oxygen and nutrients to all body tissues, and transports waste products away from the same tissues. The heart restlessly pumps blood at a rate sufficient to facilitate these transportations, exchange and homeostatic roles of the circulatory system [26].

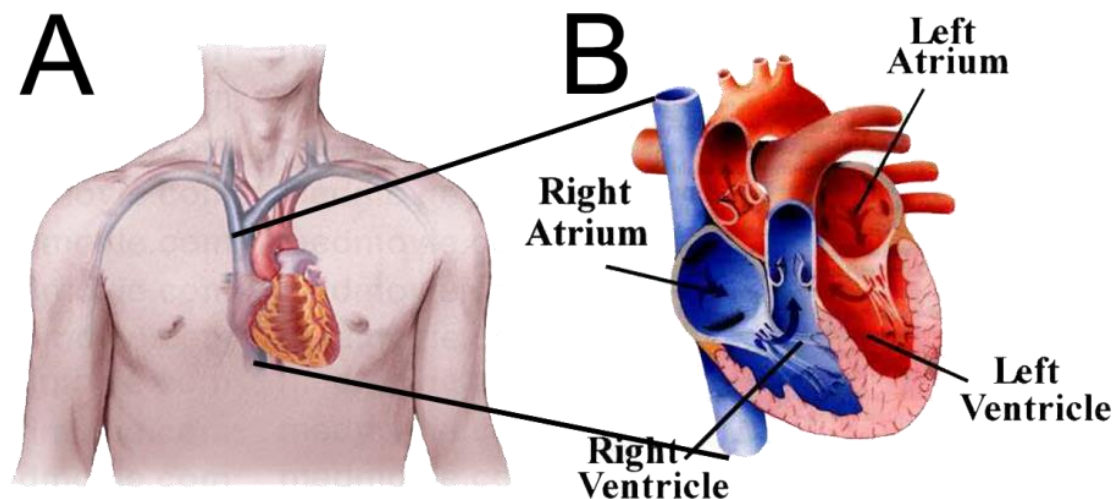


Figure 1.2 The location [24] and structure of the heart [25]. (A): an illustration of the heart position inside the human chest cavity; (B): the four-chamber structure of the heart from a posterior-anterior view.

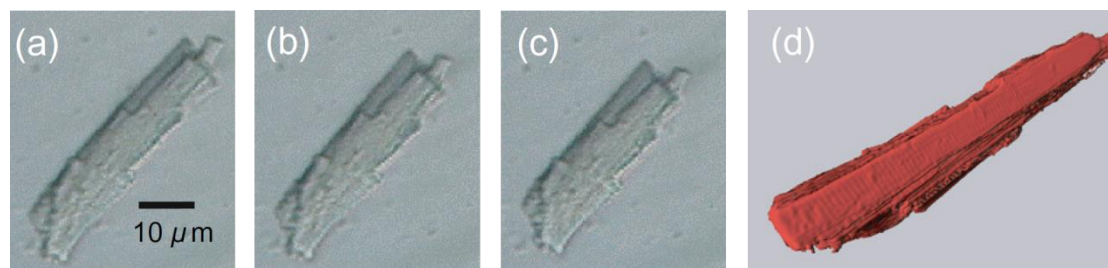


Figure 1.3 Four images of a canine ventricular myocyte [15]. (a)-(c): three consecutive snapshots displaying the contraction of the myocyte in response to an external electrical stimulation; (d): a 3D reconstructed canine ventricular myocyte.

Normal and efficient blood pumping depends on not only adequate time for ventricular filling and ejection, but also that heart musculature contracts in a coordinated manner [27]. The heart is a muscle made up of millions of myocytes [28] (see Figure 1.3(d) for an illustration of a canine ventricular myocyte). Because the contraction of individual myocyte is triggered by electrical excitation called the cardiac electromechanical effect (also known as the excitation-contraction coupling [29], see Figure 1.3(a)-(c)), a coordinated cardiac contraction requires different parts of the heart be electrically excited in a specific sequence [27].

The heart has a special conduction network (see Figure 1.4) to achieve this sequential propagation. A group of specialized cells in the RA form the sinoatrial node (SAN) that acts as the pacemaker, spontaneously firing approximately from 70 to 200 times per minute depending on physiological state of the body. Its impulse is

conveyed to myocytes of both atria, and soon atrial mechanical contraction follows which pushes blood into ventricles. At the same time, the excitation from SAN reaches the atrioventricular (AV) node via the Bachmann's bundle. AV node is the only electrical connection between ventricles and atria under nonpathological situation, where the excitation wave delays for tens of milliseconds to give the blood time to flow into the ventricles, and subsequently travels to the His bundle (HB), the left and right bundle branches (BB), and the Purkinje fibers (PKJ). Thanks to branches of the His–Purkinje system which radiate throughout the ventricular endocardial tissue and their high conduction speed, different ventricular parts contract almost simultaneously, and provide blood enough strength to flow inside the systemic and pulmonary circulation systems. After the blood ejection, both ventricles relax to get ready for the next systole. This periodic process happens during every normal heart beat.

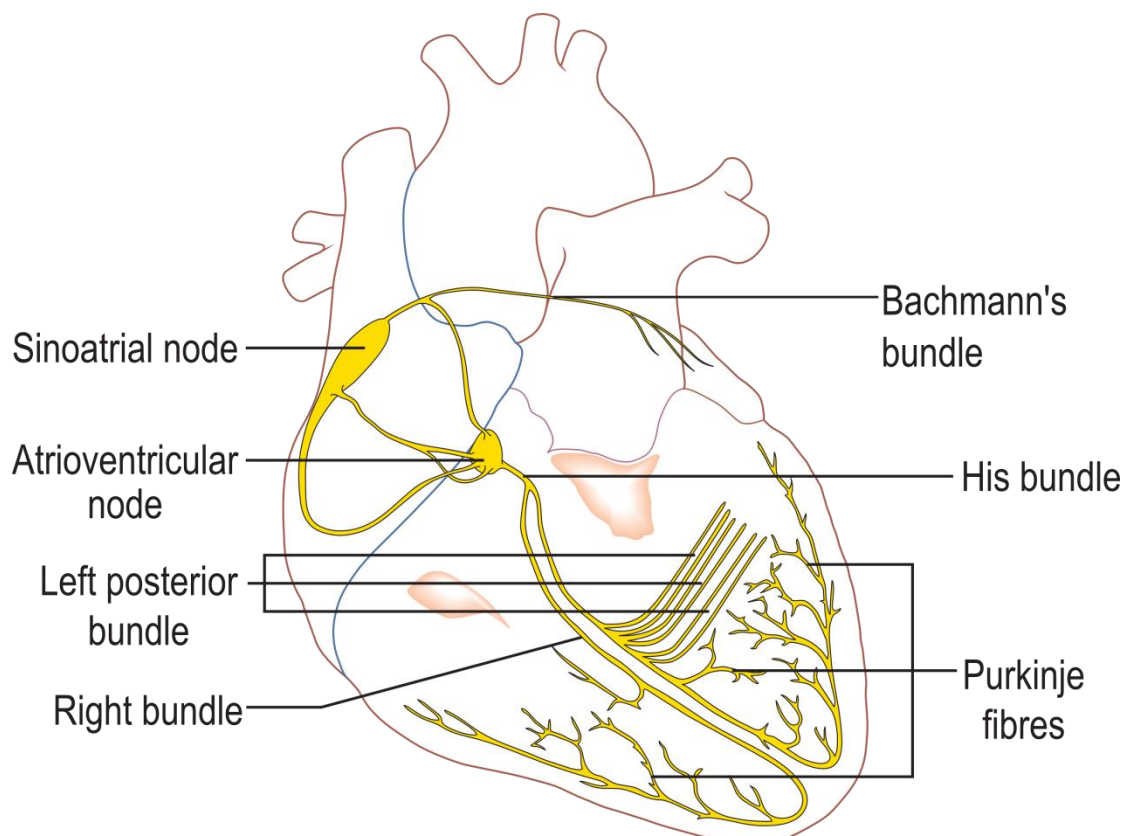


Figure 1.4 An illustration of the electrical conduction system of the heart (created by Madhero88, and licensed under the CC-BY-SA-3.0). A graphical representation of the electrical conduction system of the heart showing the sinoatrial node, Bachmann's bundle, atrioventricular node, His bundle, right bundle, left bundle and Purkinje fibers.

The excitation of the individual cardiac cell technically refers to the depolarization of transmembrane potential. The cell membrane acts as a barrier that prevents the cytoplasm from mixing with extracellular solutions. During the resting state, the differences in membrane permeability to various ions and the resultant differences between intracellular and extracellular ionic concentrations create a situation that the inside potential of the cell is negative relative to the outside potential. Thus the resting state is also noted as the polarized state with a negative transmembrane potential. Upon an electrical stimulation that brings the transmembrane potential to its firing threshold, individual cardiac cell exhibits a highly nonlinear response known as the action potential during which a surge in intracellular calcium initiates the mechanical contraction as mentioned above. The action potential obeys all-or-none law that as long as the stimulus brings the transmembrane potential of a cell above the threshold potential, the cell will give a complete response; otherwise it does not respond at all. In other words, stronger stimulus does not produce larger action potentials.

The action potential has 5 phases from 0 to 4 (see Figure 1.5). Phase 4 is the said resting state which the cell remains in until it is stimulated by an electrical impulse (usually offered by an adjacent cell). Phase 0 follows phase 4 once the transmembrane voltage is raised to a threshold potential. It is the upstroke when transmembrane potential rapidly changes from a negative value to a positive one, better known as the depolarization phase. The abrupt influx of extracellular sodium ion (Na^+) into the cell resulting from opening of the fast Na^+ channels is responsible for the depolarization. Phase 1 occurs with the inactivation of the fast Na^+ channels. This small downward deflection in the action potential is a manifestation of the transient flow of outward potassium (K^+) and inward chloride ions (Cl^-). Phase 1 is followed by phase 2, also called the “plateau” phase because during this period there is little change in transmembrane potential. Its formation and maintenance are primarily owing to the fine-tuned balance between inward calcium ions (Ca^{2+}) and outward K^+ . During phase 3, the transmembrane potential gradually decreases towards the resting potential corresponding to a net outward current due to Ca^{2+} channels closing and K^+ channels remaining, which breaks the balance of charge interplay sustained in the phase 2. In

other words, the membrane gradually becomes polarized again, and thus this period is termed as the “repolarization” phase. As soon as the repolarization phase is over, the cell restores the phase 4 associated with diastole of the heart chambers and waits for the next action potential. The active channels during different phases are shown in the Figure 1.6 (the blue and red pathways). For more information about the mechanism of action potential, please refer to other elaborately written tutorial [30] and review [31].

Once an action potential is triggered, there is a period of time during which a new intact action potential cannot be initiated regardless of external stimulation amplitude. This period is termed as the absolute refractory period (ARP, see Figure 1.5 for its span). As soon as the ARP ends, the relative refractory period (RRP) begins when the cell only responds to those stimuli with sufficient strength. The sum of ARP and RRP is the full recovery period (FRP).

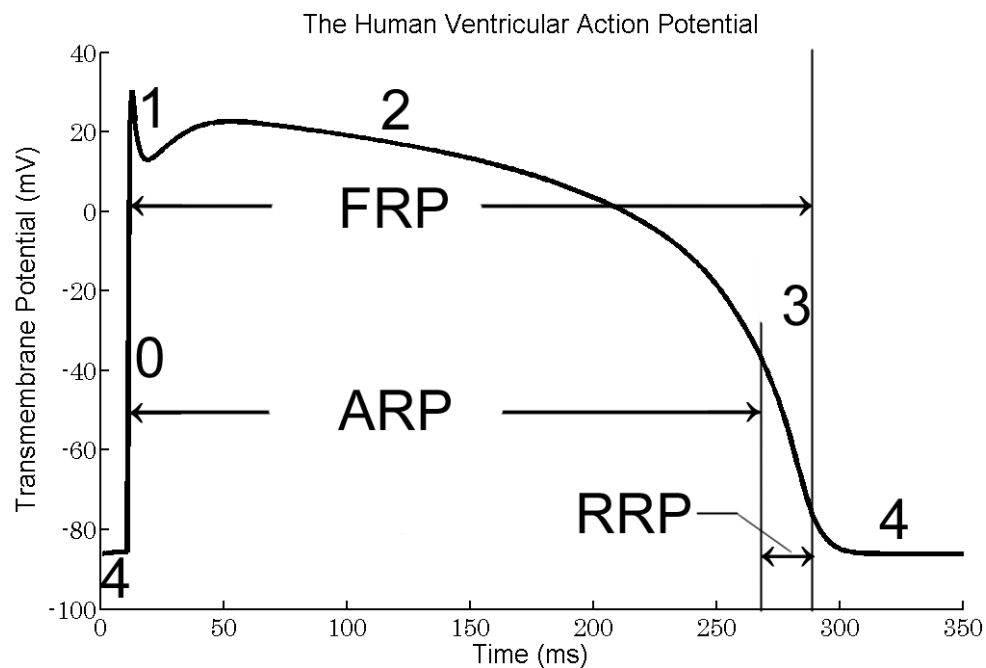


Figure 1.5 An action potential generated by a simulation of a human ventricular epicardial cell model [32]. The action potential consists of 5 phases from 0 to 4. Key: FRP = full recovery period, ARP = absolute refractory period, RRP = relative refractory period. See text for details.

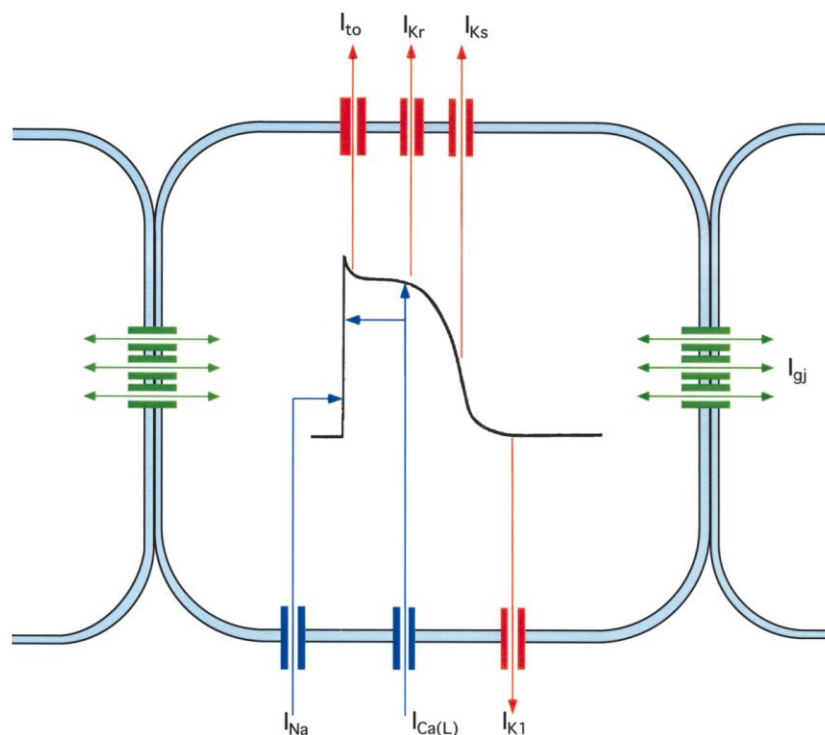


Figure 1.6 A general scheme of human ventricular myocyte representing the major membrane ionic currents mediating ventricular action potential [33]. The blue arrows represent the inward currents and the red ones represent the outward currents; these arrows point to their functional phases of the action potential. The green channels denote the intercellular gap junctions.

Cardiac cells are interconnected by gap junctions that are prerequisite for excitation conduction [34]. One gap junction is integrated with connexons which directly connect the cytoplasm of two abutting cells and provides a channel for molecules and ions exchanges between cells [35] (see green channels in Figure 1.6). When a cell is excited, influx of cation makes the intracellular side positive with respect to the extracellular side and consequently creates a voltage gradient between this depolarized cell and its yet to be depolarized neighbors, resulting in the current flow radiating from the depolarized cell to its coupled cells via the gap junctions. This current charges and excites these adjacent cells, and then the adjacent cells' adjacent cells. In this manner, the excitation propagates throughout the entire heart (please refer to Kléber *et al.* [31] for fundamental biophysical principles of the propagation) as mentioned above. This excitation propagation can be viewed as an electrical wave, with a wave front corresponding to the action potential upstroke and a wave back corresponding to the fast repolarization [36, 37].

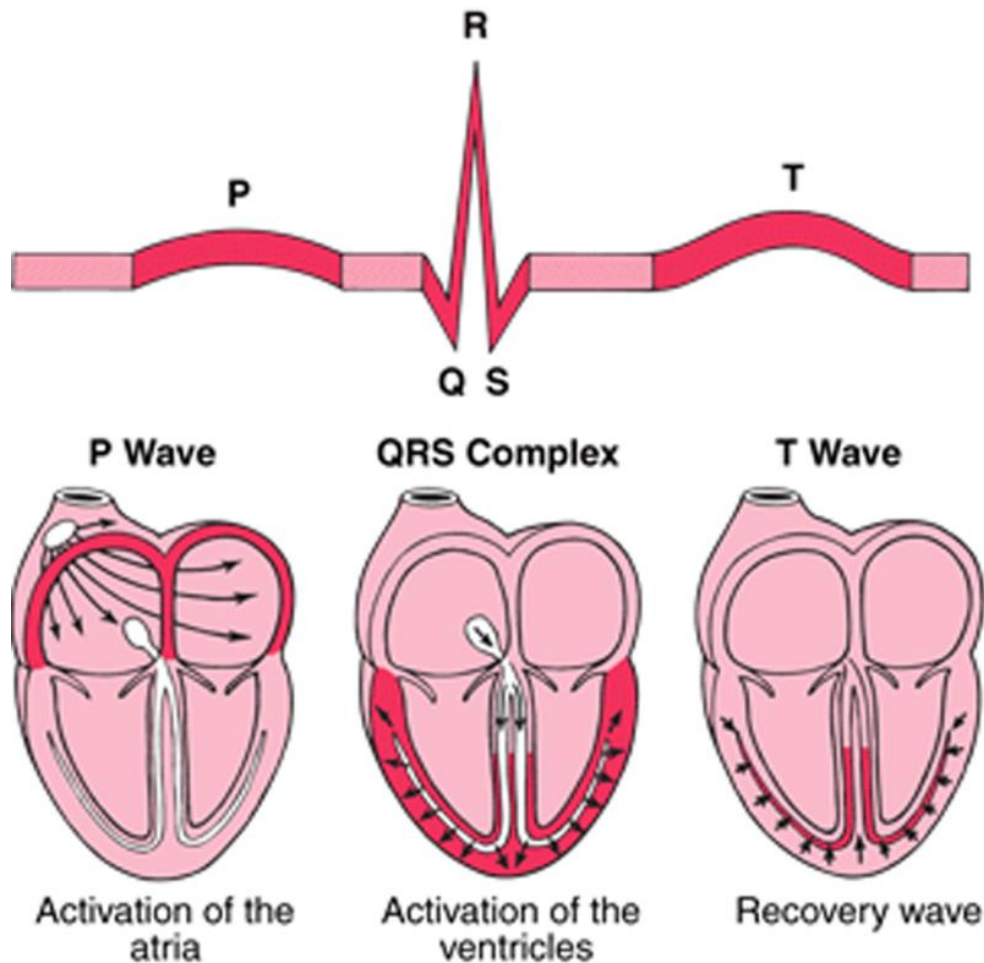


Figure 1.7 The PQRST complex and its relevant electrical activities [38]. The upper panel, an intact PQRST complex with pink isoelectric lines and red deflections. The lower panel, contributors to the different waves in sinus rhythm ECG. See text for details.

The electrical propagation activity in the heart can be recorded by electrodes deployed at body surface and the detected signal is called the electrocardiogram (ECG), a vital and essential component in cardiac diagnosis [39] since its acquisition is painless, safe, noninvasive [40] and economic. The ECG manifestation of the normal heart beat (sinus rhythm) is the PQRST complex named by Willem Einthoven. Figure 1.7 upper panel displays a normal PQRST complex and its corresponding cardiac electrical activities responsible for respective deflections of the ECG trace. P wave is generated by atrial activation; QRS wave is a symbol of ventricular activation, and T wave reflects ventricular recovery process (see Figure 1.7 lower panel). Please see Malmivuo *et al.* [41] for more knowledge about the ECG.

1.3 Reentry and hypotheses of ventricular fibrillation

Although most hearts beat with remarkable fidelity and resilience, some heart rhythm can go mad under certain circumstances. These phenomena are recognized as the cardiac arrhythmias [42]. Peter N. Jordan *et al.* [27] pointed out that, “the danger inherent to arrhythmias is manifested not in the effects the abnormal rhythm has on the cardiac tissue itself, but the effect that the abnormal rhythm has on the mechanical functioning of the heart. Ventricular arrhythmias can lead to excessively rapid and, in some situations, uncoordinated contraction, causing a drastic reduction in the efficiency with which blood is pumped throughout the body”. The general classification of cardiac arrhythmias assumed that all disturbances of rhythm resulted from abnormalities in impulse initiation and propagation [43]. Because the abnormality in impulse generation is usually related to cardiopathology [43], only the arrhythmias caused by abnormalities in propagation are discussed below.

Normally, activation waves shall extinguish after propagating throughout the entire heart and only the spontaneous firing of SAN can keep triggering continuous action potentials of each cell. However, under certain circumstance, previously activated region is activated repeatedly because the activation wave reenters the same tissue and reexcites it. This form of abnormal propagation is called reentry, one of the most special forms of abnormal conduction [43]. Figure 1.8A illustrates a simplified description of reentry formation. An initial trigger emerges at the I zone and bifurcates into two branches shown by the green arrows, the excitation along the right branch is blocked at the orange zone of refractory tissue while another excitation wave passes along the left branch and reaches the II zone where it splits and heads for two opposite directions. Later the wave reaches the III zone, and then to the orange region and can go through it because the tissue leaves its refractory period (conductive at that time), subsequently reenter the I zone. The orange zone behaves a “one-way” or unidirectional block. In this manner, the loop activation following the red-arrow trajectory becomes self-sustained and requires no external drive.

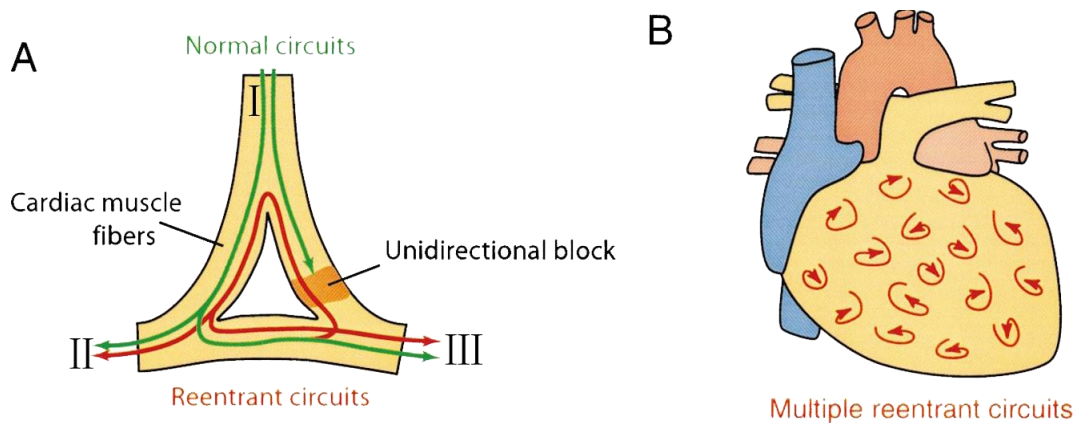


Figure 1.8 The mechanism of reentry formation and simultaneously excited reentrant circuits [44]. (A): a schematic view of reentry. The green arrows represent the normal conduction in a bifurcated pathway and one through the right branch is blocked at the orange zone of refractory tissue; if the propagation speed is slowed, then reentry through the orange area can occur (trajectory showed by the red arrows). See text for details. (B): multiple reentrant circuits happening in the ventricles.

Reentry can be briefly categorized as three types: reflection, phase 2 and circus movement. The former 2 kinds typically happen in limited and localized areas, making them appear as series of focal activation, and frequently denoted as microreentry. The circus movement, the most common reentry, often does not have a focal manifestation and is correspondingly referred to as macroreentry [27]. This type of reentry refers to the circulation of an activation wave front around an anatomical or functional obstacle in the heart, resulting in repetitive tissue activation at a frequency depending on conduction velocity around the obstacle and reentry path length [45]. The reentry hereinafter solely represents the macroreentry unless otherwise stated.

Reentry spanning several centimeters is believed to be a common cause responsible for ventricular tachycardias (VT) [46, 47], an arrhythmia precedes VF, and it has been posited that the transition from VT to VF may arise from the rapid fractionation of reentrant waves that formed at the onset of VT [42]. It is postulated that the development of multiple reentries within the ventricles causes VF [44] (see Figure 1.8B).

The “multiple-wavelet” [48] and “mother-rotor” [49] hypotheses are two dominant hypotheses to explain cardiac fibrillation [50]. The former one was hypothesized by Moe on the basis of computer simulations in a two-dimensional matrix of coupled excitable units representing a cellular automata with random refractory periods.

According to this hypothesis, cardiac fibrillation is sustained by instable wavelets that incessantly emerge, bifurcate, and collide or fuse with each other; these wavelets are perpetuated by continuous wavebreaks and self-regenerating reentry; all parts of the tissue are of equal importance to maintain the fibrillation. The latter one was first put forward in 1925, and reemphasized and improved by Jalife *et al.* [49, 51]. This hypothesis assumes that fibrillation is driven by an individual stable reentrant source of activation, also called the mother rotor. The wave fronts are unable to sustain 1:1 conduction during their propagations. Instead, the rotor emits fibrillatory conduction with intermittent propagation blocks, producing multiple irregular activation patterns, and wavebreaks are not essential to sustain fibrillation. Hence, only the region where rotor located is critical to fibrillation maintenance. These two hypotheses are thought to be contradictory instead of complimentary mechanisms [52].

Nevertheless, more and more potent evidences emerge suggesting these two hypotheses are not mutually exclusive. It is generally believed that VF in guinea pig heart is maintained by the mother rotor [49, 51]; however, in 2001, Choi *et al.* [53] reported their results stating that the VF dynamics in guinea pig hearts were consistent with a multiple wave-make and wave-break mechanism. Meanwhile, it was also considered that the rotor is common in small hearts but rare in large ones, especially in swine [19] and canine hearts [54]; however, researchers managed to find signs of existence of mother rotor [55] and transmural reentry in pigs [20]. Furthermore, Nash *et al.* demonstrated that both mother rotor and multiple wavelets existed in human hearts [56], and Pak *et al.* suggested the same conclusion based on canine experiments [57]. So improvements and modifications of these hypotheses are required. To this end, new hypotheses emerged among which “restitution hypothesis” was considered as a promising one that may lead to a breakthrough in understanding VF [50].

In 1968, Nolasco *et al.* hypothesized that if the action potential duration (APD) restitution curve had a maximum slope over 1, it would lead to APD alternans [58], and discordant APD alternans was proven to be significantly proarrhythmic [32, 59-61]. This is called the “restitution hypothesis”, which is currently one of the most extensively studied hypotheses accounting for VF [32]. The restitution is referred to as

a function relationship between electrophysiological factors (either APD or conduction velocity (CV)) and the amount of time spent recovering prior to a stimulus (termed as diastolic interval (DI)) [37, 62].

The APD restitution (APDR) curve is the most widely used technique for quantifying the repolarization of cardiac tissue because such curve reduces the extremely high-dimensional kinetics of the cardiac cell to a simple one-dimensional relationship [27]. According to the “restitution hypothesis”, the restitution curve slope is a crucial determinant of the cardiac electrical stability: a slope of less than 1 is a necessary and sufficient condition for the stability of traveling pulse [63] and a slope of larger than 1 can cause APD alternans under short pacing cycle length (CL).

An illustration of APDR slope relating with APD dynamics is depicted in Figure 1.9. Figure 1.9A displays the situation when APDR slope is less than 1, and Figure 1.9B displays the situation when APDR slope is larger than 1. The cell is paced at a fixed CL which is the sum of APD and DI. When a premature beat happens (denotation “a” in Figure 1.9A) and the APDR slope is less than 1, oscillation in APD and DI decrease until they converge to a steady point. However, when the same ectopy happens with an APDR slope larger than 1, oscillations in APD and DI gradually increase with each cycle, forming a short-long response to pacing at a fixed CL, which is also called APD alternans [64], leading to 2:2 rhythm [27] and finally unidirectional block (denotation “b” in Figure 1.9B) owing to refractoriness, which is topologically essential for the reentrant activity initiation [65, 66].

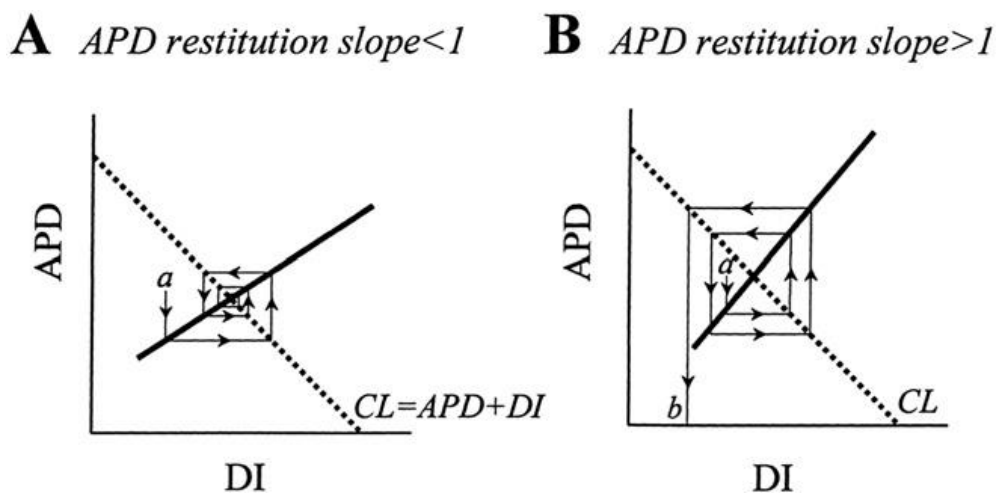


Figure 1.9 Relationship between APDR slope and APD dynamics [36].

Furthermore, when this APD alternant becomes spatial discordant, it provides a suitable substrate for premature beat to initialize reentry [59] and wavebreaks [36]. The fact that drugs which decrease APDR slope can prevent VF induction [67], reduce complexity of VF activation [68], and even suppress existing VF into regular rhythm [69] also proves the key role of APDR slope in VF induction and maintenance.

Recently experts began to realize that the APDR slope was an oversimplified touchstone of arrhythmogenic risk [32] and determinant of VF organization. For example, Cherry *et al.* demonstrated that due to strong electrotonic interactions and a flat CV restitution (CVR), spiral breakup may not happen even the APDR curve has a slope over 2 [70]. Experts have suggested that other factors like CVR also comes into play [71] because the wavelength (WL) of propagation is the product of APD and CV; and for wavebreak to occur the WL must be under a certain value at which propagation fails [72]. The synergistically proarrhythmic effects of APDR and CVR was proven *in silico* [37, 60, 73], in animal experiments [74], and in human trials [67].

In 1999, Weiss *et al.* [64] creatively connected both restitution properties with VF organizations. Based on an experiment of rabbit hearts using optical mapping in 2002, Wu *et al.* [75] confirmed this connection and claimed that there were two types of VF and illustrated that the fast (also called type 1 in their article) VF was associated with a steep APDR, a flat CVR and wandering wavelets; and the slow (type 2) VF was associated with a flat APDR, a CVR with boarder CV span and spatiotemporal periodicity. The fast VF could be converted to slow VF by perfusion of a certain heart drug. Later in 2004, they demonstrated that both VF could simultaneously exist in different zones of the heart during acute regional ischemia [76, 77] and simulated the process of transition from type 1 VF to type 2 VF in a 3D cardiac tissue slab [78]. They therefore hypothesized that both CVR and APDR were important in VF maintenance.

1.4 Simulation of arrhythmias on whole-heart models

The shape of heart model can be single cell [79], one-dimensional strain [34], two-dimensional plane [80], three-dimensional slab [76] and realistic heart anatomy [81]. For the latest development of heart models, see an excellent review by Cherry *et al.*[15]

Our research group has already developed a state-of-the-art 3D whole-heart model called the Wei–Harumi whole-heart model [13, 82]. The entire research of this dissertation is based on this model. A detailed description of this model is in Chapter 2.

A number of simulation studies of cardiac restitution using this model were published. The proarrhythmic effect of steep APDR (represented by APD rate-response and phase response) was successfully demonstrated by Wei *et al.* [83, 84], Watanabe *et al.* [85] and Yamaki *et al.* [86] based on this model. The restitution originally used in these studies was depicted by a linear function between APD and CL. However, recent literatures have showed that pacing CL decreasing causes the action potential behavior to bifurcate, in the manner that for every two stimuli, two different action potentials happen, called the 2:2 rhythm (see Fig. 5 in Jordan *et al.* [27]) as mentioned above. Thus the CL-dependence of APD is probably not as realistic as the DI-dependence of APD. Besides, the original CVR is also CL-dependent, and the role of CV has not been examined in this heart model.

The hypothesis proposed by Wu *et al.*[75, 87] inspired us to check whether the whole-heart model with certain restitution configurations can yield the corresponding VF dynamics as observed by Wu *et al.* If so, then it is quite likely that the APDR and CVR are both major determinants of VF organization.

In this dissertation, different DI-dependent APDR and CVR settings were included in the Wei–Harumi whole-heart model and VF was induced to check its responses to the alternations of restitution configurations. Because virtual heart does not have spontaneous VF, we first studied the relationship between cardiac vulnerability to VF induction and APDR slope to check the feasibility of inducing VF in the Wei–Harumi

model with DI-dependent APDR, and found that steeper APDR slope was connected with higher success rate of VF induction. Secondly, we investigated the effects of VF-induction configuration by inducing VF at different sites of the heart model with different induction protocols, and found that the VF organization was neither correlated with the induction method nor the induction site. After that we carefully studied the effects of synergy of APDR and CVR to reach the main conclusion of this dissertation. Studying T wave can provide us considerable information for investigating mechanism of VF genesis. Thus we also studied the mechanism of T wave formation, and obtained some findings concerning the relationship between APD dispersion and the T wave. Based on these findings we proposed a hypothesis that the anteroposterior APD gradient contributes to the genesis of the T wave.

1.5 Layout of the dissertation

The dissertation is organized as follows:

Chapter 1 (Introduction)

This chapter introduces the background and the purpose of the work introduced in this dissertation.

Chapter 2 (The whole-heart models)

This chapter provides an overview of electrophysiological heart models and a detailed description of the Wei–Harumi whole-heart model.

Chapter 3 (Effect of APDR Slope on vulnerability to VF induction)

This chapter shows the relationship between APDR slope and VF inducibility. The level of VF-induction risk is defined as the quantity of minimum ectopic stimuli required to induce sustainable VF. The results suggested that the APDR slope may significantly affect cardiac vulnerability to VF induction.

Chapter 4 (Effects of VF-induction Configuration on Induced VF Organization)

This chapter checks the relationship between VF organization and VF-induction configuration. The results suggested that the interactions between VF-induction protocols and sites determined the odds of successful induction but once VF was induced, its pattern was solely determined by the inner cardiac properties of the heart model.

Chapter 5 (Effects of Cardiac Restitutions on VF Mechanisms)

This chapter demonstrates the relationship between VF organization and synergy of APDR and CVR. The simulations successfully reproduced the phenomena observed in animal experiments, and supported the hypothesis that the APDR is the major determinant of VF organization, and CVR also come into play by influencing wave-front stability. The simulation suggests that restitution properties are important in VF maintenance and conversion.

Chapter 6 (Effects of APD Gradients on T-wave Genesis)

Studying T wave may facilitate understanding VF. This chapter studies the relationship between the APD gradients and T-wave amplitude. The roles of transmural, apicobasal and interventricular APD gradients were already investigated by reported studies. Our work suggests that besides these gradients, the anteroposterior APD gradient also contributes to the T-wave genesis.

Chapter 7 (Conclusions)

This chapter summarizes the contributions, points out limitations and prospect further work of this dissertation.

Chapter 2 The whole-heart models

2.1 Introduction

The increasing availability of both detailed experimental data and high-performance computers enables researchers to adopt computational models as a valuable research tools for investigating mysteries of the heart [12, 22]. The heart models can be divided into two large groups: electrophysiological and nonelectrophysiological models [13]. The latter ones are beyond the range of this dissertation and we only focus on the electrophysiological models which can be categorized into three types by using model scale as the division-criterion: single-cell model, cell-network model and whole-heart model (see Figure 2.1).

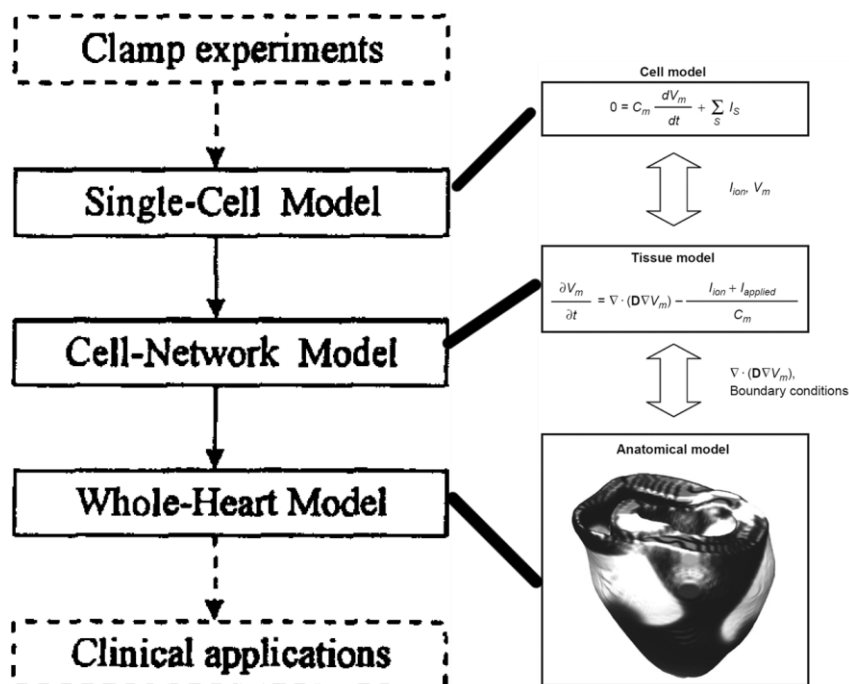


Figure 2.1 Hierarchy of electrophysiological cardiac models of different scales. Left column, classifications of the heart models [13]. Right column, corresponding integration of different levels in a whole-heart model, showing how different level models are coupled [12].

2.2 Heart models of different scales

2.2.1 The single-cell model

The model of the smallest scale is the single-cell model. It simulates the elementary mechanism of cardiac activity by mathematically describing action potentials of different cardiac cells. As mentioned in the previous chapter, the action potential is the manifestation of differences between intracellular and extracellular ionic concentrations, regulated by transmembrane currents through channels. The single-cell model uses Hodgkin and Huxley's method developed in their study of membrane ionic current in nerves to describe the ionic kinetics obtained from patch clamp experimental results with difference equations (see Figure 2.1 upper-right equation) [88]. So the authenticity and accuracy of the single-cell model depends on new facts emerging from experiments, in other words, the single-cell model takes the patch clamp data as its input.

It is worthwhile to mention the CellML language [89], which is an open standard based on XML markup language. It is being developed by the Auckland Bioengineering Institute at the University of Auckland and affiliated research groups. It aims at easing the storage and exchange computer-based mathematical models. Dr. Alan Garny developed the Cellular Open Resource (COR, see Figure 2.2), an environment for cellular modeling based on the CellML language [90]. It provides an interface that greatly facilitates applications of all kinds of cardiac cellular models as long as they are written in CellML, and these CellML-based codes can be exported to a variety of common used computer languages including MATLAB, C, C++, Java, *etc.* Currently there are over 100 heart cell models available and many literatures referring to their specifications [12]: ten Tusscher *et al.* [91] compared features of four ventricular models; Fenton *et al.* [92] summarized properties of 45 models covering Purkinje cell models, ventricular cell models, atrial cell models, sinoatrial node cell models and atrioventricular node cell models. They also illustrated action potentials from a broad range of simple and complex mathematical cardiac cell models [15].



Figure 2.2 The logo of the Cellular Open Resource, developed and maintained by Dr. Alan Garny [90]

All single-cell models are based on an appreciable number of empirical components, and constructions of these models largely rely on the ability to fit model parameters of individual ionic currents [80]. There are two major flaws with this method. One is that the model parameters that one can extract by fitting experimental data are usually not unique [93, 94]. The other one is that significant errors of the parameter values exist owing to experimental and technical limitations as well as the numerical procedures adopted to estimate the model parameters. Both factors are believed to severely impair the quality and accuracy of the model prediction [80].

2.2.2 The cell-network model

The model of the median scale is the cell-network model, better known as the “tissue model” whose ‘input’ is the ‘output’ of single-cell model [12]. The main purpose of cell-network modeling is to describe the propagation process of action potential and the polarization process of cardiac tissue arising from external stimulations in excitable tissues [13]. This modeling generally assuming that a tissue can be represented either as a regular arrangement of single-cell units interconnected by intracellular and extracellular resistances [34], or as a functional syncytium where membrane voltage is supposed to propagate smoothly manifested as consequent action potentials [13] triggered and modulated by intercellular currents (denoted as I_{applied} in the middle-right diagram of Figure 2.1) via gap junctions [95].

The organization of cell-network model can be 1-dimension (1D), 2-dimension (2D) or 3-dimension (3D). In 1D, the basic propagation model is a strand or a ring of cardiac cell units governed by cable equations [96]. Based on the bidomain approach, cable equations are extended from 1D to 2D and 3D with inclusion of anisotropy and

discontinuous bidomain [13]. According to the assumption of bidomain model, the cardiac tissue is conceived as the superposition of two averaged continuous media, the intercellular and extracellular medium, separated by a theoretical membrane of zero thickness. Details of the anisotropic cardiac source calculation in bidomain model are stated in the session 2.3.5.

The cell-network model plays a significant role in understanding clinic and experimental phenomena as well as providing new insights into mechanisms of cardiac activities. Despite the simplicity of 1D and 2D tissue models, fruitful outcomes can still be obtained based on their simulations. ten Tusscher *et al.* [32] studied the occurrence of action potential duration (APD) alternans in a ring and measured the conduction velocity (CV) restitution in a cable of cells. Otani *et al.* [73] found out a sufficient condition for propagation failure in a homogeneous 1D system. Conrath *et al.* [34] showed the functional invisibility of M cell in a strand of transversally oriented myocytes running from endocardium towards epicardium. Moe [48] advanced the celebrated multiple-wavelet hypothesis accounting for the cardiac fibrillation based on a simulation run in a 2D array of coupled excitable elements. Weiss *et al.* [36, 64] proposed that the APD restitution and CV restitution are key determinants of wavebreak through a simulation study in a 2D Luo-Rudy model. The importance of heterogeneity of APD restitution in promoting wavebreak and reentry was confirmed by Clayton *et al.* [97], Krogh-Madsen *et al.* [98], Xie *et al.* [99] and Nash *et al.* [100] (a combined clinical and modeling study) using 2D cell-network models. Besides, there are also a lot of other 2D-tissue-model involved studies that offered new understanding of cardiac researches [80, 101-104]. The most complicated cell-network model is the 3D-tissue model, also called the slab model. It represents a wedge preparation of cardiac tissue and allows complex simulations [78, 105-107]. Please see Plonsey *et al.* [108] for detailed descriptions of the cell-network models.

As the transitional layer between the single-cell model and the whole-heart model, the cell-network model has a special role in arrhythmia research. Because the only kind of arrhythmia that the single-cell model can simulate is the abnormal impulse generation, simulations of arrhythmia regarding abnormal impulse conduction can

only be run on cell-network models and whole-heart models. However, constructing a whole-heart model is laborious and costly. Furthermore, simulations on whole-heart models are usually computing-consumptive. It usually takes several wall-clock hours [14, 94, 109, 110] to simulate just 1s cardiac propagation in whole-heart models even taking advantage of super computers. Intuitively, studying cardiac activity in the whole-heart model is always not the optimal choice either due to condition limitations or overqualification of the whole-heart model. Under certain study circumstances, the cell-network model is adequate for the research aims or its insufficiencies are well tolerable because they do not affect the deduction of main conclusions. As stated in Chapter 1, studying behaves of reentry is important for understanding cardiac fibrillation. The cell-network model is an ideal platform for exhibiting reentrant waves regardless its dimension [15]. The manifestations of reentry in 1D, 2D and 3D models are 1D ring, spiral wave and scroll wave respectively (see Figure 2.3). Nash *et al.* [22] pointed out that the success of many predictions was based on simulations first encountered using simple models. Basic effects such as the structure of spiral wave core, meandering of spiral waves in 2D, curvature-induced filament drift in 3D were first predicted by cell-network models and later extended to more refined models [22]. For more information about the cell-network models in arrhythmia investigations, please see splendid reviews elsewhere [15, 31].

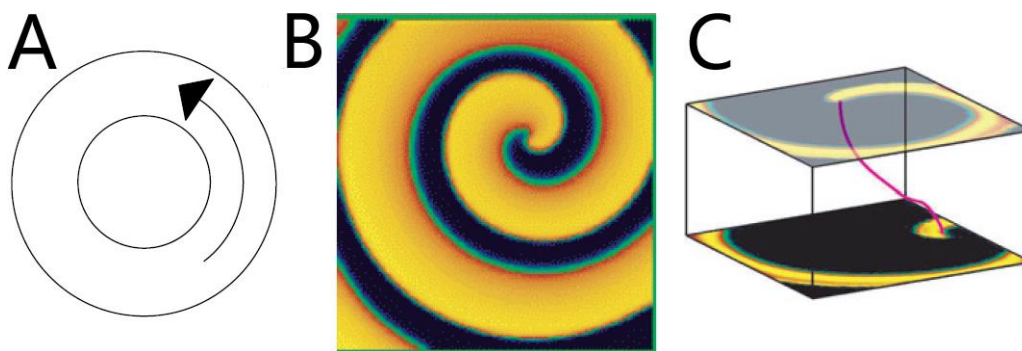


Figure 2.3 Forms of reentry in cell-network models of different dimensions. (A): 1D ring [27]. (B): a spiral wave rotating around a core [15]. (C): a scroll wave [15], the purple vortex filament is a cluster of spiral wave cores in different layers parallel to the upper and lower planes.

2.2.3 The whole-heart model

The whole-heart model is the top level of the hierarchy. The term “whole-heart model” was coined by Lorange *et al.* [111]. According to Wei [13], whole-heart models may refer to 3D heart models which contain realistic shape and are capable of simulating activation process of the heart and the body surface ECG potentials. In a broad sense, the whole-heart model can be characterized in the following ways:

1. The whole-heart model is generally defined as a macroscopic model which stands for an intact heart or parts of the heart (see the lower-right corner image of Figure 2.1), e.g. the left ventricle or both ventricles. Most whole-heart models incorporate realistic heart shape and anatomy.
2. The macroscopic nature of the whole-heart model also depends on the scale of its elements. The element of a whole-heart model usually has a size several thousand times larger than the actual size of a true heart cell. In this sense, an element in a whole-heart model is a lumped model of tissue.
3. The main purpose of a whole-heart model is to investigate global behaviors of the heart. Therefore, many whole-heart models do not incorporate a cellular mechanism directly relating activation process of the whole heart to the transmembrane ionic currents. Instead, these models employ Huygens' Principle as the propagation strategy to simulate the excitation process of the heart.
4. Most whole-heart models are accompanied by a torso volume conductor model, and aimed at reproducing surface potential. This kind of model yields clinically comparable ECG waveforms. In this aspect, the whole-heart models are closer to clinical applications than the single-cell or cell-network models.

Although such features were summarized over a decade ago, most of them still hold accuracy and precision [112]. However, because of the rapid development of cardiac modeling, new trends of whole-heart modeling emerge:

1. Most newly developed whole-heart models [14, 65, 94, 110, 113-116] incorporate partial differential-equation-based (the same as the middle-right

equation in Figure 2.1 used in the cell-network model) cardiac transmembrane potential models [12]. In other words, the real-time cellular dynamics is governed by transmembrane (I_{ion} in Figure 2.1) and intercellular currents ($I_{applied}$ in Figure 2.1) instead of preset action potential morphology. This kind of heart model is called the “reaction-diffusion” model [117].

2. Patient-specific whole-heart model is expected to be developed for clinical implementation. Several research groups have already yielded fruitful results [118-122].
3. Incorporating electromechanical effect into the whole-heart model is being studied to realize ECG simulation calculated in a “beating” whole-heart model [22, 123-125].

Constructing a whole-heart model is a computationally daunting task [125]. Even if there are models available, choosing a proper model is critical for simulation study so that details of the model can be balanced against computational time [12]. As briefly mentioned in the session 2.2.2, “reaction-diffusion” models demand large computational resources. Although several speed-up algorithms [116, 126, 127] have been proposed to increase calculation efficiency, super computer is still the exclusively platform for “reaction-diffusion” whole-heart models because their required time of personal-computer-based simulation is frustratingly long.

2.3 The Wei–Harumi whole-heart model

In this dissertation, the Wei–Harumi model is utilized to simulate VF. It is a whole-heart model with an intact heart chamber configuration (the right atrium, the left atrium, the right ventricle and the left ventricle) and has been widely distributed and accepted as a state-of-the-art whole-heart model [112]. Based on this model, computer simulations of the Wolff-Parkinson-White (WPW) syndrome [128], supraventricular tachycardia with different reentries [129], Brugada syndrome [130], torsade de pointes [131] and other arrhythmias [84] including VF [83, 85, 86] have been successfully carried out and provided sufficient evidences to prove the power of

the Wei–Harumi model in simulating complex arrhythmias run on personal computers with acceptable time consumptions (an entire simulation process usually completes within an hour) which can be further reduced by taking advantage of hybrid computation (CPU and GPU) [132]. Recently, Zhu, *et al.* demonstrated the feasibility and reliability of simulating clinical electrophysiological study in the Wei–Harumi model [133]. Intuitively, utilizing the Wei–Harumi whole-heart model as the study platform is a wise choice.

2.3.1 A general description of the Wei–Harumi model

The heart model is constructed in an inclined, 3D coordinate system with equal axial angles of 60° . It is divided into $56 \times 56 \times 90$ units with a uniform 1.5mm spatial resolution. The intersection points which coincide with heart muscle form discrete unit of the heart model, denoted as model cells (see Figure 2.4 for illustration of spatial configuration of the model cell). The location of each model cell is indicated by coordinates, i ($1 - 56$), j ($1 - 56$), k ($1 - 90$). Overall, there are approximately 50,000 model cells which are categorized into 15 types: SAN, atrial cell, AVN, HB, BB, PKJ, ventricular cell, seven kinds of user-defined model cells and connection fiber. Each type can be assigned with different electrophysiological characteristics. For simplicity, simulation of myocardial motion is not performed in the model. Because this model focuses on studying electrical activation generation and propagation inside the heart, anatomical parts without electrophysiological attributes, e.g. the cardiac aorta, are not included in this model.

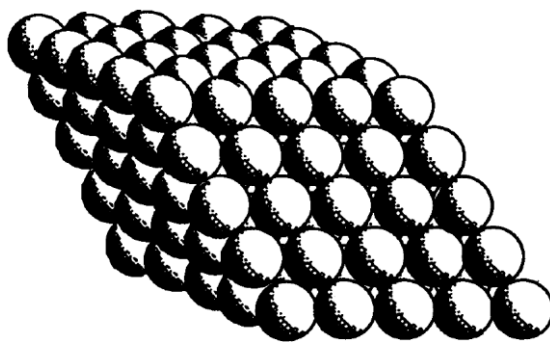


Figure 2.4 Spatial configuration of model cells in an inclined 3D coordinate system with equal axial angles of 60° [82]. A sphere represents a model cell.

2.3.2 Electrophysiological parameters

Table 2.1 Electrophysiological parameters of the model cell

PROPERTY	PARAMETER	DEFINITION
Action Potential	T0 (ms)	Duration of action potential phase 0
	T1 (ms)	Duration of action potential phase 1
	T2 (ms)	Duration of action potential phase 2
	T3 (ms)	Duration of action potential phase 3
	ARP (ms)	Absolute refractory period
	FRT (ms)	Full recovery time
	V0 (mV)	Transmembrane potential of phase 0
	V1 (mV)	Transmembrane potential of phase 1
	V2 (mV)	Transmembrane potential of phase 2
	GRD (ms/layer)	Gradient of APD distribution
	DC (%)	APD change rate to coupling interval
Automaticity	DVT (ms)	Deviation of APD for random distribution
	ECF (%)	Effective conductivity factor
	ICL (ms)	Intrinsic cycle length
	PRT (1/0)	Protection indicator (Yes/No)
	DLY (%)	Maximum delay of modulation
Conduction velocity	ACC (%)	Maximum acceleration of modulation
	BKP (%)	Break point position of phase response curve
	CV (cm/s)	Conduction velocity of fiber direction
Pacing	TD (%)	Transfer delay
	CD (a/r/b)	Conduction direction (antegrade/retrograde/both)
	BCL (ms)	Basic cycle length
	BN	Beat number of pacing
	INC (%)	Increment of BCL

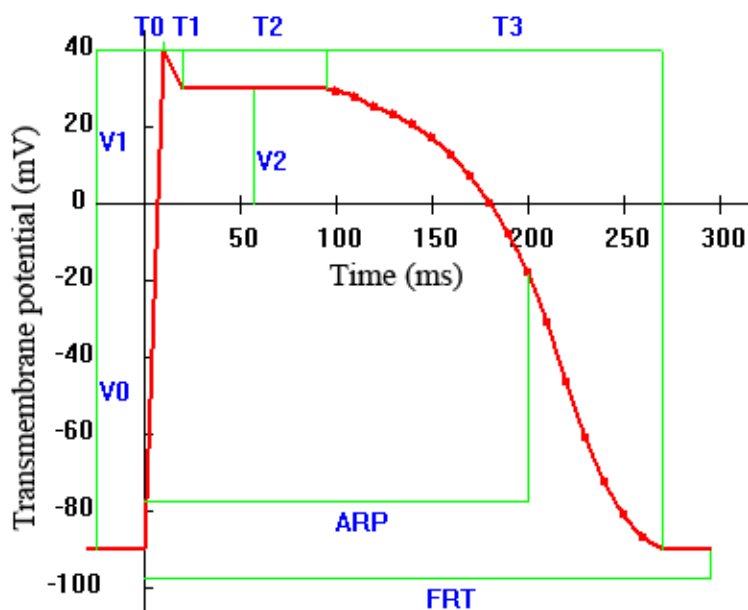


Figure 2.5 Definition of the action potential of a model cell and illustration of its related parameters. T_i ($i = 0,1,2,3$) and V_i ($i = 0,1,2$) are duration and potential of phase i of the action potential respectively. Phase 3 is represented by a curve through second-order Lagrange interpolation of sample data. Key: ARP = absolute refractory period, FRT = full recovery time.

The electrophysiological parameters of model cells are related to action potential, conduction velocity, automaticity and pacing (see Table 2.1).

Unlike “reaction-diffusion” models, the model does not “calculate” action potentials. Instead, it takes action potentials provided by literatures or simulations of single-cell models as its input. Each type of model cell has a set of values of action potential parameters (see “Action Potential” part in Table 2.1 for these parameters) to derive its corresponding action potential. An example of action potential defined in simulations is shown in Figure 2.5. The red straight lines specified by time intervals and voltages are representing the phases 0, 1, 2 and 4 of the action potential, and the phase 3 is defined by a curve through second-order Lagrange interpolation of sample data. For simplicity, APD variations were realized by assigning different time spans of the plateau phase, the full recovery time (FRT, the same as FRP defined in Chapter 1) is equal to the APD.

The ARP is independently defined as a portion of the APD. The interval between FRT and ARP is treated as RRP. In addition, the ARP of a model cell is conceptually equivalent to its effective refractory period (ERP). As we know, ERP’s end is the earliest moment when stimulation can be liberated which shall be conducted through

the tissue, for the response is judged by the arrival of excitation wave at distance or by the beat of the whole heart [134]. On the other hand, ARP is the time when a new action potential cannot be triggered. Therefore, ERP is measured at tissue and organ level, while ARP is defined at cell level. Concisely speaking, ARP is the period when no action potential can happen, and ERP is the period when no conducted action potential can be elicited. In fact, ERP includes the ARP and early part of the RRP [135]. However, equivalence of these two concepts is still rational because they are very similar terms and their difference is trivial. In the Wei–Harumi model, ERP equals to ARP and such approximation can hardly harm the quality and accuracy of simulation.

In the Wei–Harumi model, the automaticity is divided into protected and unprotected modes (represented by the parameter of PRT in Table 2.1). If a model cell is of unprotected automaticity, its excited neighboring cells can activate it and reset its automaticity. Otherwise, the model cell responds to external stimuli in a manner that bases on a phase response curve (PRC). When stimulation is applied to the cell, its intrinsic cycle length (ICL) is changed by a percentage (ordinate) according to its phase immediately before the stimulation (abscissa). Assigning protected automaticity to one model cell can make it become an ectopic pacemaker. Figure 2.6 shows a PRC set to a focus located at left ventricular wall to create premature ventricular contracts (PVC, see Figure 2.7).

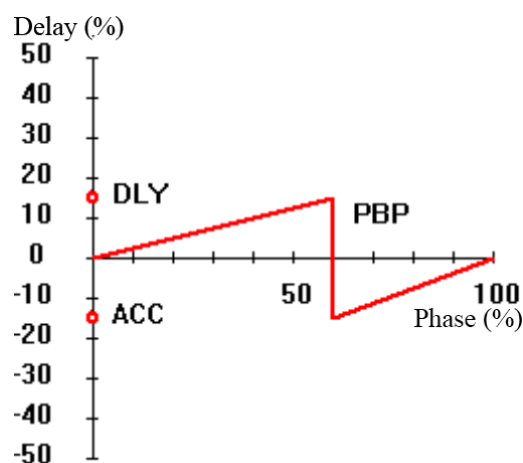


Figure 2.6 A phase response curve used in simulating PVC. The definitions of all abbreviations are in Table 2.1. Units of both ordinate and abscissa are percentages of intrinsic cycle length (ICL). On the left side of the phase break point (PBP, equivalence of BKP), the curve increases linearly from 0% to DLY, and abruptly drops to ACC, and then linearly increases to 0%.

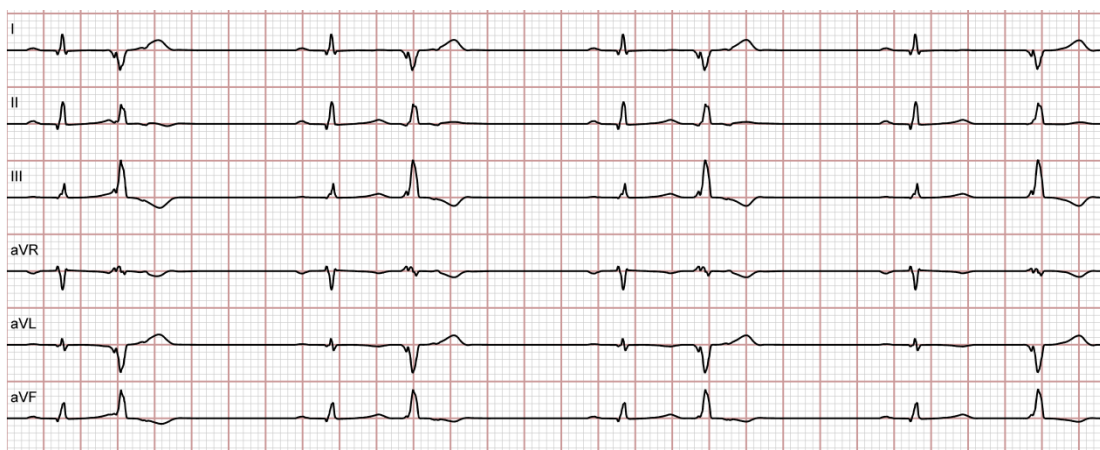


Figure 2.7 A strip of bigeminy ECG simulated from a heart model with a left ventricle located ectopic focus. Each normal QRS complex is accompanied by a PVC.

In the Wei–Harumi model, conduction velocity (denoted as CV in Table 2.1) is set to be zero during ARP, and after FRT, it is set to be a constant. During RRP, conduction speed is assumed to be proportional to coupling interval. The parameter TD , defined as a percentage of CV , is used to determine the initial conduction speed as soon as ARP ends. The parameter CD is used to indicate the conduction direction. The mentioned conduction velocity is along the principal myocardial fiber direction. CR defines the ratio between conduction speed along and across the fiber orientation. When CR is larger than 1, simulation is anisotropic; when it equals to 1, it means isotropic conduction. Definition of the fiber directions for all model cells is introduced below.

The “Pacing” in Table 2.1 means mandatory activation, and a model cell with “Pacing” properties excites every “basic cycle length” (BCL) for “Beat number of pacing” (BNP) times. The pacing rate may change with a rate defined by INC.

2.3.3 Anisotropic property

The Wei–Harumi model is an anisotropic model. For simplicity, it is assumed that every model cell shares a constant anisotropic ratio (the CR as mentioned above). Since the anisotropy is specified by magnitudes of the conduction speed along and across the fiber direction, incorporating myocardial anisotropy requires determining a fiber direction at each model cell’s location. In the Wei–Harumi model, three

anisotropy related anatomic assumptions are made: 1. The ventricular fibers are of a laminar structure; 2. The directions of all fibers within the same layer are parallel, and angled to that of the fibers in other different layers; 3. The fiber orientations gradually rotate counterclockwise over 90° with increasing depth from epicardium to endocardium. In the Wei–Harumi model, only ventricular fibers are considered as anisotropic. Fiber directions for all ventricular model cells are determined as soon as a model is created.

The ventricular volume is transmurally and apicobasally sliced in an imaginary artificial manner that all epicardial model cells are simultaneously stimulated, the wave fronts proceed from the outermost layer deep into the endocardium at a velocity so that at each time step, propagation moved one model cell ahead. The sequential number of excitation moment for one model cell (coordinates: i,j,k) is used as the layer number in transmural and apicobasal dimensions and hereby referred to as $L(i,j,k)$. The septum part is layered specially to make septal fibers as natural extensions of the left ventricular fibers. Figure 2.8 gives a cross section of the transmural layered ventricular structure.

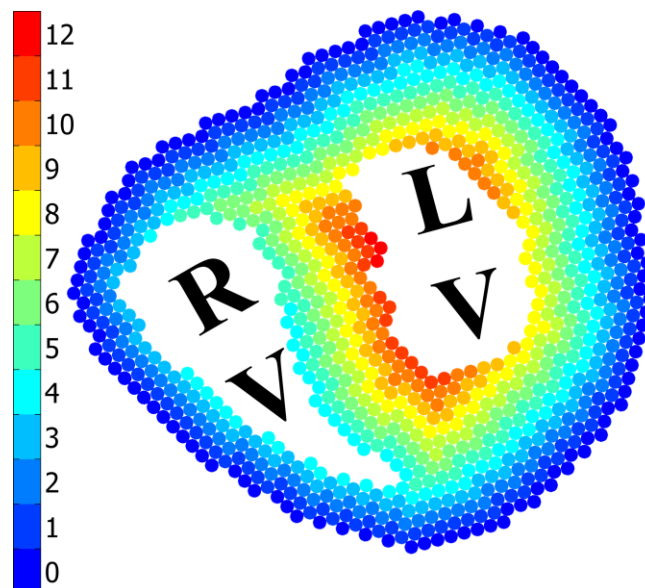


Figure 2.8 One horizontal cross section (taken from layer of $k = 40$) showing the layered structure. The layer number of the model cell is displayed by pseudo-color. Key: RV = right ventricle, LV = left ventricle.

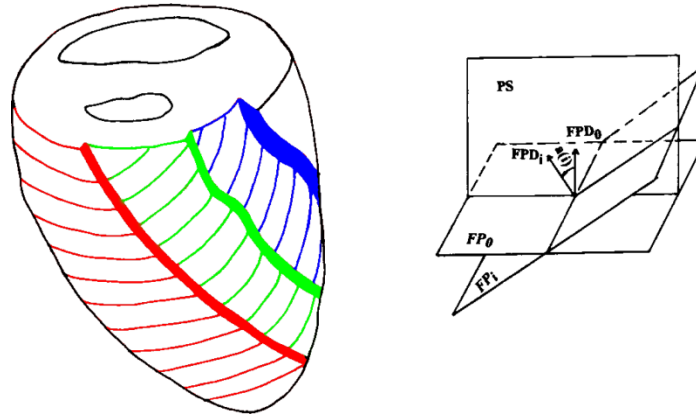


Figure 2.9 Rotating fiber directions at three representative layers (right image) and a sketch (left image) showing the relationship between fiber plane and fiber plane direction. Key: FP_0 = fiber plane of the epicardial layer; FP_i = fiber plane of layer i ; FPD_0 = fiber plane direction (FPD) of FP_0 ; FPD_i = FPD of FP_i ; $a(i)$ = included angle between FPD_0 and FPD_i ; PS = plane of septum.

As stated above, myocardial fibers within the same layer are parallel. Thus geometrically, these fibers can be regarded as intersection lines obtained by cutting the layer by a group of parallel fiber planes (FP) that share a common normal direction and hereafter referred to as the fiber plane direction (FPD). In the Wei–Harumi model, FPD of the epicardial layer is perpendicular to the geometric “heart axis” along the apicobasal direction. The left picture of Figure 2.9 shows the fiber directions in three adjacent layers. The fine red lines indicate the epicardial layer’s fiber direction, which are parallel to the FP_0 in the right picture. FPD of each layer beneath the epicardium is then generated by counterclockwise rotating FP_0 in the septal plane. The included angle for layer l is:

$$a(l) = l \times C / N \quad (2.1)$$

where N is the quantity of ventricular layers, C is the angle between FPD of the innermost layer and the FPD_0 and is set to be 90° . The left image of Figure 2.9 shows the fiber directions of two layers right under the epicardium (colored by green and blue) that are 7.5° and 15° to the red lines.

The fiber direction $\mathbf{F}(i, j, k)$ at a model cell (i, j, k) is determined by the outer product of two unit vectors. One is $\mathbf{P}(l)$, the FPD of the layer l where the model cell is located; the other one is the normal direction of the layer l , $\mathbf{N}(i, j, k)$. So $\mathbf{F}(i, j, k)$ is obtained by

$$\mathbf{F}(i, j, k) = \mathbf{P}(L(i, j, k)) \times \mathbf{N}(i, j, k) \quad (2.2)$$

2.3.4 Propagation strategy

The activation propagation of the Wei–Harumi model heart model complies with the Huygens’ Principle that every cell in the activation wave front represented a source of secondary wave fronts. The process of excitation propagation is computed with discrete time steps (ST) of 3 ms.

The activations can be either “non-conductive” or “conductive”. The former one is related with self-activated model cells, and their activation is obligatory as long as their firing moments come. The latter one refers to the propagation of depolarization from exciting model cells.

The calculation of conductive activation is realized in three steps. First, the range of propagation centered at each exciting model cell is determined. Its shape is an ellipsoidal wavelet whose long semi-axis is along the fiber direction at the exciting model cell, and the other two short semi-axes are along the transversal directions. The respective lengths of long and short semi-axes are

$$R_l = CV_l(t) \cdot ST \quad (2.3)$$

and

$$R_t = R_l \cdot R \quad (2.4)$$

where $CV_l(t)$ is the conduction velocity along fiber direction at time t ; R is the reciprocal of the anisotropic ratio. The extent of the wavelet is described by

$$l^2/R_l^2 + n^2/R_t^2 + t^2/R_t^2 < 1 \quad (2.5)$$

where l, n, t are coordinates in the local coordinate system of the exciting model cell (i, j, k) with three axes being $\mathbf{F}(i, j, k)$, $\mathbf{N}(i, j, k)$ in equation (2.2), and their outer product, respectively.

The second step is to judge excitability of the neighboring model cells inside the wavelet according to their refractoriness.

$$t - T_{\text{pre}} > \text{ARP}(t) \quad (2.6)$$

where T_{pre} is the moment of the previous activation time and $\text{ARP}(t)$ is the ARP at time t . As long as the inequation (2.6) is satisfied, this model cell is “excitable”.

The third step of the calculation is to assign a conduction velocity to excitable model cells for propagation at the next computation cycle.

These three steps are repeated for each time step until the end of the preset simulation duration.

2.3.5 Anisotropic cardiac source

Cardiac source is calculated by determining the relationship between transmembrane potential distribution and accompanied source of electromotive force. The bidomain theory [136] assumes that each point in the myocardium can be accounted as being either in the intracellular or the extracellular spaces, which are separated by a zero-thickness membrane. By applying Ohm's Law to the two domains and taking the anisotropic property into account, a relationship between current density, \mathbf{J} , and potential Φ can be established.

$$\mathbf{J}_i = -\mathbf{D}_i \nabla \Phi_i \quad (2.7)$$

and

$$\mathbf{J}_e = -\mathbf{D}_e \nabla \Phi_e \quad (2.8)$$

where \mathbf{D} represents the conductivity matrix, ∇ is the gradient operator. The subscripts i and e indicate the intracellular and extracellular domains, respectively.

For each model cell in the model, both equations above hold simultaneously. Under a quasistatic assumption, the two domains have the same current flux quantity in opposite directions.

$$\nabla \cdot \mathbf{J}_i = -\nabla \cdot \mathbf{J}_e \quad (2.9)$$

by putting equations (2.7) and (2.8) into equation (2.9), it can be rewritten as

$$\nabla \cdot (-\mathbf{D}_i \nabla \Phi_i) = \nabla \cdot (\mathbf{D}_e \nabla \Phi_e) \quad (2.10)$$

In this model, the extracellular space is considered to be "isotropic", and its conductivity is assumed as σ_e , so we can rewrite (2.10) as

$$\nabla^2 \Phi_e = \nabla \cdot (-\mathbf{D}_i \nabla \Phi_i) / \sigma_e \quad (2.11)$$

This equation satisfies the form of Poisson's equation and it is reasonable to treat the

source for the extracellular potential Φ_e as $(-\mathbf{D}_i \nabla \Phi_i)$. By using (2.7), intracellular current density \mathbf{J}_i can also be interpreted as current dipole moment per unit volume, and is referred to as cell dipole.

The propagation all over the heart volume generates time-changing distributions of transmembrane potentials of the heart (see Figure 2.10). In the simulation, for the model cell (i,j,k) , if the current time t satisfies the inequation (2.6), the model cell is at its resting state, otherwise, its transmembrane potential is a function of the time elapsed from the previous activation moment. Thus the transmembrane potential is determined by a piecewise function (see equation (2.12) and Figure 2.11).

$$\Phi_{ijk} = \begin{cases} A_{ijk}(t - T_{ijk}^{pre}) & t - T_{ijk}^{pre} < \text{ARP}_{ijk}(t) \\ \text{resting potential (nominal : } -90\text{mV)} & \text{otherwise} \end{cases} \quad (2.12)$$

where $A_{ijk}()$ is the action potential of the model cell (i,j,k) as a function of the time, T_{ijk}^{pre} is the moment of the previous activation time of the model cell and $\text{ARP}_{ijk}(t)$ is the ARP of the model cell at time t .

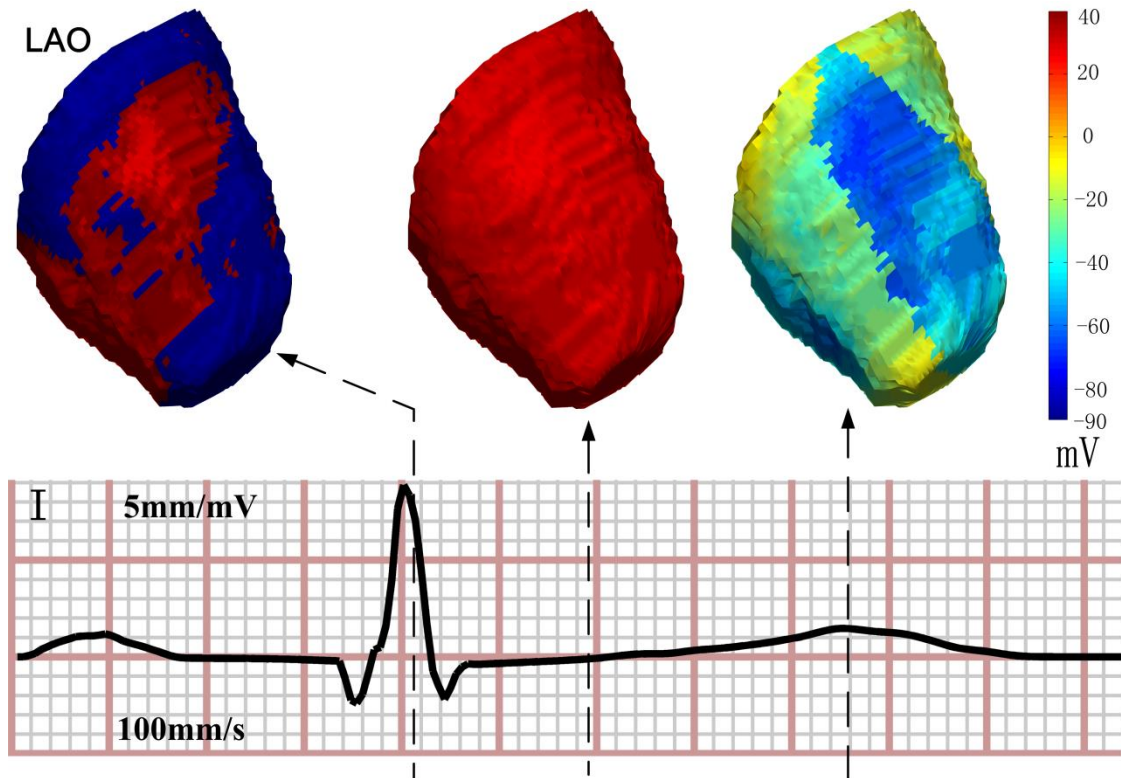


Figure 2.10 Three snapshots of epicardial transmembrane potentials distributions during a sinus rhythm. The shown pseudo-color transmembrane potential maps are taken from a left anterior oblique (LAO) view at three different moments shown by corresponding dashed arrows in the lower Lead I ECG trace.

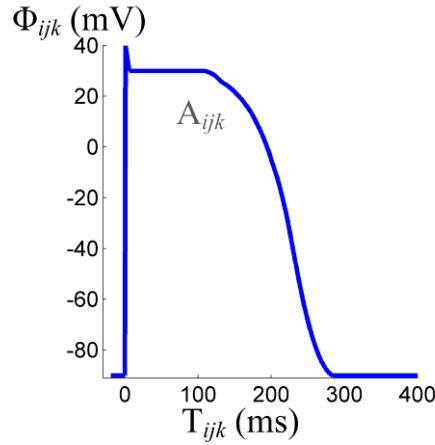


Figure 2.11 An example of the transmembrane potential of an epicardial model cell.

For simplicity, the model takes transmembrane potential as an estimation of the intracellular potential. Also, it is assumed that the intracellular conductivity is axially symmetric: the conductivity along the fiber direction is denoted as σ_l , and the conductivity along the transversal direction is denoted as σ_t . The fiber direction and two other perpendicular directions are selected to be the three axes of the local orthogonal coordinate system at a model cell and the conductivity tensor is:

$$\mathbf{D}'_i = \begin{pmatrix} \sigma_l & & \\ & \sigma_t & \\ & & \sigma_t \end{pmatrix} \quad (2.13)$$

Let \mathbf{p} , \mathbf{t}_1 and \mathbf{t}_2 (as a column vector) to be the unit vectors of the local axes in the global coordinate system, the conductivity tensor can be written as:

$$\mathbf{D}_i = [\mathbf{p} \ \mathbf{t}_1 \ \mathbf{t}_2] \mathbf{D}'_i [\mathbf{p} \ \mathbf{t}_1 \ \mathbf{t}_2]^T \quad (2.14)$$

where the superscript T is the matrix transposition.

Eliminating \mathbf{t}_1 and \mathbf{t}_2 from (2.14) results in:

$$\mathbf{D}_i = \sigma_t \mathbf{c} \quad (2.15)$$

and matrix \mathbf{c} is:

$$\mathbf{c} = \mathbf{I} + (r_2 - 1) \mathbf{p} \mathbf{p}^T \quad (2.16)$$

where r_2 is the conductivity ratio (CR defined in Table 2.1)

Finally, the cell dipole is determined by

$$\mathbf{J}_i = -\sigma_t \mathbf{c} \nabla \Phi_i \quad (2.17)$$

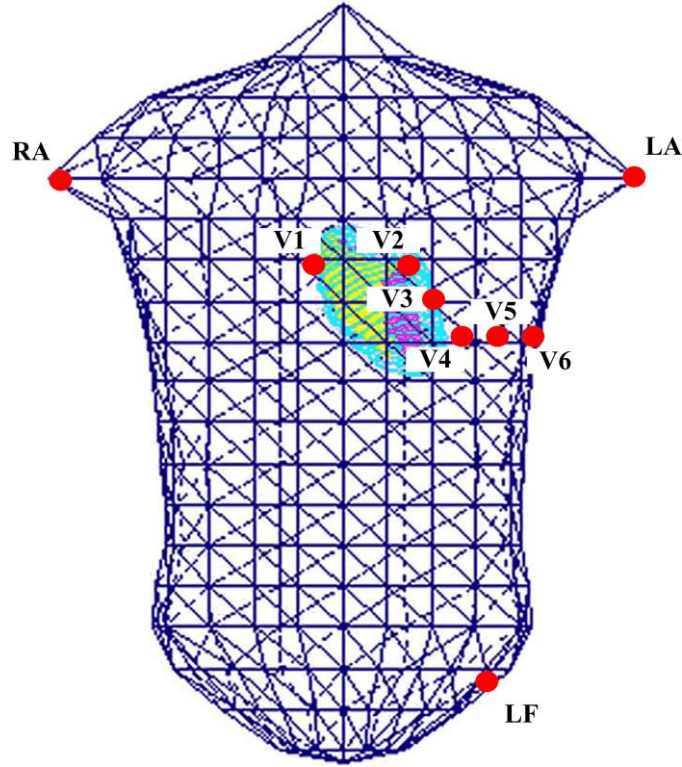


Figure 2.12 The heart–torso model. Red dots indicate the ECG electrode positions. Key: RA = right arm; LA = left arm; LF = left foot.

2.3.6 Calculation of surface ECG potential distribution

Computation of surface ECG potential is a typical volume conductor problem. In the Wei–Harumi model, the heart model is deployed inside a homogeneous conductor volume, a realistically shaped human torso reprinted by 688 triangular meshes (see Figure 2.12). We utilized an algorithm based on the boundary element method [137] to solve the Poisson equation and obtain the body surface potential map (BSPM). The 12-lead ECG was then calculated by operations of potentials at the ECG electrodes displayed by red dots in Figure 2.12.

The following equation is established for surface potential calculation by applying Green’s theorem to the torso surface:

$$\Phi(\vec{r}) = \frac{1}{4\pi\sigma} \int_v \vec{J} \cdot \nabla(1/r) dv + \frac{1}{4\pi} \int_s \Phi(\vec{r}) \nabla(1/r) ds \quad (2.18)$$

where Φ is the body surface potential, \vec{J} is the cell dipole, r is the distance from the surface location to the dipole and σ is the extracellular conductivity.

An intermediate value $\psi = \phi - \phi^0$ is introduced to transform the Poisson equation

with respect to Φ , into a Laplace equation with respect to Ψ , satisfying the boundary condition of

$$\frac{\partial \Psi}{\partial n} = \frac{\partial \phi^0}{\partial n} = -q^0 \quad (2.19)$$

where Φ and Φ^0 are potentials with and without boundary conditions, respectively. n represents the normal direction of body surface.

Applying the boundary element method with respect to Ψ leads to the following integral equation:

$$\int_{sb} \Psi \frac{\partial G}{\partial n} dS = - \int_{sb} q^0 G dS \quad (2.20)$$

where G is the Green function. Discretization of (2.20) leads to the simultaneous equations:

$$\sum_{n=1}^N h_{mn} \varphi_n = - \sum_{n=1}^N g_{mn} q_n^0 \quad m = 1, 2, \dots, N, \quad (2.21)$$

where h_{mn} and g_{mn} are coefficients related to the torso geometry, and N is the quantity of triangles that form the torso surface. The following condition:

$$\sum_{n=1}^N a_n \psi_n = - \sum_{n=1}^N a_n \phi_n^0 \quad (2.22)$$

is added to ensure a unique solution of equation (2.21), where a_n is a linear function to the area of a triangle that has a vertex n . This condition is for the purpose of defining a potential reference so that the integral of surface potential is zero. By adding (2.22) to (2.21) we get the equation in matrix notation:

$$\mathbf{H}\Psi = -\mathbf{G}\mathbf{Q}^0 - \mathbf{A} \quad (2.23)$$

And the final solution for surface potentials is obtained by:

$$\Phi = \Phi^0 - \mathbf{M}\mathbf{Q}^0 - \mathbf{P}^0 \quad (2.24)$$

where $\mathbf{M} = (\mathbf{H}^T \mathbf{H})^{-1} \mathbf{H}^T \mathbf{G}$ and $\mathbf{P}^0 = (\mathbf{H}^T \mathbf{H})^{-1} \mathbf{H}^T \mathbf{A}$.

Panel A in Figure 2.13 shows three examples of calculated BSPM during a sinus rhythm. Panel B is the corresponding 12-lead ECG waveforms comparable to clinical ECG.

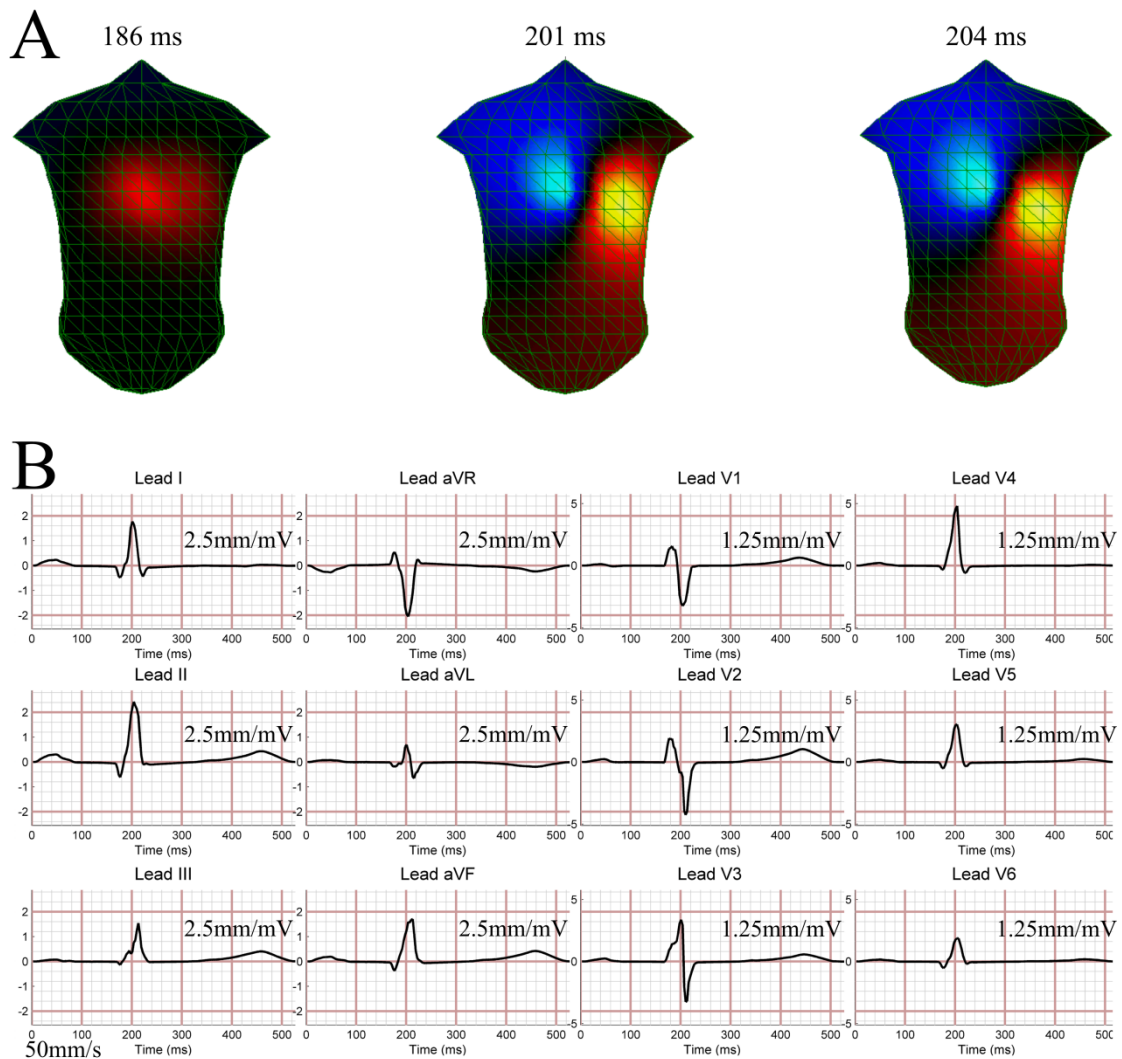


Figure 2.13 The simulated body surface potential maps (BSPM) of a sinus rhythm and its ECG. (A): snapshots of potential distributions taken at three moments: 186 ms, 201 ms and 204 ms. (B): the corresponding simulated 12-lead ECG waveforms.

2.4 Studies based on the Wei–Harumi whole-heart model

As a state-of-the-art heart model, the Wei–Harumi model is a versatile and ideal platform to help researchers get important findings. Although each simulation study performed on this model shares the same heart anatomy and torso shape, different heart models can be created by assigning different electrophysiological parameters to different model cells. Based on this heart model, Wei *et al.* simulated the Wolff-Parkinson-White (WPW) syndrome [128] and further investigated the supraventricular tachycardia related to the WPW syndrome [129]. The possibility of

using the Laplacian maps to predict accessory pathways locations in the WPW syndrome was also validated [138]. Clinically comparable bigeminy, trigeminy, quadrigeminy and other types of ECG were simulated [84]. This model was also used to evaluate effects of antiarrhythmic drugs [83]. Watanabe *et al.* used this model to verify their clinical findings that activation-recovery intervals and restitution properties were responsible for the induction of ventricular arrhythmia in heart failure [85]. Ryzhii *et al.* successfully simulated an atypical Brugada syndrome in the Wei–Harumi model [130]. In 2012, Zhu *et al.* reported their work of clinical electrophysiological study (EPS) as a clinical application of heart models [133].

These researches strongly suggest that the Wei–Harumi model is right for studying VF. The work of this dissertation is standing on the shoulders of giants.

Chapter 3 Effect of Action Potential Duration Restitution Slope on the Vulnerability to Ventricular Fibrillation Induction

3.1 Background and research target

In Chapter 1, we briefly reviewed reported work regarding the relationship between action potential duration (APD) restitution and stability of excitation propagation. According to Weiss *et al.* [64], when the spiral waves existing in ventricular tachycardia (VT) become unstable, wavebreak may occur and consequently VT may degenerate into ventricular fibrillation (VF). It is reasonable to deduce that APD restitution (APDR) is related with VF genesis. In fact, literatures have suggested that APDR is relevant to stability of cardiac electrophysiology and vulnerability to VF both in vivo [139, 140] and in vitro [141]. Such conclusion was further confirmed in simulations (inducibility of reentry) [60, 99, 101]. Nash *et al.* combined clinical study with simulation to reemphasize the significance of APDR [100]. Researchers have also shown the possibility of eliminating ventricular fibrillation by flattening APDR [67, 101] that may facilitate inventions of novel antiarrhythmic pharmacy.

Work from physicians indicates that high-risk patients with inducible VT or alternant TWA are connected with steeper APDR slope over that of low-risk patients [140]. This inspired us to take advantage of the Wei–Harumi model to determine whether steeper APDR slope links to a higher risk of VF. Figure 3.1 shows a representative endocardial APDR with a steep slope.

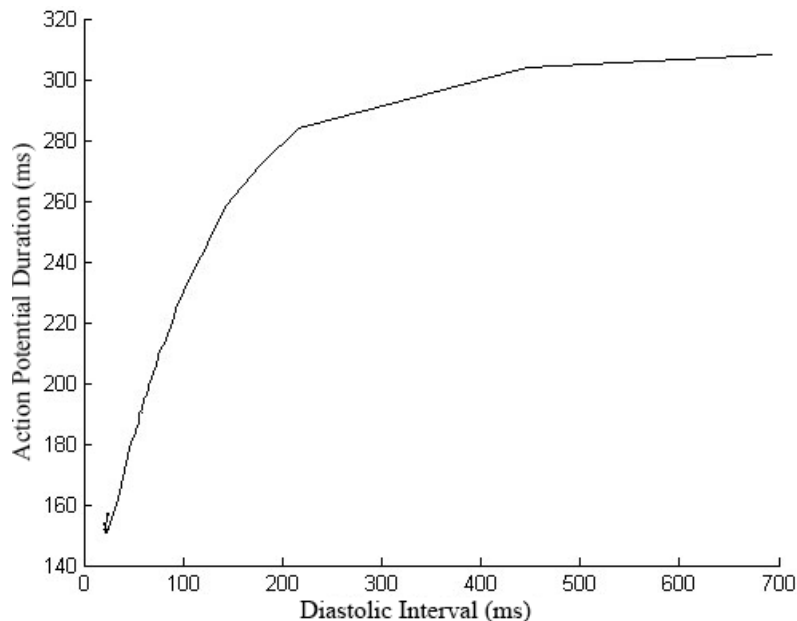


Figure 3.1 An endocardial APDR derived from ten Tusscher’s cellular model [32]. This curve is obtained by applying stimuli of 1 ms duration to the cell model using dynamic restitution protocol [62]. The stimulation strength is twice diastolic threshold.

3.2 Electrophysiological parameters used in the model

The original setting of the Wei–Harumi model assumed that the APD variation is linear with increment/decrement of the coupling interval so that during simulation the APD of a model cell is dynamically determined by equation (3.1) [13]:

$$APD(t) = APD(t-1) + DC \cdot \Delta CI(t) \quad (3.1)$$

where $\Delta CI(t)$ is the increment of coupling interval (CI) at time t , DC is a dynamic coefficient (see “Action Potential” part in Table 2.1) defined as the ratio of change in APD to $\Delta CI(t)$. CI is actually the cycle length (CL) of applied stimulus. In other words, APDR of the original Wei–Harumi model is CL-dependent.

Researchers have found that while pacing some cardiac cells at a relatively long interval, each activated action potential by corresponding stimulation is identical (called 1:1 behavior), after the pacing rhythm exceeds a certain critical rate, APD bifurcation occurs: double periodical stimuli generate two different action potentials: one short, one long [27], and this phenomenon is recognized as APD alternant, considered as one of the potential triggers of unidirectional block which may consequently induces reentry or even arrhythmia [59]. Experts suggest that APD shall

be estimated by its followed diastolic interval (DI) which is the period between onset of applied stimulation and the time when action potential reaches its 90% repolarization [141]. Thus the APDR should be DI-dependent.

The experimental acquired restitution curves (DI versus APD) are usually fitted with mono-exponential functions [100]; while Han *et al.* suggested that piecewise mono-exponential function could reflect the restitution property more faithfully [79]. Nevertheless, a piecewise linear function was adapted in this study to depict APDR for the sake of speedy computation, and this simplicity can hardly hamper simulations from deriving reliable results. Thus the APD of a model cell is determined by:

$$\text{APD} = \begin{cases} \text{Minimum} & \text{DI} \leq \text{DI}_{\min} \\ A_1 \cdot \text{DI} + B_1 & \text{DI}_{\min} < \text{DI} \leq \text{DI}_1 \\ A_2 \cdot \text{DI} + B_2 & \text{DI}_1 < \text{DI} \leq \text{DI}_2 \\ A_3 \cdot \text{DI} + B_3 & \text{DI}_2 < \text{DI} \leq \text{DI}_{\max} \\ \text{Maximum} & \text{DI} \geq \text{DI}_{\max} \end{cases} \quad (3.2)$$

where DI is the preceding diastolic interval. It should be noted that DI can be negative since ectopic stimulations may fall in the action potential when the cell has not reached its 90% repolarization. A and B are slope and intercept of the linear functions.

In the Wei–Harumi model, each cellular absolute refractory period (ARP) is defined by respective constant pluses a gradient difference. However, Michael *et al.* [142] pointed out that under normal conditions, APD90 and ERP was proportional to the cycle lengths, thus in this study ARP is set to be 90% of corresponding APD90. The definition of APD90 is the time between onset of upstroke and 90% repolarization of the action potential [143].

The used restitution data were from a clinical report by Selvaraj *et al.* [140], and they showed that patients with cardiomyopathy (arrhythmia high risk) possessed significantly steeper mean activation recovery interval (equivalent to APD) restitution slopes than that of low-risk patients. The parameters of restitution from different patients are listed in Table 3.1, and are divided into three catalogues according to their locations: Apex, Middle and Base of the heart [140]. Two models using these parameters were studied.

Table 3.1 Parameters of piecewise restitution

Patient	Parameters (millisecond)							
	<i>Location</i>	<i>Minimum</i>	DI_{min}	A_1	B_1	DI_1	A_2	B_2
Low-risk	Apex	260	0	0.57	260	40	0.08	280
	Middle	254	0	0.64	254	25	0.1	267
	Base	255	0	0.36	255	47	0.16	264
High-risk	Apex	186	-50	1.7	270	-7	0.25	260
	Middle	207	-40	1	247	12	0.16	258
	Base	203	-30	1.33	243	10	0.2	254

Patient	Parameters (millisecond) ^a					
	<i>Location</i>	DI_2	A_3	B_3	DI_{max}	<i>Maximum</i>
Low-risk	Apex	125	0	290	300	290
	Middle	125	0.09	269	300	298
	Base	107	0.08	271	300	295
High-risk	Apex	40	0.1	266	300	296
	Middle	135	0.03	276	300	285
	Base	80	0.08	264	300	288

a. Continued

3.3 VF-induction method

VF was induced by pacing with a train of periodical ectopic stimuli applied on the left ventricular epicardium of the heart model (the blue filled dot in Figure 3.2) indicated by the black arrow in Figure 3.2 [18, 19]. The stimulation timing was set to fall in the vulnerable period in order to facilitate inducibility of fibrillation. Fibrillation induction was regarded as successful if morphologically irregular simulated ECG persisted after ectopic impulses stopped. Each simulation lasted 6,000 ms.

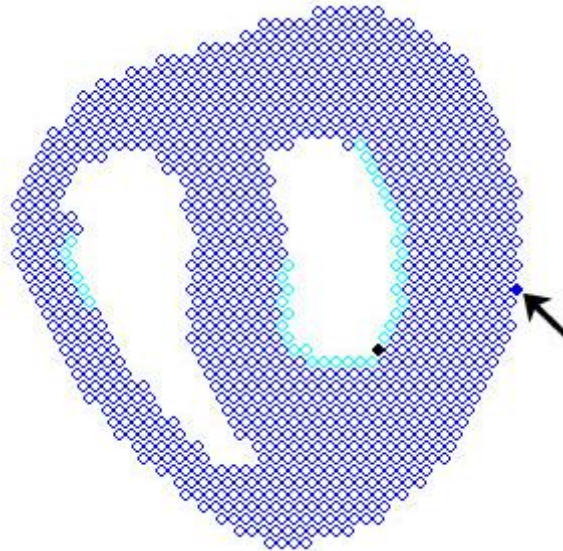


Figure 3.2 Location of the VF-induction ectopy. A cross-section located at about one third from the apex of the heart model is shown. The blue filled dot indicated by the black arrow on the right side shows the position where ectopic stimulation applies.

3.4 Quantity of minimal stimuli required to induce VF

Figure 3.3 shows lead II ECG of sinus rhythm and VF-like rhythm simulated from the two models. The extra-stimuli train started about 470 ms after the first sinus rhythm and its cycle length was slightly above 200 ms, a little longer than ARP. The open arrows in respective diagrams indicate the time of onset and end of ectopic stimuli, sinus impulses continued till the end of simulation.

Apparently the sinus rhythm of both models was identical. For the model with high-risk patient's data, at least 9 successive ectopic stimuli were required to induce fibrillation; while in contrast, the other one model demanded at least 13 stimuli.

If ectopic stimuli were insufficient, the heart model could restore sinus rhythm by itself as shown in Figure 3.4, suggesting that heart model with a less steep APDR is more robust against arrhythmogenesis. This is consistent with conclusions of those simulations which have proven that reentry can be terminated by flattening APDR curve [83, 130].

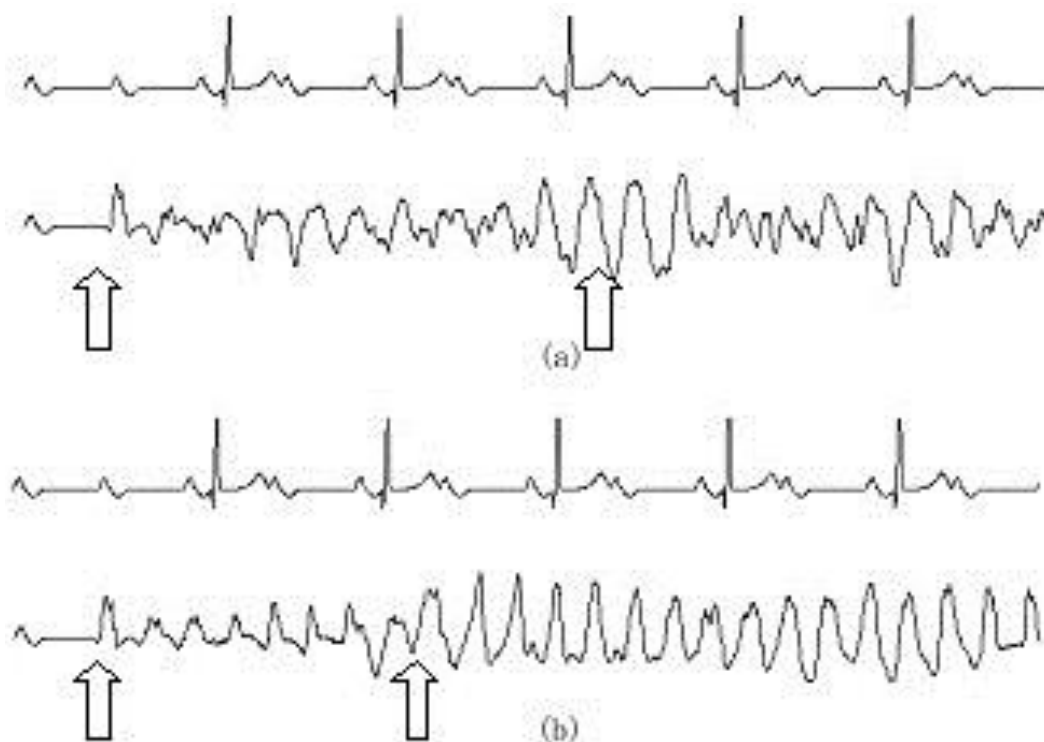


Figure 3.3 Lead II ECG of sinus rhythm and VF-like rhythm. The irregular rhythm was induced by minimum ectopic stimuli in heart models using parameters from respective patients. The upper panel indicates ECG of heart model with low-risk patient's data, and the lower one indicates ECG simulated in model with high-risk patient's data. The open arrows in the picture indicate onset and retreat moments of ectopic simulations in respective models. Note that the minimum required ectopy to induce VF of the model with high-risk patient's data is significantly less than that of the model with low-risk patient's data.



Figure 3.4 Insufficient ectopic stimuli led to failure of VF induction. An unsuccessful induction in the heart model with high-risk patient's data is shown. As soon as the ectopic stimuli ended, the simulated rhythm automatically restored normal sinus rhythm.

3.5 Discussion and conclusions

During VF, each cell's DI is very short and thus its restitution slope is sharp. Since restitution slope declines as the DI increases, the nonlinear dynamic control method can be utilized to manipulate DI and move the electrical activity into flat restitution

region, consequently stabilize kinetics of the electrical activity. Such protocol was certified with feedback feature and proven feasible [144]. These findings may facilitate future electrical therapy against arrhythmia and even dramatically reduce conventional defibrillation energy.

Previously Yamaki *et al.* [86] used the Wei–Harumi model to study how restitution may affect arrhythmogenesis and came up with a similar conclusion as our current study. In this chapter, feasibility of inducing VF in the Wei–Harumi model with DI-dependent APD restitution was proven and yielded results agreed with clinical findings. We find that the heart model with steeper restitution is more vulnerable to ectopy, thus the restitution slope may play an important role in studying VF inducibility.

As described by Weiss *et al.* [59]: steep restitution induces APD alternans, forms spatially distributed refractory period differences, and amplifies the variations of existed heterogeneity. It is quite likely that heart models with steep restitution are vulnerable to VF induction because steep restitution increases the electrophysiological heterogeneity of the heart which is thought to be an essential substrate for inducing reentry and even arrhythmia [145].

Chapter 4 Effects of Ventricular Fibrillation Induction Configurations on Induced Ventricular Fibrillation Organizations

4.1 Ventricular fibrillation induction protocols

As mentioned in Chapter 1, we have to induce ventricular fibrillation (VF) in heart models prior to studying VF because virtual hearts do not have spontaneous VF. To induce VF in animal experiments, human trials or computer models, the stimulation delivery protocol, the pacing site and the stimulation amplitude are some key issues.

The first issue, VF-induction protocols can be briefly divided into three catalogues: alternating current (AC) induction [146, 147], direct current induction [148] and pacing induction [67]. The AC induction has been proven to be less realistic than the pacing induction [149], which includes burst pacing protocol [15, 56], S1S2 protocol [80] (also called T-shock [149] or cross-field stimulation [15]), and a newly emerged pacing sequence proposed by Otani [73]. For the second issue, some researchers suggest that the general clinical VF-induction sites are the right and left ventricular outflow tracts (RVOT and LVOT), and the right ventricular (RV) apex [65, 150]. Keldermann *et al.* reported an interesting finding that the induced VF patterns were related with the induction sites, where core of the initial scroll wave was located [94]. Simulation amplitude, the third issue, is usually twice diastolic threshold [67].

Considering the diversity of VF-induction methods, it is necessary to determine whether different induction methods change the patterns of induced VF because it is impractical to implement all VF-induction methods in one research. In this research, we applied several pacing protocols at different sites of the Wei–Harumi heart model [13, 82] to check the impacts of induction methods and sites on induction results and patterns of induced VF.

4.2 Model settings and VF-induction configurations

4.2.1 VF-induction protocols and sites

We employed the S1S2 protocol, the burst pacing protocol [83, 130, 151] and the protocol proposed by Otani [73] in this study as VF-induction protocols.

The S1S2 protocol was composed of a train of S1 stimuli pacing at a constant cycle length followed by a premature S2 stimulation timed to fall in vulnerable period of the last S1 impulse [114]. It is widely used to introduce spiral waves in two-dimensional cardiac tissues [32, 80, 101] and scroll waves in three-dimensional models [94, 114].

The sequence of burst pacing protocol comprises a series of ectopic stimuli at a constant cycle length interacting with underlying sinus rhythm; delivery timing of the ectopic stimulation is set to be immediately after absolute refractory period (ARP) of the model cell at the place where ectopic stimulation applies.

The Otani's protocol [67, 73] provides a “blocking condition”, which suggests that there are sequences of irregularly timed stimuli that guarantee propagation failure at a finite distance from the excitation source even through the tissue is homogeneous, and their intervals can be calculated with the equation 1 in Otani [73] for the tissue with a certain combination of action potential duration (APD) restitution and conduction velocity (CV) restitution. Because it was difficult to calculate all optimal intervals, only intervals among S1-S5 were calculated. If this sequence could not induce VF, then additional stimuli immediately after the end of ARP would be appended. If over 6 additional stimuli were appended, the induction was considered to be unsuccessful because this sequence was nearly the same as the burst pacing.

The pacing sites were the RVOT, endocardium of the RV apex (Endo-RV), epicardium of the RV apex (Epi-RV), and the lateral left ventricular (LV) epicardium extended from the heart base for about a quarter of the apicobasal dimension [83, 130, 151] (see Figure 4.1). For the S1S2 protocol, S1 induction site was near the atrioventricular node, and S2 was applied at the two sites used by Keldermann *et al.* [94] at areas with APD restitution (ADPR) of either high or low slope.

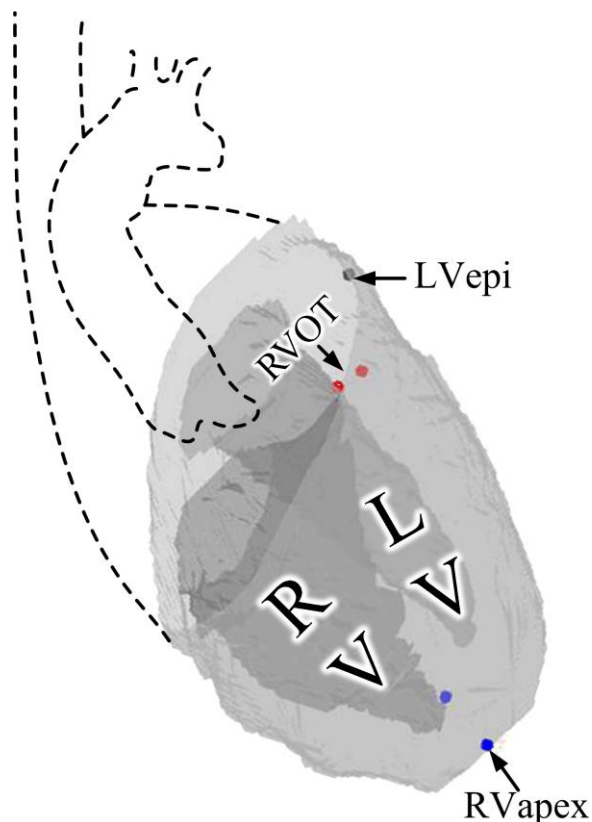


Figure 4.1 An illustration of VF-induction sites. The figure shows an anterior-posterior view of the ventricles (contour lines of some other not-shown anatomical parts are shown in dashed lines). The blue dots indicate endocardium and epicardium of the RV apex sites, the red dots show the RVOT pacing places, and the black dot is the induction site on the lateral LV epicardium. Key: RV = right ventricle, LV = left ventricle, RVOT = right ventricle outflow tract, LVepi = LV epicardium.

The quantity of stimuli was adjusted in order to make sure only minimum ectopic pulses were sent to induce VF. Induction was considered to be successful as long as irregular simulated ECG persisted after withdrawal of the VF-induction pacing [147]. An entire simulation lasted about 6,000 ms.

4.2.2 APD and CV restitution

The integrated APDR curves were generated by fitting clinical data provided by Selvaraj *et al.* [152]. They measured endocardial restitutions in three regions: apex, middle, and base of the ventricles from two groups of patients called the low-risk and high-risk patients. Data from the former group were used in this study. The used LR I_{Na} CVR curve was from simulation results (see Fig. 8 in ten Tusscher *et al.* [32]) generated by stimulating one-dimensional strain of human cardiac cells *in silico*.

The restitution data were then fitted with the following mono-exponential function [62, 67, 153] which showed an accurate fitting to clinical data [100]:

$$APD(CV) = APD_{ss}(CV_{ss}) - A_{APD}(A_{CV}) \cdot \exp(-DI/B_{APD}(B_{CV})) \quad (4.3)$$

where APD_{ss}/CV_{ss} is the steady-state APD/CV (SS in Table 4.1), A and B are parameters of the fit, DI is the preceding diastolic interval. If the DI exceeds the range specified by the top and bottom values (see Table 4.1 for the specified values), the DI's value is replaced by the top (or bottom) value.

Table 4.1 Parameters of exponential restitutions

Restitution	Parameters ^a					
	Location	Bottom (ms)	SS	A	B	Top (ms)
APD (ms)	Apex	2	270.4	29.27	39.52	209.5
	Middle	0	265.9	30.5	63.25	212.2
	Base	2	264.5	29.9	56.1	212.1
CV (cm/s)	All	23.3	67.1 ^b	39.2	27.1	400

a. The unit of bottom, top and APD_{ss} is millisecond

b. The unit of CV_{ss} is centimeter per second

4.3 Results of induction by different configurations

Table 4.2 is an overview of the induction results. Surprisingly, the S1S2 protocols failed to induce any sustainable VF: after 8 pacing stimuli, S2 stimulation slightly disturbed the ECG waveform but did not induce any irregular ECG (see Figure 4.2).

Table 4.2 Overview of the induction results

VF-induction Protocol	Sites of Ectopy ^a			
	LV	RVOT	Epi-RV	Endo-RV
S1S2	Fail	Fail	Fail	Fail
Burst Pacing	Sus ^a	Sus	Sus	Fail
Otani's protocol	Sus	Sus ^b	Fail	Fail

a. Sustainable VF was induced

b. Pacing site was on the epicardium

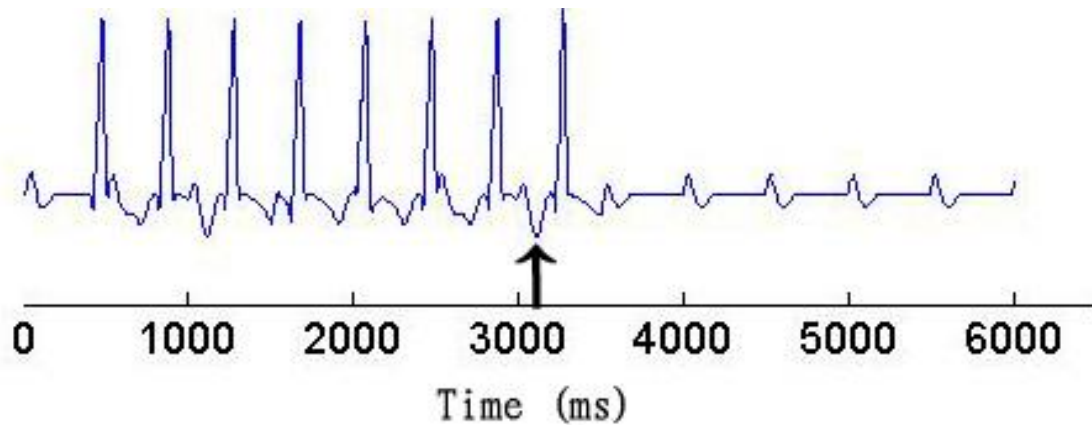


Figure 4.2 A representative ECG strip showing that S1S2 protocol failed to induce VF. Only lead II is displayed. The black arrow points out the time when S2 was applied and the succeeding ECG simply generated another QRS complex but there was no onset of VF.

Both the burst pacing and the Otani's protocol could induce sustainable irregular rhythm at the left LV epicardium. The Otani's protocol failed to induce VF at the RVOT, but when the induction site was changed to a corresponding epicardial site (the red dot on the epicardium in Figure 4.1), the induction became successful. The burst pacing protocol managed to induce sustainable irregular rhythm at the RVOT. The Otani's protocol failed to induce VF at epicardium of the RV apex because at least 8 additional stimuli were required to induce sustainable VF. Interestingly, neither of these two protocols induced sustainable VF at endocardium of the RV apex: the ECG trace showed no sign of ventricular electrical activity (only P waves presented due to atrioventricular block) after several waveform oscillations as illustrated in Figure 4.3.

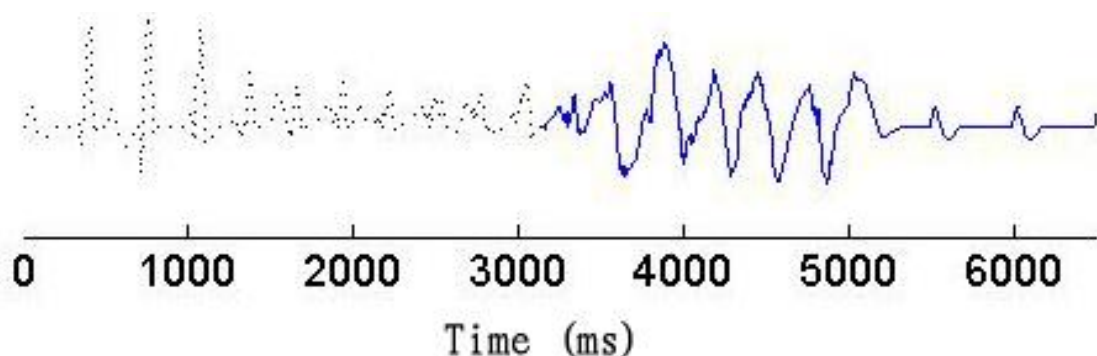


Figure 4.3 A representative ECG strip showing induced unsustainable VF. The lead II ECG of a VF-induction by the Otani's protocol is shown. The dashed line shows the waveforms when ectopy was applied. The solid line shows the unsustainable VF, whose irregular morphological waveforms disappeared after several peaks.

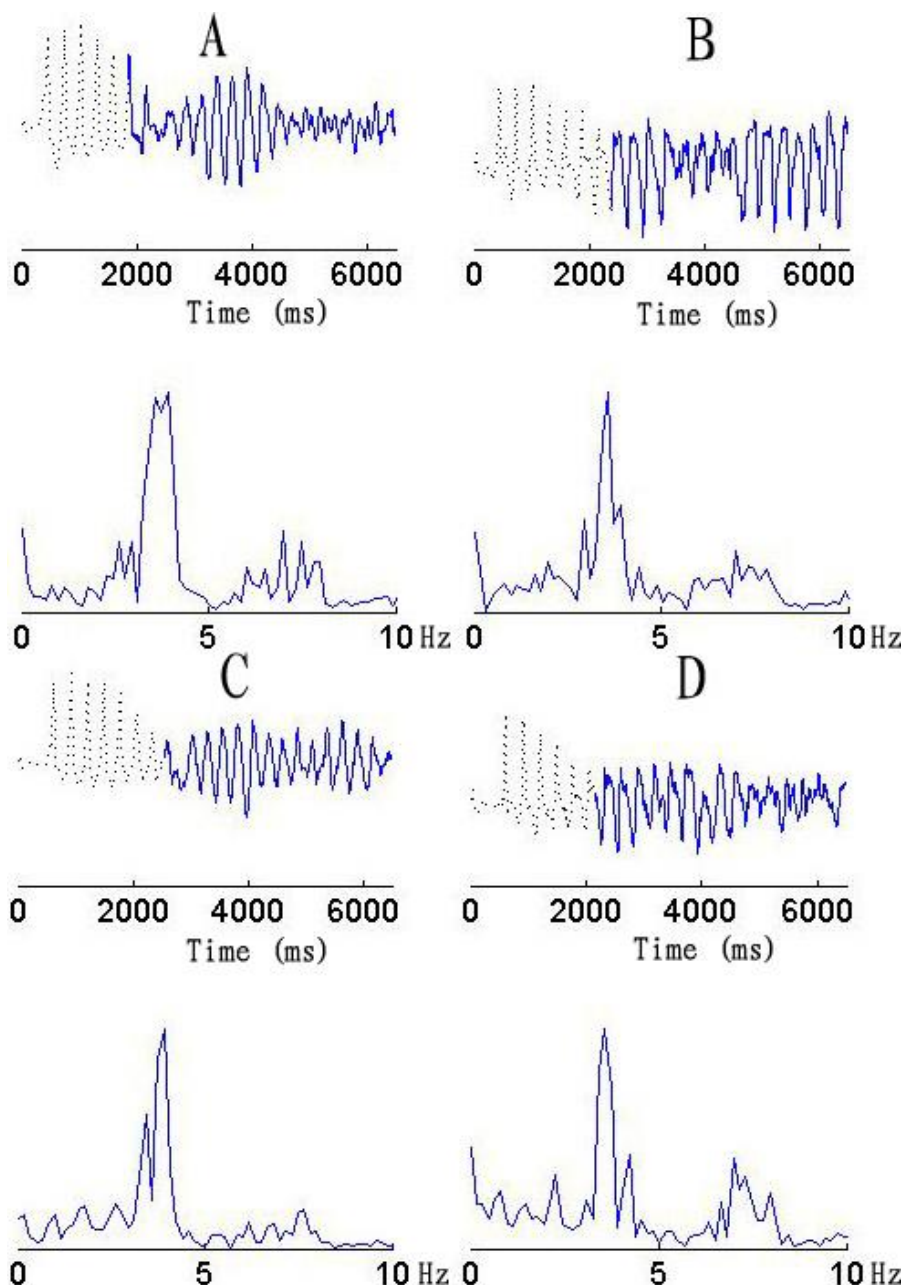


Figure 4.4 ECG waveforms and spectra of four induced VF episodes. The upper panels show traces of lead II ECG and the lower panels show the corresponding spectra. The dashed lines show the ECG during VF-inductions. (A): VF induced by Otani's protocol applied at a corresponding epicardial site of the RVOT. (B): VF induced by Otani's protocol applied at the lateral LV epicardium. (C): VF induced by burst pacing applied at the RVOT. (D): VF induced by burst pacing applied at the lateral LV epicardium.

The successfully induced VF episodes are illustrated in Figure 4.4. Figure 4.4A and B are VF episodes induced by the Otani's protocol, and Figure 4.4C and D are VF episodes induced by the burst pacing. Figure 4.4A and C are VF episodes induced by pacing at the RVOT (or a corresponding epicardial site of the RVOT), and the other

two episodes are induced by pacing at the left LV epicardium. The upper panel of each subfigure shows the simulated ECG; ECG during the period when induction pacing was applied is shown by dashed lines and ECG after that is shown by solid lines. The lower panel of each subfigure shows the corresponding power spectrum of respective ECG.

Figure 4.4A and C show that the simulated ECG of VF episodes induced at the RVOT site are relatively neat while the other two are relatively coarse. The four ECG spectra have a similar dominant frequency of approximately 4 Hz, therefore the patterns of these four VF episodes are almost the same despite of subtle differences in ECG morphology, and their similar spectral distributions are quite likely due to their identical inner restitution properties [75].

4.4 Induction configurations and VF patterns

Keldermann *et al.* [94] showed that the patterns of induced VF episodes were site-related: if the induction pacing was placed at an area with steep APDR, it induced VF with organizations of multiple-wavelet propagation while induction at an area with shallow APD restitution induced mother-rotor patterns. In this study, we performed VF simulations through combining VF-induction protocols and sites based on the Wei–Harumi whole heart model. The relationship between induction site and VF pattern was not supported by this research because all induced VF episodes showed a phenomenon of mother-rotor VF pattern regardless of induction configurations. This might be due to the fact that their integrated restitution was relatively shallow and the sites which successfully induced VF were in regions with very shallow APDR. However, neither did simulations conducted in models with an artificially steep APDR (not shown) show the same observation as Keldermann *et al.*'s research [13]. It is quite likely due to the differences between these two heart models. For example, propagation principle of the Wei–Harumi model is Huygens' Principle, while that of the other one is based on diffusion-reaction equations.

4.5 The induction configurations and the probability of inductions

Our simulations showed the combination of VF-induction protocols and sites affected the probability of successful induction: the S1S2 protocol could not induce VF, and ectopic pacing at endocardium of the RV apex could only induce unsustainable arrhythmia (see Figure 4.3) in our simulations. Only burst pacing could induce VF at epicardium of the RV apex. Interestingly, once the VF was triggered, its pattern was relatively stable and showed no induction-method dependence.

Weiss *et al.* [59] showed that although ventricular ectopy was very common in patients with reduced ejection fraction (<35%), the odds of inducing fatal arrhythmia is quite low. They showed that the ectopic stimulation could possibly trigger reentries only when the preexisted heterogeneity was large enough, in other words, the heart was robust against arrhythmogenesis. In this research, VF-induction configuration should be tricky enough in order to trigger sustainable VF. If intervals among stimuli were not proper values or pacing sites were not inducible places, the heart could restore normal rhythm after induction pacing stopped. This is consistent with the finding of Weiss *et al.* [59].

4.6 Summary and conclusions

In this research, we performed VF inductions using three pacing protocols at three pacing sites. Some combinations of pacing protocols and sites failed to induce self-sustainable VF and the reason for the failures needs further investigations. Only certain combinations of protocols and sites could trigger self-sustainable VF, and once VF was induced, the induced VF pattern was determined by the intrinsic properties instead of the VF-induction methods. Propagation analysis of the simulations demonstrated that before a successful induction, the excitation propagations were blocked at a distance from the pacing site and thus created gradients of depolarization time among adjacent cells. When the gradients passed a certain threshold, the induced arrhythmia became self-sustainable. This phenomenon was observed in VF inductions by the Otani's pacing protocol and the burst pacing.

Our result is useful in studying VF mechanisms. Since there are a lot of VF-induction methods, it is impractical to implement all of them at a time, especially in animal experiments or human trials. If VF is independent of induction methods, then using an arbitrarily selected induction method is enough, because the pattern of VF induced by other induction methods will be almost the same.

Chapter 5 Effects of Cardiac Restitutions on Ventricular Fibrillation

The simulation results of Chapters 3 make us believe that cardiac restitution is related to ventricular fibrillation (VF). According to the conclusion of Chapter 4, we realize that this relationship is independent of VF-induction configurations. Based on these findings, we presume that cardiac restitutions can be key factors that determine VF dynamics.

5.1 Mechanisms of ventricular fibrillation revisiting

The mechanism underlying VF has been a topic of intense research for a long time [11]. As discussed in Chapter 1, the multiple-wavelet [48] and the mother-rotor [49] hypotheses are considered as two major but contradictory hypotheses that account for the mechanism of VF. However, neither multiple-wavelet nor mother-rotor hypothesis can satisfyingly explain existing experimental and clinical observations. In addition, the mechanism(s) responsible for the degeneration from reentrant ventricular tachycardia (VT) to VF, conventionally believed to be due to a different mechanism, is neither fully understood [154].

As described in Chapter 1, Wu *et al.* suggested that there were two types of VF [75], and postulated that both conduction velocity (CV) restitution and action potential duration (APD) restitution were important in VF maintenance and verified their hypothesis in a three-dimensional cardiac tissue slab [78]. Since the shape of the real heart is not a slab, the hypothesis tested by simulations in a cardiac tissue slab [78], that space-time dependent APD restitution (APDR) and CV restitution (CVR) can significantly influence VF organization and conversion, needs further validation using whole-heart models with realistic heart shapes, because anatomical features can significantly influence wave instability [109]. If both APDR and CVR are indeed important determinants of VF behavior, the manifestations of VF induced in models

with certain APDR and CVR could reflect these restitution properties. Moreover, the multiple-wavelet VF, the mother-rotor VF and VT would be reproduced in models with corresponding restitution configurations. Furthermore, the transitions from multiple-wavelet VF to VT, to mother-rotor VF from restitution alterations could also be simulated.

Several studies based on whole-heart models have already investigated the relationship between cardiac restitutions and VF organization. Xie *et al.* [109] investigated the influence of the APDR slope on VF patterns in a canine ventricular model (by varying the parameter that controls the Ca^{2+} current amplitude, G_{si}), but didn't investigate the effect of the CVR on VF. ten Tusscher *et al.* [14] tested several factors, including excitability and APDR that determine the number of rotors during VF. Nevertheless, the effects of these factors were only studied individually without investigating the combined action of APDR and CVR in influencing the VF organization. Keldermann *et al.* [94, 114] have successfully reproduced both multiple-wavelet and mother-rotor VF in a detailed human ventricular model. However, they only investigated the effects of APDR heterogeneity and VF-induction site on the VF dynamics. To the best of our knowledge, few simulation studies based on a human whole-heart model have been implemented so far to verify the deduction that multiple-wavelet VF, VT, and mother-rotor VF are probably just the different appearances of corresponding APDR and CVR properties, and their mutual conversions are due to changes in restitution. The purpose of this study was to check the role of APDR and CVR in exploring the mechanism of VF [64].

5.2 Simulation method

We used the Wei–Harumi whole-heart model, a “rule-based” model that contains a detailed description of cellular electrophysiology and cardiac anatomy [13, 82] in this study. Its effectiveness is proven by many recognized publications based on this model [130, 133]. We enhanced this model's spatial resolution to a finer level of 0.5 mm×0.5 mm×0.5 mm by fissuring each model cell into 27 identical model cells. Also,

the time step of excitation propagation calculation was changed to 1 ms. Unlike the models reviewed in the previous session, our model included the His–Purkinje system, which is considered to play an important role in initiation and maintenance of VF [10, 65, 155]. Details and features of this model are provided in Chapter 2, session 2.3.

5.2.1 Electrophysiological settings

We used the APDR and CVR curves in previous publications as an “input” into the Wei–Harumi model. During the simulations, the model cells are assigned time-varying APD and CV according to their APDR, CVR, locations in the model, and diastolic intervals (DI). The validation of these restitution settings was carefully performed by simulating cardiac processes consistent with clinical reports [156, 157]. The APDR and CVR inputted are described below.

The APDR curves were derived by fitting the clinical discrete data published by Selvaraj *et al.* [140] to a mono-exponential function [100], as shown below in (5.1):

$$\text{APD} = \text{APD}_{\text{ss}} - A \cdot \exp(-\text{DI}/B) \quad (5.1)$$

where APD_{ss} is the steady-state APD, A and B are the fitting parameters, and DI is the preceding diastolic interval defined as the amount of time spent recovering prior to an applied stimulus.

Selvaraj *et al.* defined two data sets recorded from two groups of patients designated as “High-Risk” and “Low-Risk” [140], with each set containing APDR at the apex, middle, and base of the right ventricular (RV) endocardium. Hereinafter, the APDR fitted from the High-Risk and Low-Risk groups’ data sets will be referred to as “steep” and “shallow” APDR, respectively (see Figure 5.1, only the APDR curves at the apex are shown, whose maximum slopes are 1.85 and 0.55, respectively). During the simulation, the effective refractory period (ERP) was part of the APD as introduced in session 5.2.2 below, and a ventricular model cell could not be excited by its neighboring model cells if it was in its ERP.

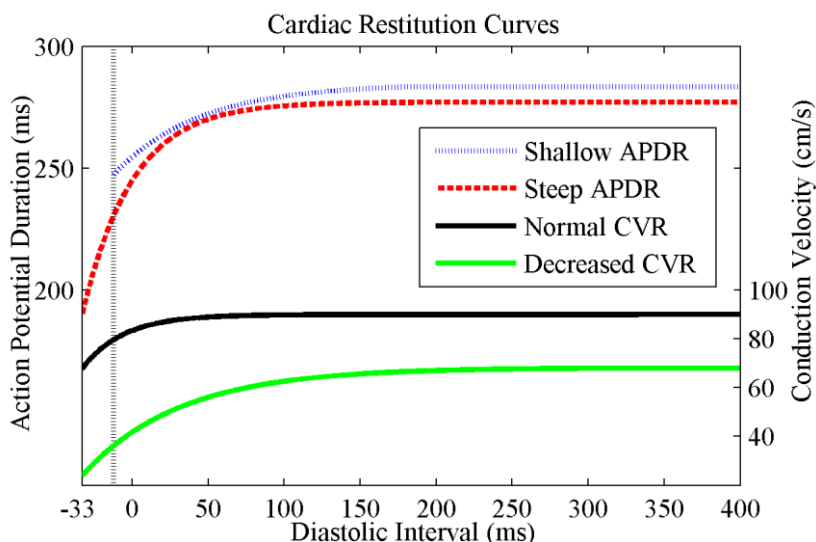


Figure 5.1 The APDR and CVR curves adopted. The dashed lines represent shallow/steep APDR at the apex with a maximum slope of 0.55/1.85, and the solid lines represent CVR. The vertical dotted line denotes the DI of a shallow APDR.

The CVR curves were also depicted using a mono-exponential function similar to (5.1). The sources for the CVR were data from the results of ten Tusscher *et al.* [32] obtained from simulations using a strain of human myocyte model. There were three curves provided in ten Tusscher *et al.* [32], and two of them were adopted in this study: the standard I_{Na} and the LR I_{Na} CVR curves (obtained from simulations using models with standard and Luo–Rudy (LR) fast I_{Na} dynamics [32], respectively). Both curves were left-shifted by about 56 ms in the abscissa so that the minimum DI value in the latter curves was aligned with the minimum DI value of the steep APDR curve (−33 ms). In addition, the LR I_{Na} restitution curve was scaled up by a factor of 30% to make its steady-state value become 90 cm/s. The transformed LR I_{Na} or standard I_{Na} CVR data (resembling a flat CVR or a steep CVR with a broader span in Wu *et al.* [75]) represent physiologically normal excitability or decreased excitability of the cells. Hereinafter, these two CVR will be referred to as “normal” and “decreased” CVR, respectively. During the simulation, the CVR determines the myocyte longitudinal CV dynamically, and the value of CV of an excited cell determined the extent that it could influence. The two solid lines in Figure 5.1 show both transformed CVR curves. Note that these two curves are comparable to CVR acquired from clinical trials [158].

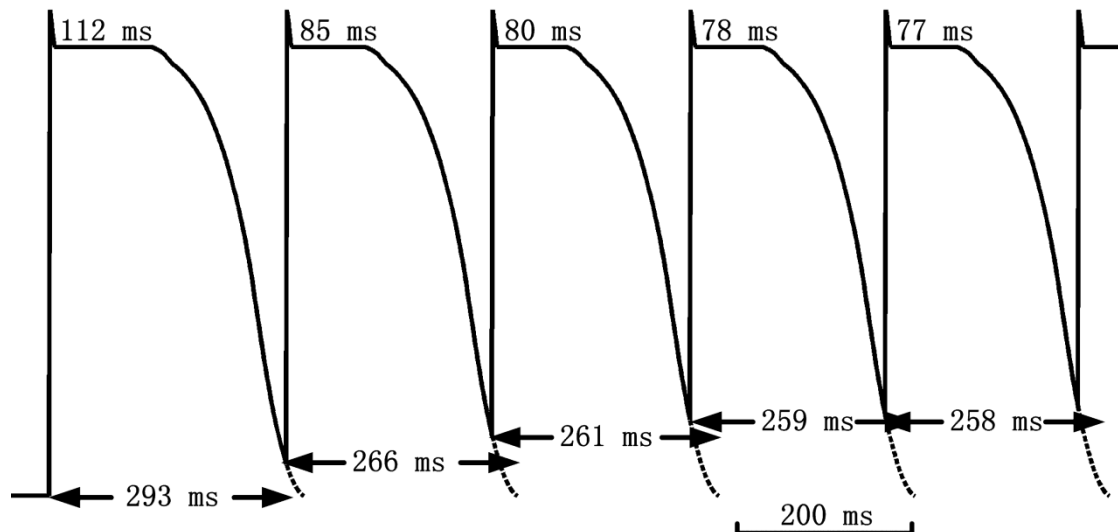


Figure 5.2 An illustration of consecutive simulated action potentials triggered by repetitive extrastimuli. Note that the capture gradually becomes earlier during the preceding repolarization phase (encroachment of extrastimuli on the preceding repolarization phase, marked by the double-arrows) [157]. Also the APD (its value is the number inside double-arrow) decreases reflected by the shrinkage of plateau phase (its value is the number on the plateau phase).

5.2.2 The effective refractory period

It is known that the ERP is well related to activation recovery intervals (ARI, a good surrogate of APD [159, 160]) in the absence of pharmacologic interventions. In this study, ERP of a model cell was dynamically determined by subtracting certain time from corresponding APD. The amount of shrinkage from APD to ERP (designated as ΔAE , and $ERP = APD + \Delta AE$) was a piecewise function (see expression (5.2)) of DI in order to mimic the progressive encroachment onto the preceding repolarization phase of extrastimuli [157].

We assumed that the shallow APDR had less negative ΔAE (less absolute value) according to the data from Selvaraj *et al.* [140] (see the vertical dotted line in Figure 5.1). Figure 5.2 shows the simulated gradual elevation of repolarization level from which action potential can be provoked thanks to consecutive extrastimuli. Each extrastimulation was delivered as soon as ERP ended. Note that the minimum DI depends on ERP and APD [140]. Figure 5.2 also shows the simulated gradual shrinkage of APD that is represented by plateau phase shortening.

$$\Delta AE = \begin{cases} \Delta AE_{\max} & \text{if } DI \geq S1 \\ \Delta AE_{\max} - (S1 - DI) \times Slope1 & \text{if } S1 > DI \geq S2 \\ \Delta AE_{\max} - (S1 - S2) \times Slope1 - (S2 - DI) \times Slope2 & \text{if } S2 > DI \geq S3 \\ \Delta AE_{\min} & \text{Otherwise} \end{cases} \quad (5.2)$$

For models with steep APDR, the ΔAE_{\max} , ΔAE_{\min} and S1-S3 are -21 ms, -33 ms, 39 ms, -21 ms and -27 ms respectively; for models with shallow APDR, the ΔAE_{\max} , ΔAE_{\min} and S1-S3 are 0 ms, -12 ms, 60 ms, 0 ms and -6 ms respectively. Slope1 and Slope2 are 0.1 and 1 respectively.

Table 5.1 Restitution settings of defined time-invariant models ^a

<i>Model</i> \ <i>Chamber</i>		<i>Right Ventricle</i>		<i>Left Ventricle</i>	
<i>No</i>	<i>Naming</i>	<i>APDR</i>	<i>CVR</i>	<i>APDR</i>	<i>CVR</i>
<i>1</i>	<i>Steep decreased</i>	<i>Steep</i>	<i>Decreased</i>	<i>Steep</i>	<i>Decreased</i>
<i>2</i>	<i>Steep normal</i>	<i>Steep</i>	<i>Normal</i>	<i>Steep</i>	<i>Normal</i>
<i>3</i>	<i>Shallow decreased</i>	<i>Shallow</i>	<i>Decreased</i>	<i>Shallow</i>	<i>Decreased</i>
<i>4</i>	<i>Shallow normal</i>	<i>Shallow</i>	<i>Normal</i>	<i>Shallow</i>	<i>Normal</i>
<i>5</i>	<i>Hybrid decreased</i>	<i>Shallow</i>	<i>Decreased</i>	<i>Steep</i>	<i>Decreased</i>
<i>6</i>	<i>Hybrid-reverse decreased</i>	<i>Steep</i>	<i>Decreased</i>	<i>Shallow</i>	<i>Decreased</i>

a. See Figure 5.1 for the representative restitution curves.

5.2.3 Models with different restitutions

Table 5.1 lists the cardiac restitution settings of six different models used in our simulations. It is known that there are different types of electrophysiological heterogeneities in human ventricles, such as the apicobasal gradient, the transmural gradient, and the left–right ventricular heterogeneity [100, 158]. These heterogeneities have been proven to play an important role in developing ventricular tachyarrhythmia [94]. The settings of the transmural and apicobasal APD gradient have been described in Chapter 2, session 2.3.3, and the left–right ventricular heterogeneity was modeled

in a simplified manner by assigning different sets of APDR to the left ventricle (LV) and RV (Models 5 and 6 in Table 5.1, respectively), according to clinical findings that the mean APDR slope of the LV can be significantly steeper [158] or shallower [100] than that of the RV. For simplicity, the electrophysiological properties of other cells were unchanged [82], and other pathological heterogeneities (e.g. necrosis and fibrosis) were omitted.

Furthermore, to model the effect of the admission of D600 in increasing concentrations as reported by Wu *et al.* [78], Model 2 was duplicated (referred to as the “first stage” in Figure 5.6), and its APDR was shallow for a period of ten seconds after removal of any ectopy (referred to as the “second stage” in Figure 5.6), and then eight seconds later the CVR was changed to the decreased CVR (modeling a reduced excitability, referred to as the “third stage” in Figure 5.6). Hereinafter, this model will be referred to as the “time-variant model”, while the other models will be referred to as the “time-invariant models”.

5.2.4 VF induction

The extrastimuli protocol [161] was employed to beget VF. Its sequence comprised a series of ectopic stimuli applied as soon as the cell at the pacing site left its ERP. Stimulation sites was located at lateral LV epicardium extended from the heart base for about a quarter of the apicobasal dimension [83, 130]. Ectopy was removed once the irregular simulated ECG became incessant [147]. Propagations were run for 28 s or terminated if the heart restored sinus rhythm. The cycle length of sinus rhythm was 800 ms.

5.2.5 Measurements of analysis

The fast Fourier transform (FFT) of a VF episode from the twelfth second to the end of the simulation in the time-invariant models was calculated to assess the overall spectrum. The frequency of interest (FOI) was set to 1–9 Hz (a trade-off of 3–9 Hz in Masse *et al.* [18] and 1.5–8 Hz in Masse *et al.* [162]), the dominant frequency (DF)

was defined as the frequency with the highest peak in the power spectrum [18, 56, 163], the median frequency (MF) was defined as the frequency that cut the spectrum into two regions with equal total power, and the spectral width (SpW) was defined as the band centered at the MF that covered 67% of the power in the FOI [163]. The upper-right image in Figure 5.4 shows the locations of the DF, MF (black dotted line), and SpW (the span between the two red lines). These three parameters could describe the metrics of the VF dynamics well [163].

A time–frequency analysis was performed to check the temporal frequency variation during VF in the time-variant model. A short-time FFT was performed with a Gaussian window of 1024 points (3.072 s) shifting stepwise ($\Delta t = 192$ ms) throughout the VF episode [164]. The DF, MF, and SpW values defined above were also determined for each short-time spectrum obtained, and hereinafter are designated as ST-DF, ST-MF, and ST-SpW, respectively. The time–frequency distribution figure was then constructed by plotting the three parameters on the ordinate versus time on the abscissa.

An autocorrelation function for individual VF episodes was generated to evaluate its periodicity, and the r -value of the first peak after zero (FPAZ, dimensionless) was used for quantitative comparison [165]. All the objects of our analyses were traces of Lead II ECG.

5.3 Results of induced VF in different models

5.3.1 Effects of APDR in the time-invariant models

Panel A in Figure 5.3 shows the VF organization reproduced using a model with a steep APDR (Model 2). The continuous snapshots of the three-dimensional wave-front display intuitively demonstrate this turbulence, in which wave fronts continually emerged, bifurcated, fused, and faded, resulting in a mottled epicardial activation map. The densely scattered dark-blue pixels in the activation map indicate a high incidence of wavebreaks where an abrupt dispersion of refractoriness [164] occurred. Furthermore, a random-like spatiotemporal pattern is highlighted by the

disorganized ECG trace in Figure 5.3.

In the contrast, the tachyarrhythmia in the model with a shallow APDR (Model 4) showed a significantly higher degree of regularity and periodicity, and is technically regarded as a pleomorphic VT. The snapshots of the wave fronts in Panel B show an example of the VT. The wave fronts originated from the lateral endocardium of LV near the base, and gradually expanded into the vicinity of, and later swept over, the entire cardiac volume. This organized activity might be also manifested by the uniformly distributed activation time. The ECG trace cycle length was stable, around 260 ms, each spike was almost identical, and their amplitude was much larger than that of the ECG in Panel A.

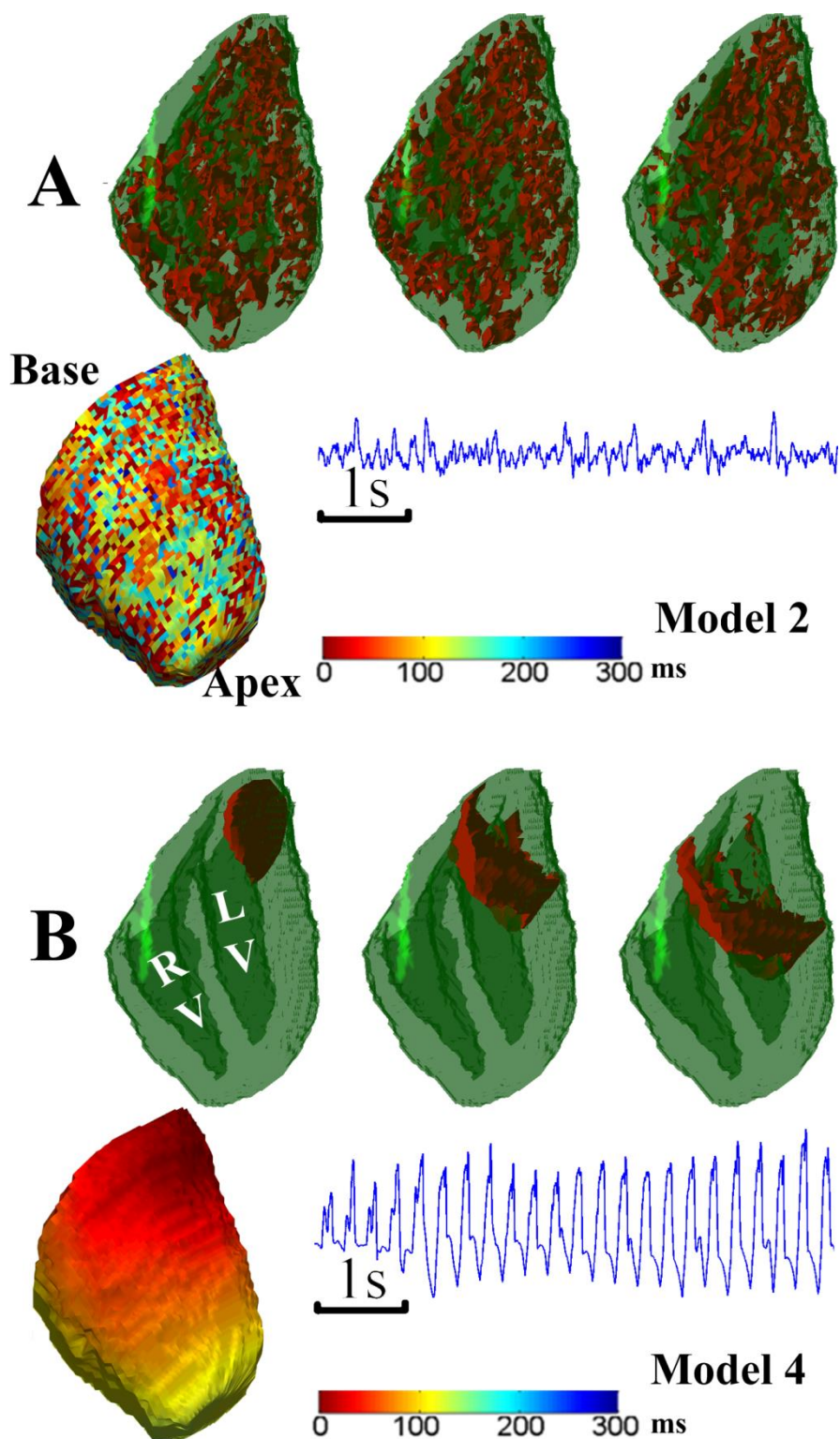


Figure 5.3 Illustrations of VF dynamics in models with different APDR (atria are not shown). (A): VF induced in a model with a steep APDR (Model 2). (B): VF induced in a model with a shallow APDR (Model 4). The upper three snapshots are consecutive shots taken 30 ms apart showing the underlying propagation (wave fronts are shown in red, and the shell of the heart is shown in semi-transparent green). The activation map shows the moment of local excitation time. Both the wave-front demonstration and the activation map are taken from a left anterior oblique (LAO) view. The ECG trace shows a 6s segment starting from the eighteenth second of the simulation. Key: RV = right ventricle, LV = left ventricle.

5.3.2 Effect of CVR in the time-invariant models

Under a steep APDR environment, the VF ECG of models with different CVR were almost the same at first glimpse, but the temporal regularity of the VF in models with decreased CVR (Model 1) was lower than that of the VF in models with normal CVR (Model 2), as evidenced by a comparison between their spectra and the autocorrelations in Figure 5.4. The spectrum of Model 1 contained multiple frequency peaks over the entire FOI domain, resulting in a broad value of SpW = 4.25 Hz, and a notable deviation of the dominant frequency (2.50 Hz) from the median frequency (4.63 Hz). The VF ECG of Model 2 was more organized in the way that the DF value coincided with the MF value (both were 5.38 Hz), and the value of the SpW decreased markedly (2.13 Hz) on comparing it with the value of SpW for Model 1.

However, under a shallow APDR environment, the influence of CVR on VF organization was opposite to that of the steep APDR situation. The VF induced in Model 3 (with decreased excitability) showed a slightly more compact spectrum than the VF in Model 4, indicating an increased degree of regularity (see Figure 5.4 Spectrum column, Models 3 and 4).

The autocorrelation plot shown in Figure 5.4 summarizes the degree of periodicity of the VF induced in models with different restitution properties, whose FPAZ values were 0.12, 0.42, 0.95, and 0.80 for Models 1, 2, 3 and 4, respectively. Note that the FPAZ value of the VF induced in models with a steep APDR (Models 1 and 2) was much lower than that in models with a shallow APDR (Models 3 and 4). Models with a normal CVR did not always show higher FPAZ values.

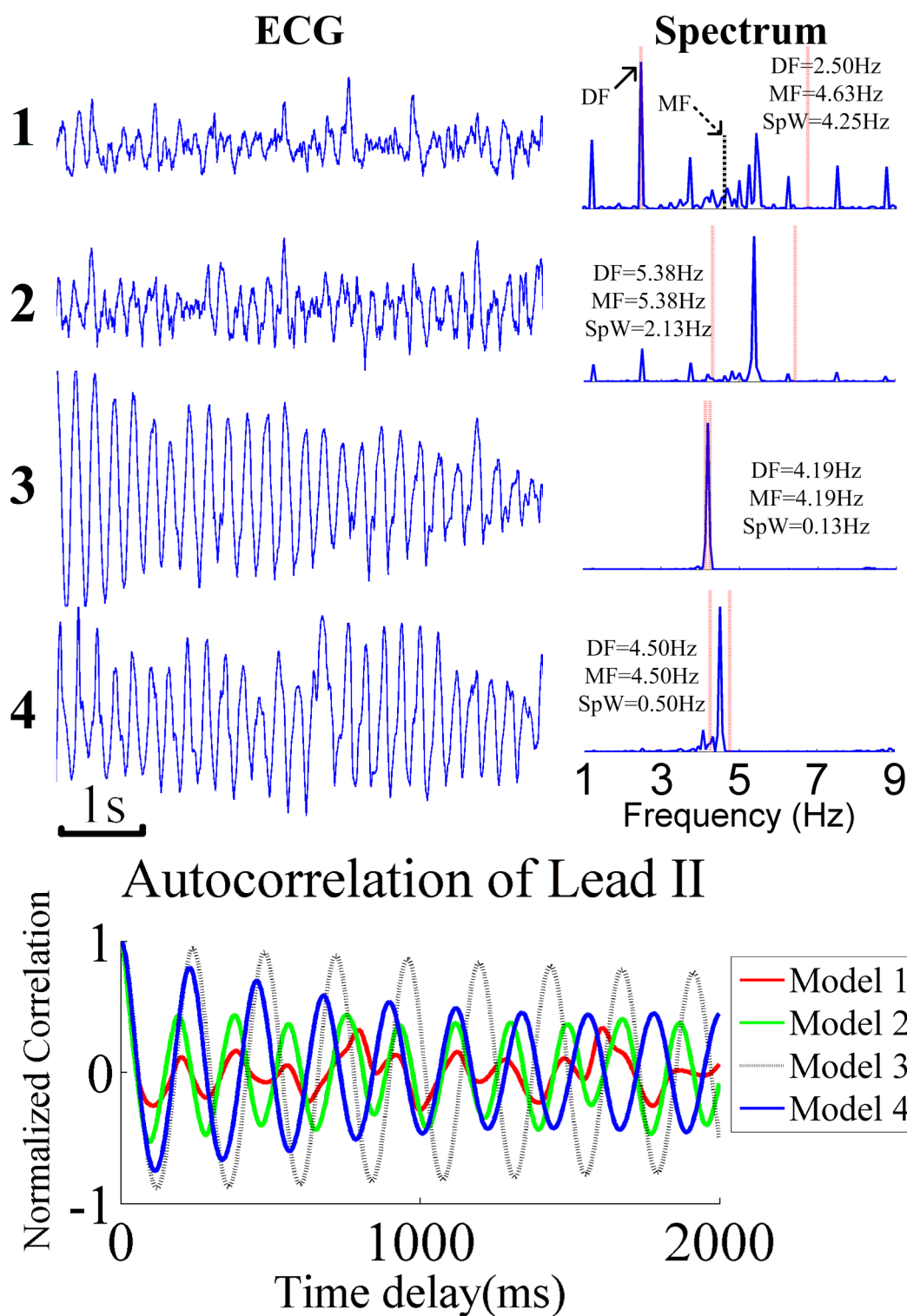


Figure 5.4 ECG characteristics of VF induced in the homogeneous models (Models 1 to 4). Upper-left side = VF-ECG episodes of 5 s, the digits on the left side denote the number of used model. Upper-right side = the corresponding ECG spectra. The dominant frequency (DF) denotes the frequency component with the highest amplitude, the median frequency (MF) is denoted by the black dashed line, and the boundaries of the spectral width (SpW) are denoted by the red dotted lines. Lower panel = autocorrelation of the ECG of the VF induced in the four models. See text for details.

5.3.3 Effect of heterogeneity in the time-invariant models

There was a relatively stable spiral activation movement in the right ventricular epicardium of Model 5, where the APDR was shallow during VF, as shown in the upper panel of Figure 5.5. The spiral wave rotated clockwise around the core (the black asterisk), which was located in the RV near to the boundary of the LV and RV, apart from at the base, for about 50% of the apicobasal dimensions. A single rotation took approximately 240 ms. The wave fronts emitted by this reentrant source managed to propagate coherently through the RV epicardium, but broke up because of intermittent fibrillatory conduction blocks in the LV (as evidenced by the complex distribution of the activation time) where APDR was steep. Its spectrum was characterized by a single peak (4.25 Hz) and a narrow SpW (0.38 Hz).

The VF of Model 6 showed considerable enantiomorphy with the VF discussed above, which is consistent with the restitution distribution. The region where the APDR was shallow also allowed regular propagation, featured by a steady breakthrough (denoted by the black dot in the lower-left image of Figure 5.5) sending out centrifugal depolarization waves. Its cycle length was about 230 ms. Simultaneously, a continuous formation of wavebreaks occurred on the other side of the heart where the APDR was steep. The spectral distribution was more concentrated compared with the VF of Model 5 (SpW = 0.13 Hz vs. 0.38 Hz).

Virtual ablations were performed to check whether the VF in Models 5 and 6 was indeed driven by the electrical activity in the shallow APDR regions (RV in Model 5 and LV in Model 6). The removal of mother rotors in the shallow APDR regions did not eliminate the VF. We found that decreasing the mass of ventricles with a steep APDR was a more effective way to eliminate the VF than reducing ventricular tissue with a shallow APDR. For Model 5, the minimum mass with a steep APDR required to sustain VF was approximately 4% of the original ventricular tissue, while the portion for a shallow APDR required to sustain VF was nearly 48%.

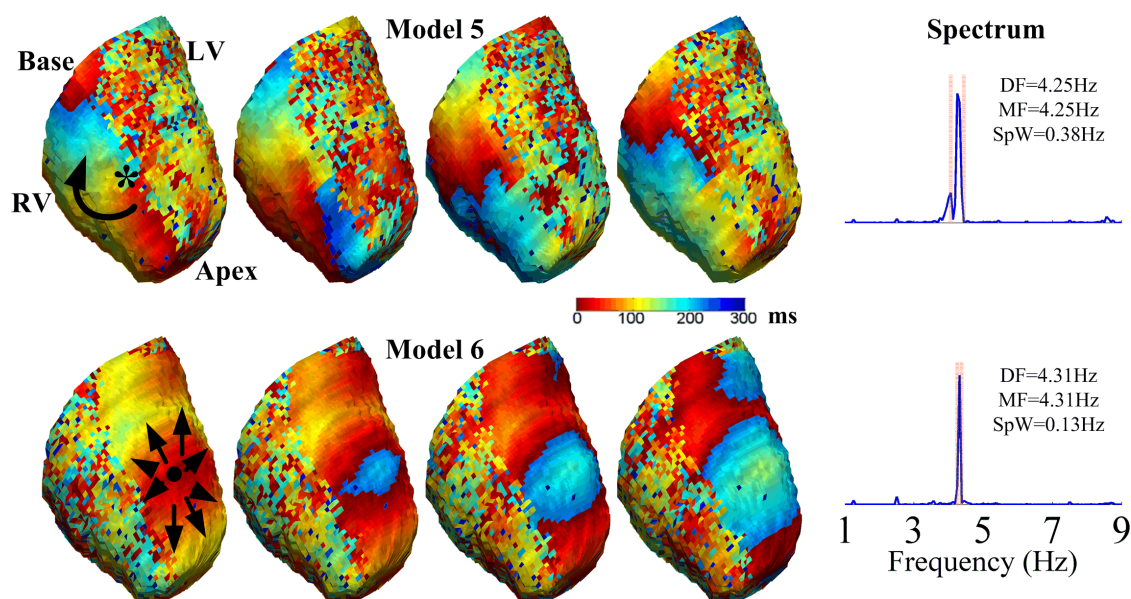


Figure 5.5 The behavior of VF induced in the heterogeneous models (Models 5 and 6). The interval between adjacent activation maps was 60 and 30 ms in the upper VF (Model 5) and lower VF (Model 6) groups, respectively. The spiral wave rotated along the direction indicated by the black arrow around the core marked by the black asterisk. The Spectrum column shows the spectra of both VF. The abbreviations used are the same as defined in Figure 5.4. Key: RV = right ventricle, LV = left ventricle.

5.3.4 Evolution of VF in the time-variant model

Figure 5.6 shows the evolution of VF in the time-variant model. The first stage (denoted by the black line) was the same as the VF induced in Model 2. The VF complexity (i.e., the characteristics of the ECG and activation map) in the time-variant model was reemphasized by its intensive temporal frequency variation. The ST-DF and ST-MF of the first stage fluctuated frequently within a wide band of 2.3–5.9 Hz. The ST-SpW changed widely over a broad range from about 0.98 to 5.9 Hz. This stage matches the description of Type 1 VF [75], or multiple-wavelet VF.

After the APDR flattened (the second stage indicated by the red arrow), the degree of regularity abruptly increased, manifested by the overtly compact spectral distribution, the neat and stable ECG spikes with occasionally varying amplitudes, and the organized activation map, although scattered wavebreaks were present. The second stage reproduced the VT well.

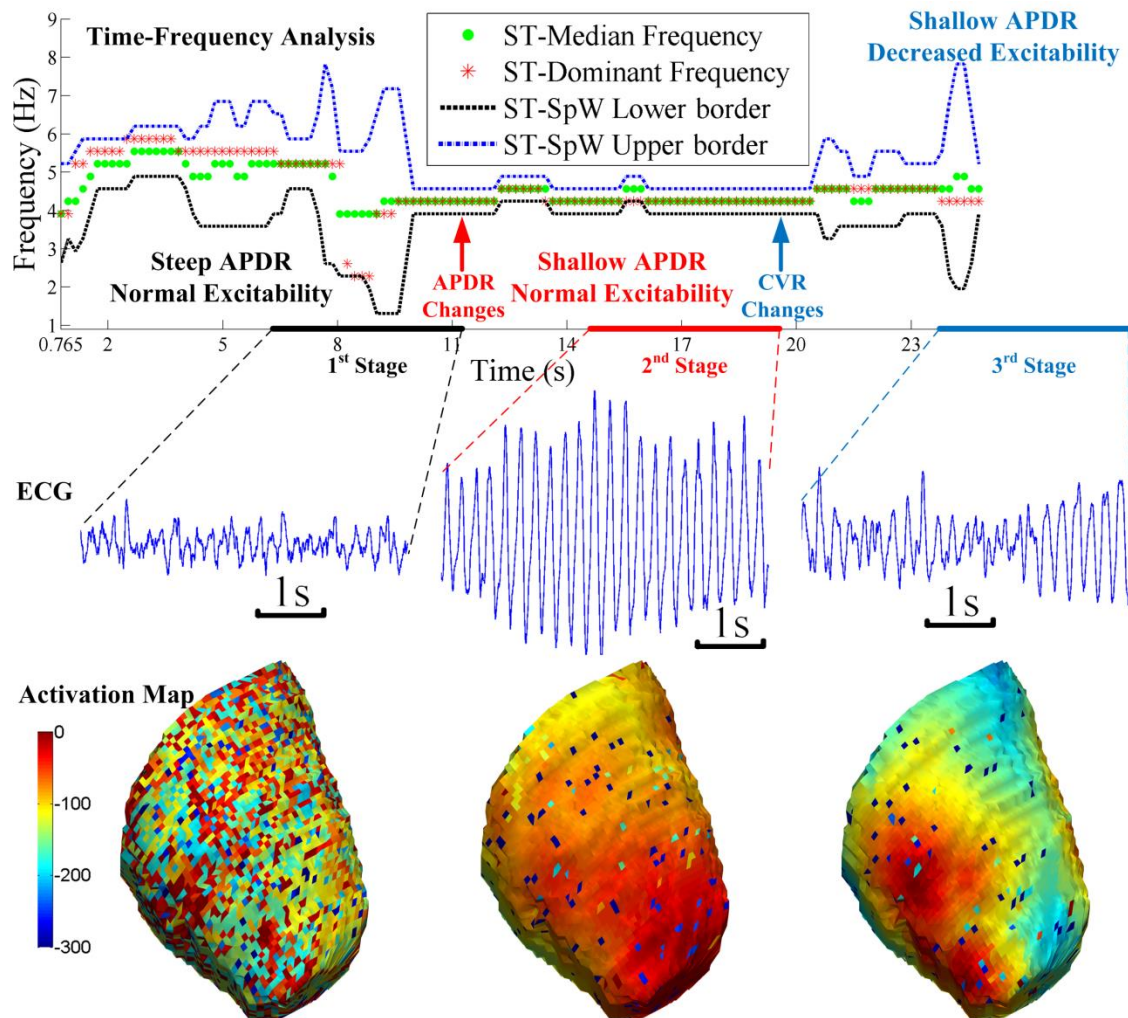


Figure 5.6 The simulation of restitution changes. The upper plot shows a time–frequency analysis. The entire trace is divided into three stages separated by two vertical arrows. The restitution settings of each stage are shown. The middle panel shows the ECG traces of the last 5 s of each stage. The span of each trace is denoted by the bold line orientated along the time axis of the time–frequency analysis. The lower maps are representative activation maps of the three stages. Key: ST = short time.

Finally, after the excitability was decreased, there was a reduction in organization that cannot be regarded as a return to the initial VF pattern. This reduction was characterized by the temporally varying and changeable frequency content as well as the irregular ECG. It seems that this stage resembles Type 2 VF. Nevertheless, the activation map showed a comparable mode with the second stage, except for the lagged activation time of the distal regions (in green) from the breakthrough (red region) because of the slow conduction velocity. Thus, the model with restitution properties that varied following the sequence suggested by Wu *et al.* [75] did not reproduce the transition from VT to Type 2 VF exactly (i.e., the mother-rotor VF).

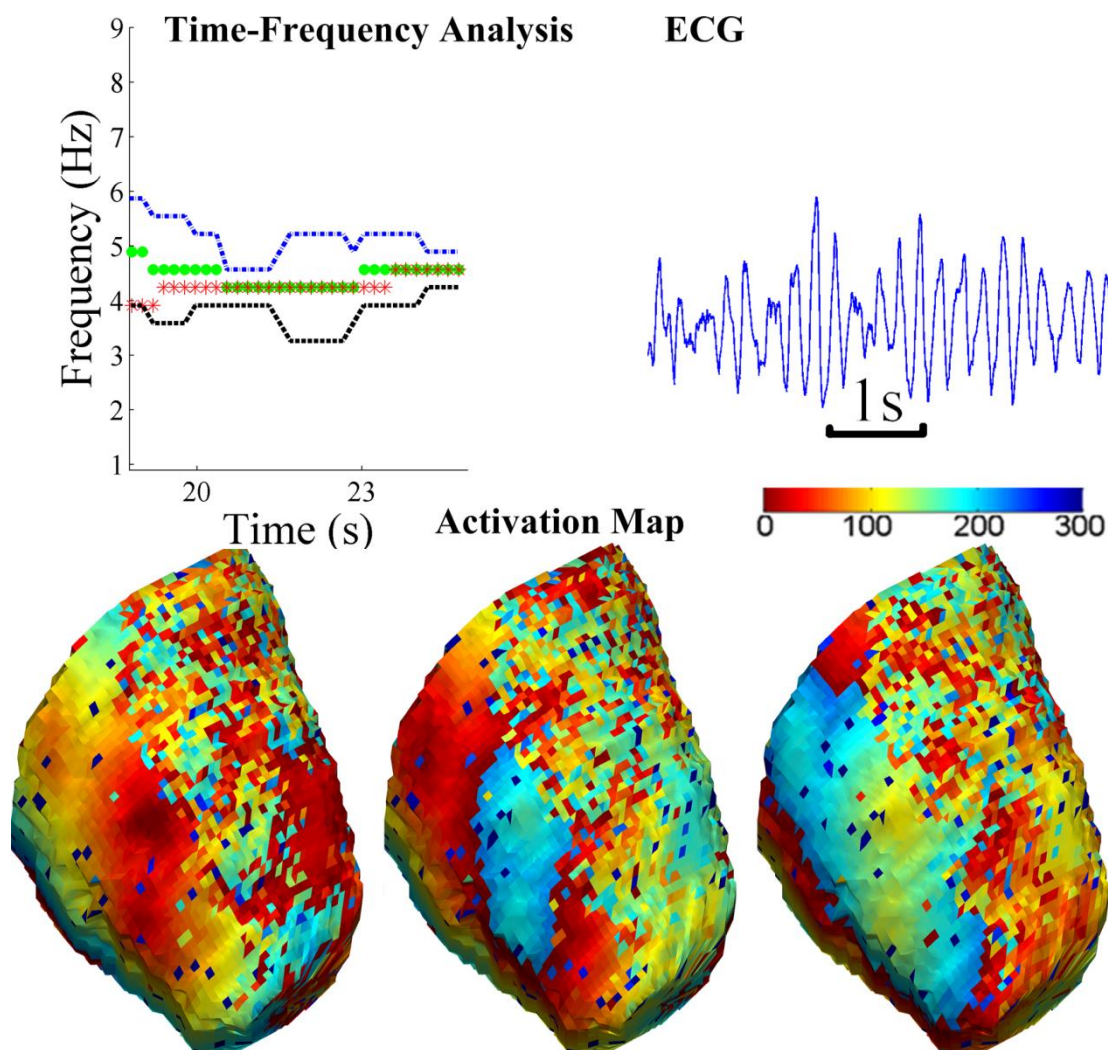


Figure 5.7 Situation of a modified “third stage” that reduces the excitability and heterogenizes the APDR. The description of the time–frequency analysis is the same as in Figure 5.6. The ECG is the last 5s episode of the resimulated “third stage”. The activation maps are taken at intervals of 60 ms.

Thus, we assumed that the suppressed excitability is an oversimplified explanation for the transition from VT to Type 2 VF, and other factors must be involved in the conversion process. We found that if the APDR was changed to a heterogeneous distribution accompanied by a decreased excitability in the third stage, then the VF transition would follow the pattern observed by Wu *et al.* [75].

Figure 5.7 shows the resimulated third stage after an abrupt transition from VT. There was an obvious decline in regularity on comparison with the VF in the second stage, evidenced by the changeable frequency content in the time–frequency analysis and the ECG. The activation maps were taken at intervals of 60 ms, and depicted VF similar to the VF induced in Model 5, reminiscent of mother-rotor VF.

5.4 Discussion

The major new findings of this chapter's work are as follows. First, to the best of our knowledge, the present study first simulated the important and well-recognized experimental study by Wu *et al.* [75] where the conversion from VT to mother-rotor VF was due to the APDR heterogenization instead of CVR flattening. Second, we clarified effects of the interplay between APDR and CVR on VF dynamics. Third, the conversion from multiple-wavelet VF to VT, and the degeneration from VT to mother-rotor VF were successfully simulated in a “non-ionic rule-based” whole-heart model.

5.4.1 Effects of restitution on VF dynamics

Our simulation data suggest that the APDR slope plays a significant role in determining the VF dynamics. In general, a steep APDR corresponds to highly disorganized VF dynamics, and a shallow APDR corresponds to regular VF dynamics.

Idiopathic VF is an uncommon disease of an unknown etiology that occurs in the absence of perceptible organic heart disease or identifiable channelopathy [166], or simply stated, “a healthy heart”. It is safe to assume that this type of heart has a shallow APDR and a normal excitability. The tachyarrhythmia induced in the model with this type of restitution (Model 4, Figure 5.3B) reproduces the idiopathic VF [167] well. Meanwhile, it is known that structural heart diseases (SHD), such as the old myocardial infarction and hypertrophic cardiomyopathy, may significantly steepen the APDR slope [168]. Simulations show that the VF induced in the models with a steep APDR (Models 1 and 2) also reproduce the multiple-wavelet VF that commonly occurs in patients with SHD, e.g., the DF of the VF induced in Model 2 was 5.38 Hz, slightly exceeding the clinical DF reported by Nash *et al.* [56] and Masse *et al.* [162]. Recently, a clinical study by Latcu *et al.* [169] has shown that the average DF of “fast VF” ($DF > 5$ Hz) and “slow VF” ($DF < 5$ Hz) was 5.84 Hz and 4.66 Hz, respectively, which are slightly above the DF values of the VF induced in Models 2 (5.38 Hz) and 4 (4.50 Hz), implying, to a certain extent, that our simulation may explain the VF

occurring in these patients. The different APDR configurations may contribute to the different behaviors between the SHD correlated VF and the idiopathic VF.

The effect of CVR modulating VF dynamics lies with the APDR. When the APDR slope is steep, CVR can markedly influence the VF organization. However, under other APDR settings, the impact of CVR is not so prominent.

The autocorrelation plot in Figure 5.4 shows the effect of restitution well. The autocorrelations of the steep APDR are lower than those of the shallow APDR; however, the autocorrelations of a decreased CVR are not always lower than those of a normal CVR, depending on the related APDR. Thus, the synergy between the APDR and CVR determines the VF dynamics, with the APDR taking the leading role.

Apart from the slope of the APDR, the heterogeneity of the APDR may also influence the VF behavior. This confirms the clinical findings of Bueno-Orovio *et al.* [170]. In the heterogeneous models, the electrical activity was organized in the regions with a shallow APDR and became unstable and broke up in the regions with a steep APDR. The DF values of the VF induced in the heterogeneous models were similar to those of clinical VF obtained during ischemia (3.60 ± 0.04 Hz) [162], which induces heterogeneity because cardiac tissue in different areas has a different tolerance to acute ischemia.

Although it seems that the VF induced in the heterogeneous models (Models 5 and 6) is driven by a breakthrough or spiral wave located in the shallow APDR region, virtual ablation reveals that this could be a false impression. According to the mother-rotor hypothesis, clearing the mother rotor should be a sufficient condition to cease the VF [94], in contrast with our simulations. However, although mother-rotor VF is well observed and documented [95], evidence of terminating VF via ablation is rare, and thus, the causality between the ablation of mother rotor and VF defibrillation remains to be established [171]. Hence, failing to stop VF with ablation does not necessarily mean that the simulated mother-rotor VF is false, and it is still possible that heterogeneity of the APDR is responsible for the mother-rotor VF. Virtual ablation also suggests that decreasing the amount of tissue with a steep APDR outweighs ablating the shallow APDR regions. Since it is not possible clinically to

locate precisely a steep APDR region, admission of a drug that flattens the global APDR slope would be a practical way to prevent or convert VF [172].

5.4.2 Effects of restitution changes and heterogeneity on VF changes

The restitution changes in the time-variant model followed the sequence reported by Wu *et al.* [75]. However, only the former two stages reproduced the expected VF well, showing a comparable time course of DF with clinical observation [173]. Although the ECG of the third stage was more irregular than the ECG of the second stage, it did not faithfully reproduce the characteristics of Type 2 VF as predicted by Wu *et al.* [75]. However, if the restitution changes, that occurred in the third stage, were composed of a decreasing excitability and a heterogenizing APDR, the VT could be converted into Type 2 VF (mother-rotor VF), as shown in Figure 5.7. This implies that a decreased CV might only partly contribute to the VF conversion, while the heterogeneity of the APDR may be one of the true causes of the transition from VT to Type 2 VF.

Consequently, our simulation results suggest that Type 1 VF indeed arises from a steep APDR and a normal excitability. The flattening of the APDR slope can convert Type 1 VF into VT, and Type 2 VF is most likely from the heterogeneity of the APDR instead of decreased excitability, or at least the decreased excitability is not the major reason for the conversion from VT to Type 2 VF. Although Wu *et al.* [75] found that the heterogeneity of the APDR among four recording sites was insignificant after D600 infusion, the heterogeneity might be masked, because four recording sites may not have fully reflected the overall heterogeneity of the APDR. It is likely that the decreased excitability played an auxiliary role to the heterogeneity and other unknown causes in abruptly converting VT into Type 2 VF. This suggested modification to the deduction of Wu *et al.* [75] needs further validation. It is worthwhile to note that these factors are in line with the cardiac attributes determining the wavebreak suggested by Weiss *et al.* [64].

5.4.3 The feasibility of using a rule-based model for the current study

As far as VF is concerned, publications showed that the behaviors of spiral waves and reentry circuits were simulated with both reaction–diffusion models (ionic rule-based models) and cellular automaton models (non-ionic rule-based models, or simply called rule-based models) [174-176]. Several studies could even construct a cellular automaton model from “reaction–diffusion” rules to reproduce simulations of “reaction–diffusion” models [177-180]. So we consider that these two types of heart model should be complementary to each other. On the other hand, in the “rule-based” model, the clinically measured restitution can be faithfully and quantitatively translated into the simulation rules that govern the cellular dynamics, but it is difficult to do so in the “reaction–diffusion” model. In order to directly examine the relationship between cardiac restitution and VF dynamics, it is more suitable to use a “rule-based” model (which is the Wei–Harumi whole-heart model) for the current study.

5.5 Summary and conclusions

In this chapter, different types of VF in models with different APDR and CVR setups were simulated using the Wei–Harumi model. Our simulation results suggest that the mechanism of VF has a tight relationship with the cardiac restitution properties. It is likely that the conventional mechanisms of VF can all be explained by the restitution mechanism. In addition, our work supports the hypothesis that the synergy between the APDR (both its slope and heterogeneity) and CVR contributes to transitions between multiple-wavelet and mother-rotor mechanisms in the VF. We believe that the results from our simulation study based on a whole-heart model may be significant in understanding the mechanism of VF, and complement “reaction–diffusion” model-based and experimental studies.

Chapter 6 Effects of Action Potential Duration Gradients on the Genesis of the Concordant T wave

6.1 Background

The T wave is a valuable contributor to cardiac diagnosis. It is believed to result from the spatial potential differences stemming from repolarization (downstroke) of the action potential (AP) in individual cells throughout the ventricular walls [181]. Some abnormal repolarization pattern, e.g. early repolarization syndrome was suggested to be associated with idiopathic ventricular fibrillation (VF) [182], and clinical researches have proven that patients with a history of idiopathic VF have a higher prevalence of early repolarization [183]. More recently, T-wave alternans has been considered as a promising marker in assessing the risk of ventricular arrhythmogenesis [184]. So studying T wave can provide us considerable information for investigating the mechanism of VF genesis. In this chapter, we investigated the relationship between the AP duration (APD) gradients and the normal T wave.

6.1.1 T wave and APD dispersion

Reported work suggests that T-wave peak corresponds to the earliest end of repolarization [185]. It is evident that the distribution of the APD is uneven; otherwise, the polarity of the T wave will be opposite to the QRS complex because the former reflects the downstroke of the AP and the latter represents the upstroke. In fact, an inverse relationship between the activation time and APD was found in human trials [186, 187], and confirmed by simulations [188]. In other words, the cell that is excited first is the last one to repolarize. Many studies have shown that there are different types of electrophysiological heterogeneities (APD dispersion) existing in the ventricles, such as the apicobasal gradient [189], transmural gradient [190] and left–right ventricular APD heterogeneity [100, 158].

6.1.2 Researches on mechanisms of concordant T wave

Unlike the P wave and the QRS complex [191], the source and derivation of the T wave are still controversial [192-194]. The debate focuses mainly on the role of APD gradients on the formation of the T wave. Originally, it was believed that the T wave was caused by the gradient of repolarization in the apicobasal dimension [195]. Nowadays, the transmural repolarization gradient is becoming increasingly accepted as the true reason for the upright T wave [40, 196, 197]. Through simulations, Xue *et al.* suggested that the role of the apicobasal gradient was superior to the transmural gradient in the genesis of the positive T wave [198]. In stark contrast, Okada *et al.* used simulations to suggest that apicobasal APD dispersion makes merely an auxiliary contribution to the attainment of the physiological T-wave morphology compared with the transmural APD gradient [199], and the validity of this suggestion was supported by a reasonable agreement between the simulated and measured ECG in a limited number of clinical cases [200].

In 2007, Weiss *et al.* reported that they had studied the effects of three APD gradients on the T-wave polarity and found that interventricular APD changes were necessary to reproduce the positive T wave [201]. Four years later, they investigated the influence of slowly delayed rectifier current I_{Ks} heterogeneities in different cardiac dimensions on the T-wave shape in an anatomically detailed human ventricular model within a realistic torso. They concluded that the interventricular APD dispersion may be undesirable in reproducing the measured human ECG [202]. Nevertheless, Opthof *et al.* [193] suggested that although the interventricular dispersion only provides a trivial contribution to the dispersion in activation time, the portion of the contribution that it provides to the dispersion in the recovery outweighs the sum of the other dispersions. Each conclusion drawn by these studies seems plausible, and there must be a correct explanation.

According to Opthof *et al.* [193] and Arini *et al.* [203], the anteroposterior heterogeneity is also a contributor to ventricular repolarization dispersion (VRD). In this study, we investigated the effect of APD gradients in four dimensions (transmural,

interventricular, apicobasal and anteroposterior) on T waves in a whole-heart model, with a particular focus on how the anteroposterior APD gradient affects the T-wave amplitudes and its role in simulating T-wave amplitudes that are similar to the clinical findings [204].

6.2 Electrophysiological settings

The Wei–Harumi whole-heart model was used as the study platform. Please refer to Chapter 2, session 2.3.6 for detailed information about electrophysiological settings and surface ECG calculation method. Any special settings or modifications are described below.

6.2.1 The APD gradient in the transmural dimension

In the transmural dimension, the ventricles were layered from the epicardium to the endocardium. The thickness of each layer was 1.5 mm. The left image in Figure 6.1A shows the layered structure of a ventricular cross section. The transmural APD dispersion was realized by assigning different APD to different layers. A typical AP morphology is shown in the right image of Figure 6.1A.

According to clinical measurements by Taggart *et al.* [190], the transmural APD increased from the epicardium to the endocardium with a gradient of approximately 1 ms/mm. In this study, we assumed that the transmural APD increased linearly from the epicardium to the endocardium with a gradient of 2 ms/layer, namely 1.33 ms/mm. The image on the right side of Figure 6.1A displays the morphologies of the epicardial and endocardial action potentials.

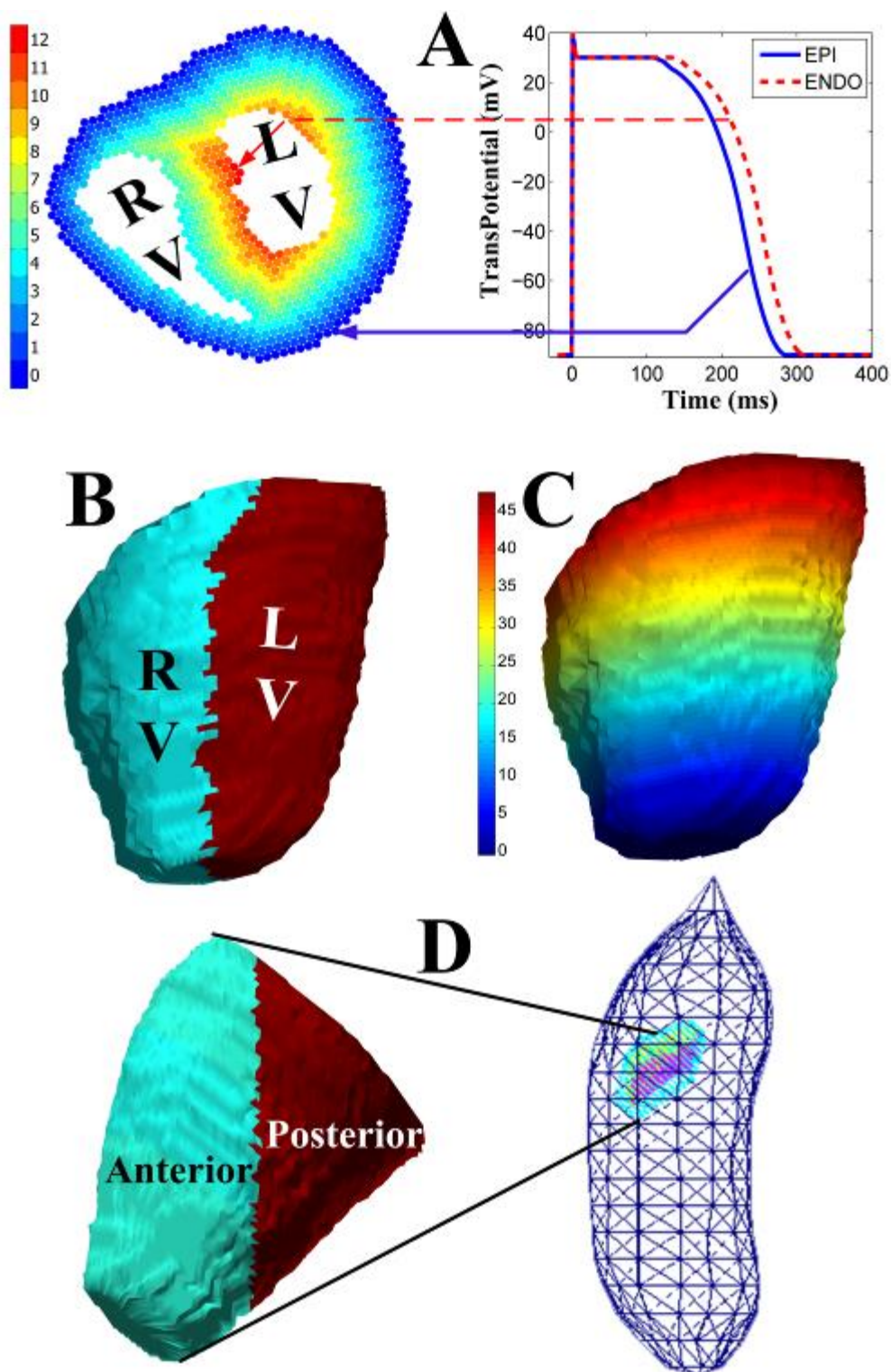


Figure 6.1 Schematics of gradients in different dimensions (atria are not shown). (A): a cross section in the left image shows the transmural APD gradient, the right image shows two representative AP morphologies of the epicardial and endocardial cell. The red-dashed waveform is the action potential of an endocardial cell, and the blue waveform is the action potential of an epicardial cell with a shorter plateau phase. The corresponding arrows indicate their locations in the heart. (B): division of the left and right ventricles. (C): the apicobasal gradient. (D): division of the anterior and posterior ventricles and the position of the heart inside a torso. Key: RV = right ventricle, LV = left ventricle.

6.2.2 The APD gradients in other dimensions

The heart was divided into the right and left ventricle (RV and LV, respectively) along the septum, as shown in Figure 6.1B (taken from a left anterior oblique (LAO) view). For simplicity, the interventricular dispersion was represented by a specific APD difference between the two ventricles.

The ventricles were sliced along the apicobasal direction, as shown in Figure 6.1C (again from an LAO view). The apicobasal APD increment was proportional to the sequence number of the corresponding slice. The thickness of each layer was also 1.5 mm.

The right image of Figure 6.1D displays the location of the heart inside a torso from a lateral view. The left image is a close-up of the ventricles, divided into anterior and posterior parts by a frontal plane. Like the interventricular gradient, the anteroposterior dispersion was represented by a specific APD difference between the anterior and posterior areas.

6.2.3 The APD of different model cells

The APD of one model cell was determined by (6.1):

$$\begin{aligned} \text{APD} = & \text{APD}_{\text{base}} + \text{LayerNum}_{\text{T}} \cdot \text{Gradient}_{\text{T}} + \text{LayerNum}_{\text{AB}} \cdot \text{Gradient}_{\text{AB}} \\ & + \text{IV} \cdot \text{Gradient}_{\text{IV}} + \text{AP} \cdot \text{Gradient}_{\text{AP}} \end{aligned} \quad (6.1)$$

where APD_{base} is the predefined baseline APD (a constant in this study), $\text{LayerNum}_{\text{T}}$ is the sequence number of the model cell in the transmural dimension (see Figure 6.1A for the transmural sequence), $\text{LayerNum}_{\text{AB}}$ is the sequence number of the model cell in the apicobasal dimension (see Figure 6.1C for the apicobasal sequence), IV represents the ventricle that the model cell belongs to ($\text{IV} = 1$ for the LV, and $\text{IV} = 0$ for the RV), and AP is the indicator of the location in the anteroposterior direction ($\text{AP} = 1$ if the model cell is in the posterior area, and $\text{AP} = 0$ if the model cell is in the anterior area). $\text{Gradient}_{\text{T}}$, $\text{Gradient}_{\text{AB}}$, $\text{Gradient}_{\text{IV}}$ and $\text{Gradient}_{\text{AP}}$ are the transmural, apicobasal, interventricular and anteroposterior gradients, respectively.

Because homogeneous APD lengthening in the entire ventricular volume only

results in elongation of the ST segment rather than T-wave variations [197], the absolute APD value is not as important as the APD dispersion in the genesis of the positive T wave. In other words, the baseline APD can be an arbitrary value. In this study, we set the APD_{base} to be 260 ms.

6.2.4 Models with different gradients

Table 6.1 shows the gradient settings for five different models. For convenience, the unit used for the transmural and apicobasal gradients was ms/layer, which can be converted into ms/mm by dividing by 1.5; the unit used for interventricular and anteroposterior dispersions was millisecond. Model 1 was a model with a homogeneous APD. Model 2 had a transmural gradient of 2 ms/layer. Based on Model 2, we constructed three models having gradients in the other three dimensions: Model 3 had an apicobasal gradient ranging from 0.05 to 0.3 ms/layer; Model 4 had an interventricular gradient ranging from -30 to -5 ms; and Model 5 had an anteroposterior gradient ranging from 5 to 30 ms.

Table 6.1 The gradient settings of models

<i>Model</i>	Gradient _T [*]	Gradient _{AB} [*]	Gradient _{IV} ^{**}	Gradient _{AP} ^{**}
1	0	0	0	0
2	2	0	0	0
3	2	0.05 – 0.30	0	0
4	2	0	$-30 - -5$	0
5	2	0	0	5 – 30

a. Unit is ms/layer

b. Unit is ms

6.3 Analysis of the simulation results

6.3.1 Simulation results of Models 1 and 2

The blue trace in Figure 6.2 displays the simulated ECG of Model 1, namely the model with the homogeneous APD. It is obvious that the T-wave direction is opposite to the direction of the prominent part of the QRS complex in the same lead. This result agrees with the prediction of Harumi *et al.* [181]. Apparently, these T waves are quite different from those shown by the black traces in Figure 6.2, which have amplitudes that agree with the clinical reports [204].

The red trace shows the ECG generated by the simulation of Model 2. We can see that when the transmural gradient was added to the ventricles, the derived T-wave amplitudes were closer to the clinical values in many leads, except for the slightly expanded deviation in the lead aVL. However, apart from the lead V2, the T-wave amplitudes of Model 2 were still considerably different from the clinical values.

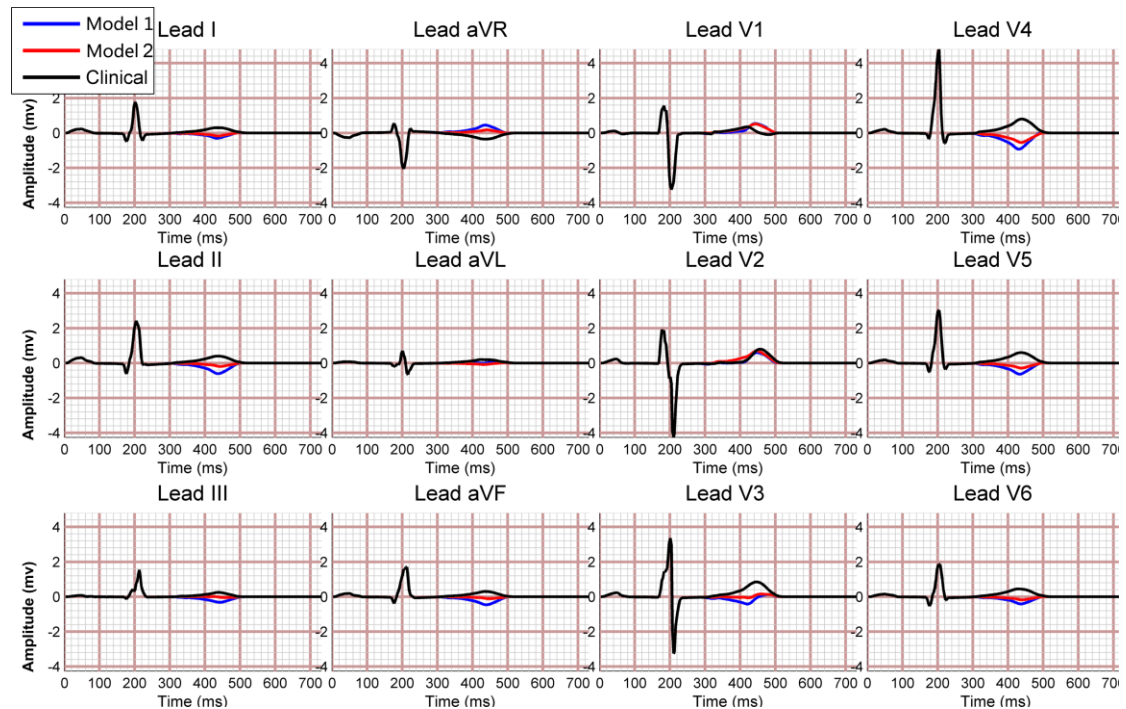


Figure 6.2 The simulated ECG using Models 1 and 2 and the clinical ECG.

6.3.2 Simulation results of Model 3

As displayed in Figure 6.3, with the gradually increased apicobasal gradient, the simulated T-waves show quite different change trends in different leads:

1. There is hardly noticeable movement among T-wave waveforms in leads I, V1 and V6.
2. The T-wave amplitudes ascend in leads II, III, aVF and V2 to V5, and the T-wave polarity of leads II, aVF and V4 is gradually turned from negative to positive.
3. Although certain apicobasal gradients can generate T waves consistent to the clinical amplitudes in some leads, e.g. the T wave in lead III when the gradient is 0.20 ms/Layer, a total match to the clinical values in 12 leads is not observed in all simulations of Model 3.

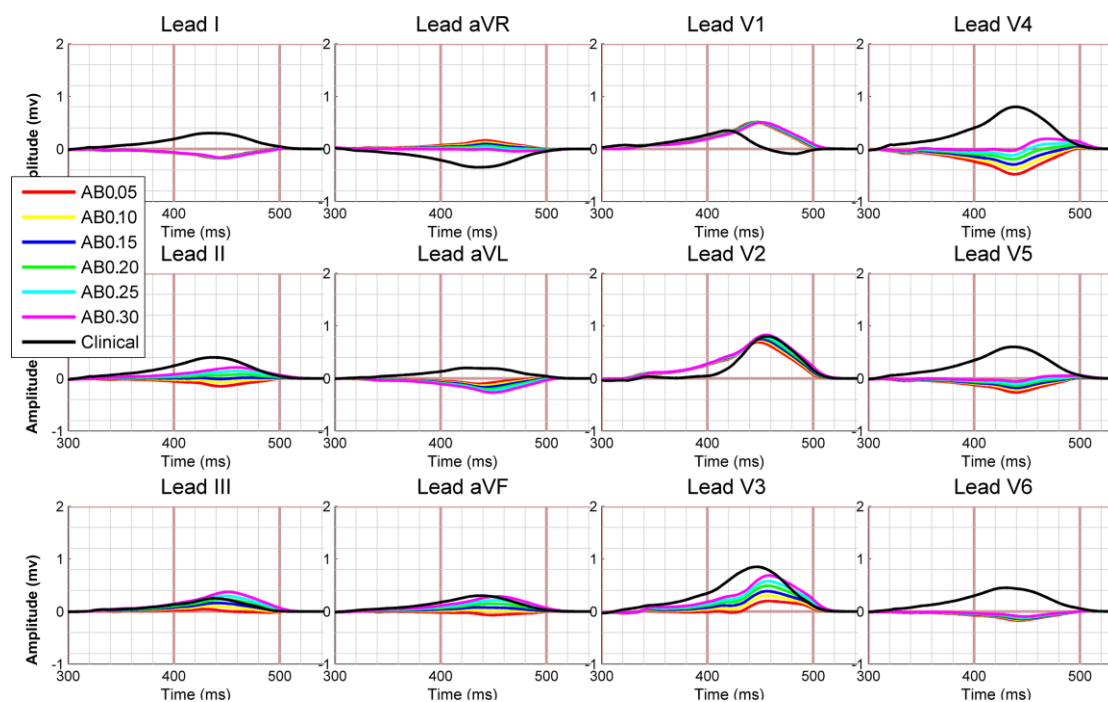


Figure 6.3 The simulated T waves using Model 3. The “AB” in the legend box means the apicobasal gradient, the number to the right indicates the value of the gradient. No close match in all leads between the simulated T wave and the clinical T wave was obtained.

6.3.3 Simulation results of Model 4

Figure 6.4 shows how the interventricular gradient influences the morphology of simulated T wave. When the absolute APD drop between two ventricles becomes larger and larger, the T waves have following changes:

1. Except the lead aVF, the other 11 leads show significant changes of T-wave amplitude: the T-wave amplitudes in leads I to aVL and leads V4 to V6 change towards the clinical values; T wave in leads V1 to V3 change away from the clinical amplitudes.
2. Like simulations done in Model 3, certain interventricular heterogeneities can produce clinical comparable T waves in several leads, e.g. when the APD of right ventricle is 15 ms longer than the APD of left ventricle, the simulated T waves match the clinical amplitudes in leads I and aVL. However, no simulation run in Model 4 can generate T waves close to the clinical amplitudes in all leads.

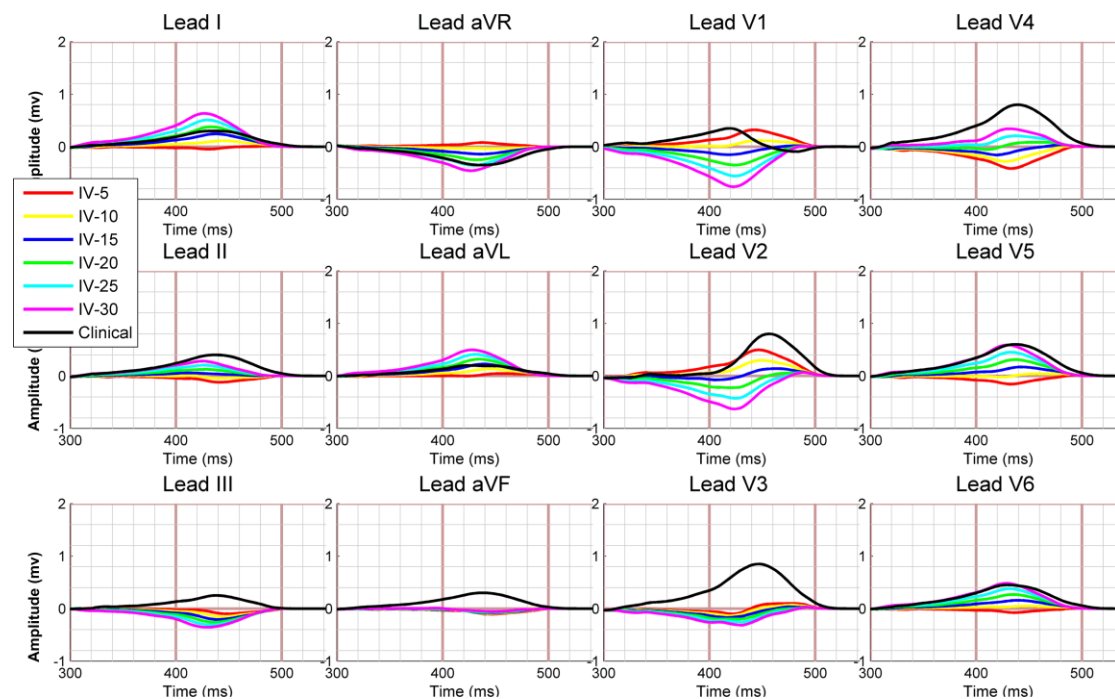


Figure 6.4 The simulated T waves using Model 4. The “IV” in the legend box represents the dispersion in the interventricular dimension, and the number to the right indicates the value of APD difference. No close match in all leads between the simulated T wave and the clinical T wave was obtained.

6.3.4 Simulation results of Model 5

Figure 6.5 shows the T-wave morphologies computed from different anteroposterior dispersion in Model 5. Again, no ideal match in all leads is obtained from this model. The ECG morphologies have similar changes as those of Model 4, nevertheless some unique features exist:

1. Fast amplitude changes are mainly in the precordial leads.
2. The manner of changes in the limb leads, including direction and speed, is similar as those of simulations using Model 3.
3. The change directions in the precordial leads are opposite to those of simulations using Model 4.

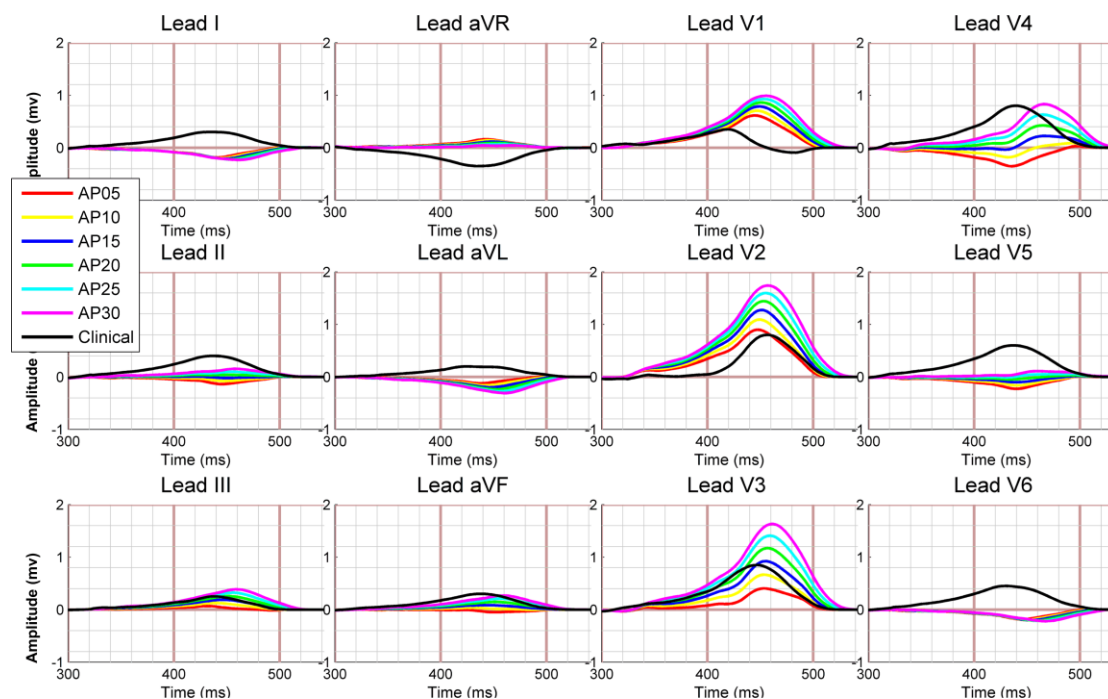


Figure 6.5 The simulated T waves using Model 5. The “AP” in the legend box means the dispersion in the anteroposterior dimension, the number to the right indicates the value of APD difference. No close match in all leads between the simulated T wave and the clinical T wave was obtained.

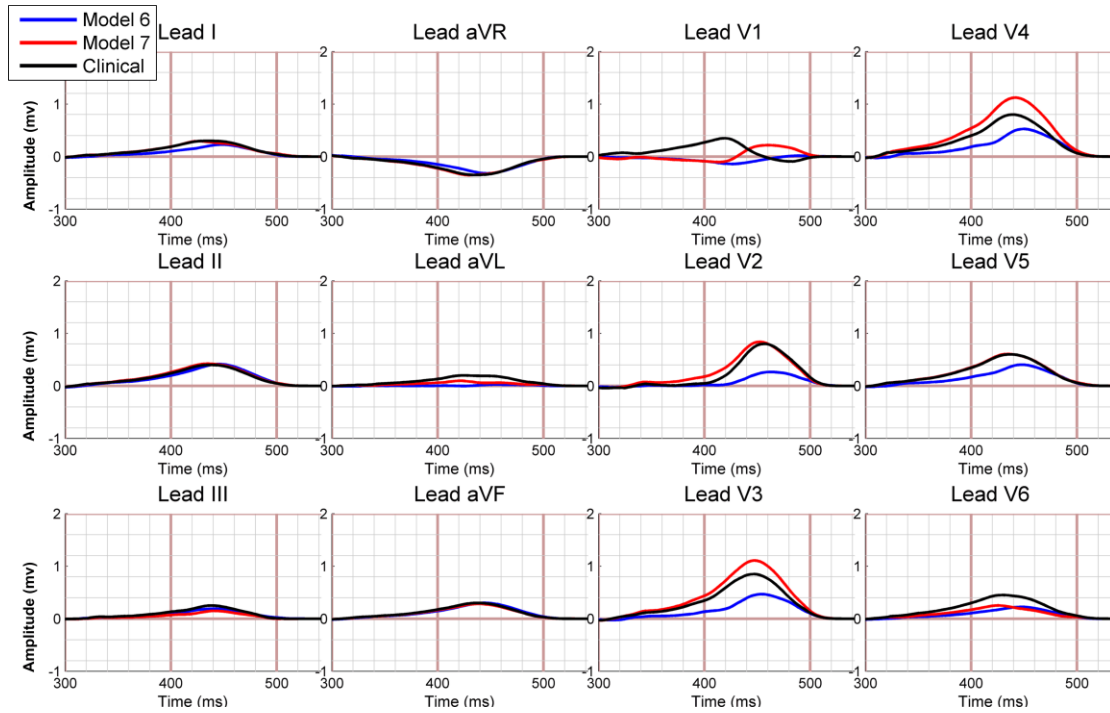


Figure 6.6 The simulated T waves using Models 6 and 7 and the clinical T wave.

6.3.5 Optimized combinations of gradient in different dimensions

Because models with a single gradient cannot generate T waves with amplitudes close to clinical values in all leads, we tried to simulate ECG in models incorporating several different gradients.

First, we assumed that there was no APD gradient in the anteroposterior dimension. By using an optimized configuration of $\text{Gradient}_T = 2 \text{ ms/layer}$, $\text{Gradient}_{AB} = 0.298 \text{ ms/layer}$ and $\text{Gradient}_{IV} = -15 \text{ ms}$ (hereinafter referred to as Model 6), we obtained T waves shown by the blue traces in Figure 6.6. These T waves did indeed show significantly improved consistency with the clinical amplitudes. In spite of this, good agreement with clinical values was only confined to the limb leads. The polarity of the T wave in the lead V1 was opposite to the clinical polarity, and the T-wave amplitudes in the leads V2 to V6 were only 32% to 67% of the corresponding clinical values (see Table 6.2).

Table 6.2 The ratios of simulated T-wave amplitudes to clinical values

<i>Model</i>	<i>I</i>	<i>II</i>	<i>III</i>	<i>aVR</i>	<i>aVL</i>	<i>aVF</i>
6	76.07%	103.35%	75.84%	91.63%	12.25%	100.17%
7	97.87%	104.85%	59.80%	100.91%	47.95%	94.30%
<i>Improvement</i>	21.80%	-1.50%	-16.04%	7.46%	35.70%	-5.57%
<i>Model</i>	<i>V1</i>	<i>V2</i>	<i>V3</i>	<i>V4</i>	<i>V5</i>	<i>V6</i>
6	-40.23%	32.99%	54.91%	65.80%	67.17%	49.87%
7	61.97%	104.65%	130.35%	140.34%	100.98%	55.96%
<i>Improvement</i>	102.2%	62.36%	14.74%	-6.14%	31.85%	6.09%

Later, we introduced the anteroposterior gradient into the model and found that when the ventricles had a setting of $\text{Gradient}_T = 2$ ms/layer, $\text{Gradient}_{AB} = 0.043$ ms/layer, $\text{Gradient}_{IV} = -22$ ms and $\text{Gradient}_{AP} = 24$ ms (hereinafter referred to as Model 7), the simulated T waves (shown by the red waveforms in Figure 6.6) had the closest similarity to the clinical amplitudes. The T waves in the limb leads matched the clinical amplitudes quite well, as evidenced by the coincidences of the red and black traces. Table 6.2 shows a comparison of the simulated T waves between Models 6 and 7. These percentages are ratios of the simulated T-wave amplitudes to their corresponding clinical values. Although neither Model 6 nor Model 7 exactly reproduced the clinical T-wave amplitudes, the latter had an improved similarity. This improvement did not happen in every lead: in leads II, III, aVF and V4, the T-wave amplitudes in Model 6 were even closer to the clinical amplitudes. However, the differences seen in these leads between the two models were relatively small, ranging from 1.5% to 16.04%. In contrast, the changes in the other leads were much more pronounced, ranging from 6.09% to 102.2% with an average of 35.28%. The T-wave polarity in the lead V1 became concordant with its preceding QRS complex. This means that the direction of every T wave simulated in Model 7 matches the clinical observations.

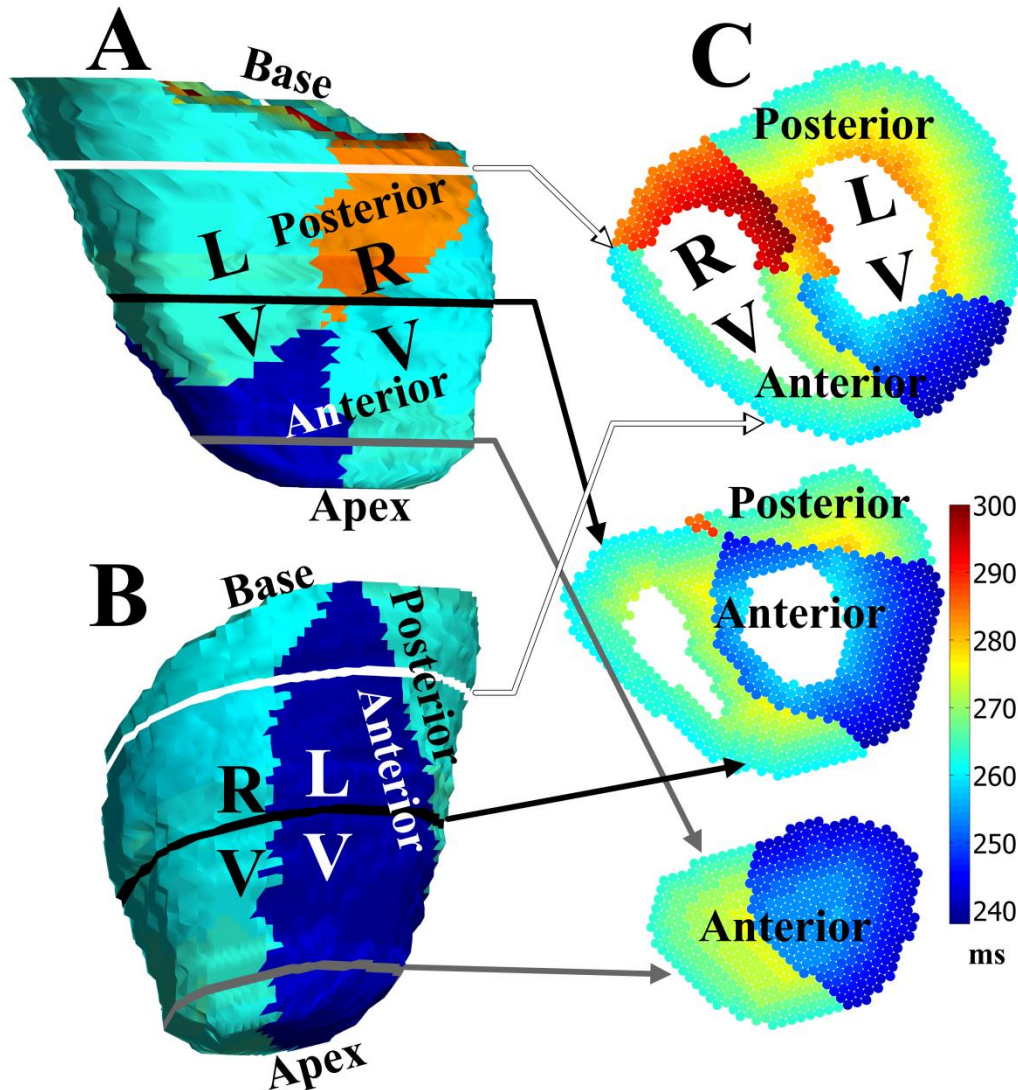


Figure 6.7 The APD distribution in Model 7. (A): the APD distribution on diaphragmatic surface from a right posterior oblique view; (B): the APD distribution on sternocostal surface, seen from an LAO view; (C): three representative cross sections whose locations are indicated by the white, black and gray lines in A and B. Key: RV = right ventricle, LV = left ventricle.

The APD distribution in Model 7 (see Figure 6.7) was very complicated, as shown by the distinct APD variations in left–right, front–back and transmural directions.

6.4 Discussion

6.4.1 The transmural gradient in the heart

The transmural APD heterogeneity was once considered to be the major cause for the T wave and QRS complex of the human ECG having the same polarity [181]. The

reliability of this viewpoint was enhanced by the discovery of M cells [192, 196]. However, although direct experimental evidence of the existence of M cells in human ventricles was found [205, 206], clinical trials [190, 207] and simulations [34] have suggested that M cells are functionally “invisible”; in other words, there is no prominent distinction between the surface and midmyocardial cells in an intact heart [194, 208, 209]. This quantitative difference is mainly caused by the electrotonic current flow of the intercellular coupling [34], which smoothens the intrinsic APD discrepancy amongst neighboring myocytes [210]. In fact, clinical measurements have proven that the transmural APD increases gradually from the epicardium to the endocardium [190].

Nevertheless, the transmural APD gradient alone cannot explain why the T wave is concordant with the QRS complex. As we know, the T wave is associated with the dispersion of repolarization [40, 194]. To generate a T wave with the same direction as the QRS complex, the epicardial cells have to repolarize earlier than the endocardial cells [181, 197]. However, recent clinical studies have shown that although the transmural APD did increase gradually from the epicardium to the endocardium, the endocardium repolarized earlier than the epicardium [34] or almost simultaneously [187]. This is because the repolarization time of an individual cell is calculated by adding its APD to its depolarization time, and the transmural APD increment from the epicardium to the endocardium is not long enough to compensate for the change in the transmural activation time. This is probably the reason why the ECG simulated by Model 2 manifested discordant T waves in most of the leads. Hence, besides the transmural gradient, there must be other APD heterogeneities contributing to the genesis of the T wave.

6.4.2 Roles of the apicobasal, interventricular and anteroposterior gradients

The apicobasal gradient is also recognized as one of the primary causes of T-wave concordance [189, 198]. However, our study demonstrated that a model with a combination of transmural and apicobasal gradients (Model 3) still did not generate T waves with clinically comparable amplitudes in all leads.

Because the difference between the clinical values and the T-wave amplitudes simulated in Model 2 varied among the 12 leads (e.g., the drop in the lead V4 was very large, but the drop in the lead V2 was relatively small), changing another single gradient (Models 3–5) could only generate T waves with amplitudes matching the clinical values in a limited number of leads. In addition, a similarity to the clinical values could never be reached in some leads, because changing the APD gradient did not always bring about desirable changes in the T-wave amplitudes. For example, in the simulations of Model 4 (Figure 6.4), when the interventricular difference was -15 ms, the simulated T waves in the leads I and aVL showed good agreement with the clinical amplitudes; if we wanted to simulate T waves with amplitudes close to the clinical amplitudes in the leads aVR and V6, we had to expand the interventricular difference to -30 ms, and this led to deviations of the simulated T waves in the leads I and aVL from the clinical amplitudes. It is obvious that changing the interventricular heterogeneity alone could not generate a T wave matching the clinical signal in the lead aVF, because there was little change in the T-wave amplitude in response to the change in APD heterogeneity. This dilemma existed in all simulations created by Models 3–5, implying that a change in a single gradient was not capable of reproducing T waves with clinical amplitudes in all leads. This is in line with the findings of Weiss *et al.* [201].

6.4.3 The necessity of including the anteroposterior gradient

From the simulations using Models 3–5, we noticed that the uneven amplitude changes provided by different gradients might be smoothed out if the changes to the gradients in various dimensions were combined. Indeed, the combination of transmural, apicobasal and interventricular gradients did generate T waves closer to the clinical observations compared with the results from Models 3–5. Adding the anteroposterior gradient into the model provided a striking improvement in the similarities to the clinical values (see Table 6.2). This is strong evidence that the anteroposterior APD dispersion is essential to forming the normal T wave. Considering this finding, we hypothesized that the anteroposterior gradient plays an

important role in the genesis of the T wave.

6.4.4 Comparing simulation results with clinical studies

A comparison between Figure 6.7 and the clinical epicardial activation recovery interval (ARI, a surrogate of APD [160]) map [211] demonstrates that, to a large extent, the APD distribution in Model 7 faithfully reproduced the clinical findings: the longest APD was at the posterior basal ventricle, and the shortest APD was at the anterior apical ventricle. The APD in the anterior RV and the posterior LV were almost the same. The endocardial and epicardial APD dispersions in Model 7 were also similar to the repolarization time dispersions found in clinical reports (8 ms vs. 14 ± 2 ms and 47 ms vs. 50 ± 9 ms, respectively) [187]. Ramanathan *et al.* [211] reported that the average ARI of the RV was 32 ms longer than that of the LV, and the apex-to-base dispersion was 30 ms. Our optimal APD configuration includes an interventricular difference of -22 ms (longer RV APD) and an apex-to-base dispersion of about 26 ms (the sum of an anteroposterior difference of 24 ms and an apicobasal gradient of 0.043 ms/layer multiplied by 46 layers). Thus, it is safe to conclude that the APD distribution of Model 7 was close to the clinical measurements. The consistency of the simulation results with the clinical data enhances the reliability of our hypothesis.

6.5 Conclusions

We hypothesized that the anteroposterior gradient is an essential consideration in accounting for the T wave being concordant with QRS complex in the human ECG. This hypothesis was supported by the computer simulations in this chapter. The setup of the APD distribution in our model simulated T waves that were very similar to the clinical findings. This study contributes to the theoretical and clinical understanding of the T-wave genesis in human surface ECG.

Chapter 7 Conclusions

7.1 Contributions of this dissertation

Ventricular Fibrillation (VF) is the most malignant arrhythmia that remains a significant cause of sudden cardiac death. Action potential duration (APD) restitution and conduction velocity (CV) restitution are considered to be two major determinants of VF formation and maintenance. Many studies carried out by computer simulations were done to investigate the relationship between cardiac restitution and ventricular fibrillation, and fruitful outcomes were gained that facilitate understanding VF mechanisms.

In this dissertation, the following contributions were made:

- a) The feasibility of studying VF in the Wei–Harumi model with diastolic-interval (DI) dependent restitution was proven. Through simulation, it is suggested that steeper APD restitution (APDR) slope is related to higher risk of VF genesis.
- b) It was demonstrated that only certain combinations of VF-induction protocols and sites could induce self-sustainable VF, but the induced VF organization was not related with VF-induction methods. It is concluded that the selection of induction methods has little influence on VF patterns, and the different VF patterns are solely the reflections of different intrinsic electrophysiological properties.
- c) Different types of VF in models with different APDR and CV restitution (CVR) setups were successfully simulated using the Wei–Harumi model. VF in models with different APDR manifested distinct behaviors, either multiple-wavelet or mother-rotor, and these behaviors were considerably affected by CVR. Our work supports the hypothesis that the synergy between the APDR (both its slope and heterogeneity) and CVR contributes to transitions between multiple-wavelet and mother-rotor mechanisms in the VF. It is likely that the conventional VF mechanisms can all be explained by the restitution

mechanism.

- d) Through simulations, we hypothesized that the anteroposterior gradient is an essential consideration in accounting for the T wave being concordant with QRS complex in the human ECG.

7.2 Limitations and future work

Although simulation work was elaborately designed and carefully carried out, a lot of aspects were overlooked or simplified, and should be improved in future work.

- a) All simulation work of this dissertation is based on the Wei–Harumi model, and it is possible that all results derived are model-dependent. The heart shape is fixed for all performed simulations. It is preferable to test the reliability and validity of these results in other whole-heart models.
- b) The longest simulation duration is 28 seconds. Although this time length is longer than the simulation time in some reported work [94, 109, 114] and comparable with VF duration in some clinical VF studies [169, 212], it is still relatively shorter comparing with the observation time in some animal experiments [163, 213] and some VF studies in human heart [162, 173]. VF may evolve into a different organization or terminate if simulation is run for a longer period. In future work, the simulation time should be extended to several minutes.
- c) It was assumed that the DI-dependent restitution curves are fixed as the function between DI and APD (or CV). However, animal experiments had shown that for one certain DI, its corresponding ensuing APD was not determined [30]. Thus such assumption is not fully consistent with the real situation, and may influence fidelity of the results.
- d) In the simulations of VF study, the used APDR and CVR curves were acquired from different studies, so arbitrary combinations of these properties may be unrealistic. In addition, only heterogeneity of the APDR was considered in our simulations, but a novel technique has revealed considerable heterogeneity in

- CVR [10, 11] which is not included in the simulations.
- e) Since the heart model is made up by discrete model cells of finite number and lacks intercellular currents, discretization error may occur. For example, the excitation moment map in Figure 5.3A looks noisy at the first glimpse. Nevertheless, it is unlikely that the simulation reasonability is affected by the noises, because the simulated ECG has comparable waveforms and similar frequency band with the clinical observations, indicating that the simulated cardiac electrical activities well reproduced the VF behaviors in vivo, and the overall simulation results are still reliable and trustworthy.
 - f) It is worth stressing that restitution is not the only determinant of VF dynamics, and other factors may also play an important role [12]. Some omitted alterations, e.g. the increased gap-junction resistance and fibrotic/necrotic tissues may also affect the VF organizations.
 - g) For the work in Chapter 6, there are also several limitations. First, configurations of the four APD gradients used were somewhat simplified. Second, a realistic T wave is generated in a beating heart; however, our heart model does not simulate the movement of cardiac muscle. Third, simulations only took influence of the APD dispersion into account; however, the actin potential morphology may also affect the T wave. Fourth, we used the T-wave amplitude as the only parameter for comparison without considering other indices of ventricular repolarization dispersion, e.g., the T-wave peak-to-end interval and the total energy of the T wave [41]

The effect of these limitations remains unclear, and shall be investigated in future work. The contributions done in this dissertation is an extension of previous VF studies using the Wei–Harumi whole-heart model. There is still a long way to go before we fully understand the mystery of VF.

Acknowledgements

Study in University of Aizu is a journey of harvest, not only because of the rich knowledge I have absorbed, but also the sincere friendship, the virtue, the truth, kindness and beauty of the humanity I am blessed to feel.

I would like to express my most sincere gratitude to my former advisor, Prof. Daming Wei. My entire research is based on the heart model he created. His creative ideas, great wisdom and abundant knowledge helped me to achieve many academic breakthroughs. His care and concern for me is throughout my post-graduate program in University of Aizu. When I failed to graduate from University of Aizu in 2011, it was because of Prof. Wei's inspiring encouragement and kind help, I could have the opportunity to continue my study and finally make my dream come true.

I am deeply indebted to my current advisors, Prof. Wenxi Chen. His generous taking me over after Prof. Wei's retirement and constant guidance are the keys to my doctoral degree. His careful reading and thoughtful commenting on journal manuscripts considerably facilitated the publication process. I am also very grateful to him for instructing me to prepare my dissertation defense.

My special thanks are to Prof. Xin Zhu. He provided me many precious and valuable suggestions and ideas to me that solved a lot of research problems. I really appreciate his energetic mind and great academic ability. His professional modifications and polishing to my manuscripts have greatly improved the quantity and level of these papers.

I am also honored to have Prof. Zuxiang Fang and Prof. Jianguo Yu as my advisors at Fudan University. I really thank them for their unselfish inculcations of knowledge, patient guidance and timely encouragements. I am very fortunate to have four masters as my advisors, and I have learned countless knowledge and virtue from them, which is definitely the largest treasure of my life time.

I am really lucky to have Prof. Tuan Duc Pham and Prof. Yasuhiro Hisada as my dissertation review referees. I sincerely thank them for reviewing my dissertation very

carefully and providing me many precious comments to improve my dissertation.

I greatly appreciate my parents and girlfriend for always being at my side. I would like thank Dr. Weijia Lu for his academic advises. I also would like thank Ms. Mashiko, Dr. Shizhong Yuan, Dr. Wenfeng Shen, Dr. Xiaoling Zhou, Dr. Ying Chen, Mr. Zhaoqin Liu and Dr. Ming Huang for their kind helps. I sincerely thank all my friends in Biomedical Information Technology Laboratory, University of Aizu and Electrophysiology and Pacing Laboratory, Fudan University as well as Medtronic (Shanghai) Management Co., Ltd. I thank the financial support from University of Aizu. I thank all the persons that helped and encouraged me. Thank you all, I can never make it without your great help and support. I always owe you one.

References

- [1] R.J. Myerburg. Sudden Cardiac Death: Exploring the Limits of Our Knowledge. *J Cardiovasc Electrophysiol*, 2001, 12(3): 369-381
- [2] E. Braunwald, D.P. Zipes and P. Libby. Heart disease: a textbook of cardiovascular medicine. Philadelphia: WB Saunders Company, 2001
- [3] E.D. Engelstein and D.P. Zipes. Sudden cardiac death. In: R. W. Alexander, R. C. Schlant and V. Fuster. The Heart, Arteries and Veins. New York: McGraw-Hill, 1998: 1081-1112
- [4] Vital and Health Statistics Division. Vital Statistics in Japan - The latest Trends. Japan Ministry of Health, Labour and Welfare. 2010-10-24
- [5] Fire and Disaster Management Agency. Statistics of Cardiopulmonary Resuscitation (2008). Japan Ministry of Internal Affairs and Communications. 2008-12-15
- [6] M.E. Zevitz. Ventricular Fibrillation. Medscape Reference. 2010-11-12
- [7] A.S. Adabag, R.V. Luepker, V.L. Roger and B.J. Gersh. Sudden cardiac death: epidemiology and risk factors. *Nature*, 2010, 7(4): 216-225
- [8] D.M.E. Robles, R. Bernard, P. Coumel, A.N. Damato, C. Fisch, D. Krikler, N.A. Mazur, F.L. Meijler, L. Mogensen, P. Moret, Z. Pisa and H.J. Wellens. Definition of terms related to cardiac rhythm. WHO/ISFC Task Force. *Eur J Cardiol*, 1978, 8(2): 127-144
- [9] J.E. Erichsen. On the influence of the coronary circulation on the action of the heart. *Lond Mag Gazette*, 1842, 2: 561-565
- [10] P.B. Tabereaux, D.J. Dossall and R.E. Ideker. Mechanisms of VF maintenance: Wandering wavelets, mother rotors, or foci. *Heart Rhythm*, 2009, 6(3): 405-415
- [11] N.A. Trayanova. The Long and the Short of Long and Short Duration Ventricular Fibrillation. *Circ Res*, 2008, 102(10): 1151-1152
- [12] R.H. Clayton and A.V. Panfilov. A guide to modelling cardiac electrical activity in anatomically detailed ventricles. *Prog Biophys Mol Bio*, 2007, 96(1-3):

19-43

- [13] D. Wei. Whole heart modeling progress principles and applications. *Prog Biophys Mol Bio*, 1997, 67(1): 17-66
- [14] K.H.W.J. ten Tusscher, R. Hren and A.V. Panfilov. Organization of Ventricular Fibrillation in the Human Heart. *Circ Res*, 2007, 100(12): e87-e101
- [15] E.M. Cherry and F.H. Fenton. Visualization of spiral and scroll waves in simulated and experimental cardiac tissue. *New J Phys*, 2008, 10(12): 125016-125043
- [16] N. Kumaraswamy, P.W. Gregory, M. Sharon, M.R. Jack, W.K. Matthew, M.S. William, E.I. Raymond and H. William. Epicardial organization of human ventricular fibrillation. *Heart Rhythm*, 2004, 1(1): 14-23
- [17] G.P. Walcott, G.N. Kay, V.J. Plumb, W.M. Smith, J.M. Rogers, A.E. Epstein and R.E. Ideker. Endocardial wave front organization during ventricular fibrillation in humans. *J Am Coll Cardiol*, 2002, 39(1): 109-115
- [18] S. Masse, E. Downar, V. Chauhan, E. Sevaptsidis and K. Nanthakumar. Ventricular fibrillation in myopathic human hearts: mechanistic insights from in vivo global endocardial and epicardial mapping. *Am J Physiol Heart Circ Physiol*, 2007, 292(6): H2589-H2597
- [19] J.M. Rogers, G.P. Walcott, J.D. Gladden, S.B. Melnick and M.W. Kay. Panoramic Optical Mapping Reveals Continuous Epicardial Reentry during Ventricular Fibrillation in the Isolated Swine Heart. *Biophys J*, 2007, 92(3): 1090-1095
- [20] L. Li, Q. Jin, J. Huang, K. Cheng and R.E. Ideker. Intramural Foci During Long Duration Fibrillation in the Pig Ventricle. *Circ Res*, 2008, 102(10): 1256-1264
- [21] J.L. Byars, W.M. Smith, R.E. Ideker and V.G. Fast. Development of an Optrode for Intramural Multisite Optical Recordings of Vm in the Heart. *J Cardiovasc Electrophysiol*, 2003, 14(11): 1196-1202
- [22] M.P. Nash and A.V. Panfilov. Electromechanical model of excitable tissue to study reentrant cardiac arrhythmias. *Prog Biophys Mol Bio*, 2004, 85(2-3): 501-522
- [23] A.J. Compton and B.T. Patel. Simulating a whole patient for class teaching. In: *Simulation in Medicine (Ref. No. 1998/256)*, IEE Colloquium on. London: IET, 1998:

1-5

- [24] Medmovie.com. Cardiac illustration/HrtOrientation. 2004-01-22
- [25] Starsandseas.com. HeartChambers. 2010-12-02
- [26] R.M. Berne and M.N. Levy. Cardiovascular Physiology (8th edn). St. Louis, MO, USA: Mosby, 2001
- [27] P.N. Jordan and D.J. Christini. Therapies for Ventricular Cardiac Arrhythmias. *Crit Rev Biomed Eng*, 2005, 33(6): 557-604
- [28] P. Kohl. Heterogeneous Cell Coupling in the Heart: An Electrophysiological Role for Fibroblasts. *Circ Res*, 2003, 93(5): 381-383
- [29] D.M. Bers. Cardiac excitation-contraction coupling. *Nature*, 2002, 415(6868): 198-205
- [30] R.A. Li, G.F. Tomaselli and E. Marban. Structural and molecular bases of ion channel function. In: Douglas P. Zipes and Jose Jalife. Cardiac Electrophysiology: From Cell to Bedside, Fourth Edition. Philadelphia, Pa: W.B. Saunders, 2004
- [31] A.G. Kleber and Y. Rudy. Basic Mechanisms of Cardiac Impulse Propagation and Associated Arrhythmias. *Physiol Rev*, 2004, 84(2): 431-488
- [32] K.H.W.J. ten Tusscher and A.V. Panfilov. Alternans and spiral breakup in a human ventricular tissue model. *Am J Physiol Heart Circ Physiol*, 2006, 291(3): H1088-H1100
- [33] M. Firouzi and W.A. Groenewegen. Gene polymorphisms and cardiac arrhythmias. *Europace*, 2003, 5(3): 235-242
- [34] C.E. Conrath, R. Wilders, R. Coronel, B.J. de, P. Taggart, G.J. de and T. Opthof. Intercellular coupling through gap junctions masks M cells in the human heart. *Cardiovasc Res*, 2004, 62(2): 407-414
- [35] W.R. Loewenstein. Junctional intercellular communication: the cell-to-cell membrane channel. *Physiol Rev*, 1981, 61(4): 829-913
- [36] J.N. Weiss, P.S. Chen, Z. Qu, H.S. Karagueuzian and A. Garfinkel. Ventricular Fibrillation : How Do We Stop the Waves From Breaking? *Circ Res*, 2000, 87(12): 1103-1107
- [37] E. Cytrynbaum and J.P. Keener. Stability conditions for the traveling pulse:

- Modifying the restitution hypothesis. *Chaos*, 2002, 12(3): 788-799
- [38] Biologycorner.com. PQRST complex and relevant electrical activity. 2010-12-13
- [39] S. Dixit and D.J. Callans. Mapping for Ventricular Tachycardia. *Card Electrophysiol Rev*, 2002, 6(4): 436-441
- [40] G. Yan, R.S. Lankipalli, J.F. Burke, S. Musco and P.R. Kowey. Ventricular repolarization components on the electrocardiogram: Cellular basis and clinical significance. *J Am Coll Cardiol*, 2003, 42(3): 401-409
- [41] J. Malmivuo and R. Plonsey. Bioelectromagnetism: Principles and applications of bioelectric and biomagnetic fields. New York: Oxford University Press, 1995
- [42] F.H. Fenton, E.M. Cherry and L. Glass. Cardiac arrhythmia. *Scholarpedia*. 2008-07-10
- [43] R.M. Hoffman BF. Cellular mechanisms for cardiac arrhythmias. *Circ Res*, 1981, 49(1): 1-15
- [44] M.T. Keating and M.C. Sanguinetti. Molecular and Cellular Mechanisms of Cardiac Arrhythmias. *Cell*, 2001, 104(4): 569-580
- [45] Y. Rudy. Reentry: Insights From Theoretical Simulations in a Fixed Pathway. *J Cardiovasc Electrophysiol*, 1995, 6(4): 294-312
- [46] E.M. Aliot, W.G. Stevenson, J.M. Almendral-Garrote, F. Bogun, C.H. Calkins, E. Delacretaz, P.D. Bella, G. Hindricks, P. Ja š, M.E. Josephson, J. Kautzner, G.N. Kay, K. Kuck, B.B. Lerman, F. Marchlinski, V. Reddy, M. Schaliij, R. Schilling, K. Soejima and D. Wilber. EHRA/HRS Expert Consensus on Catheter Ablation of Ventricular Arrhythmias: Developed in a partnership with the European Heart Rhythm Association (EHRA), a Registered Branch of the European Society of Cardiology (ESC), and the Heart Rhythm Society (HRS); in collaboration with the American College of Cardiology (ACC) and the American Heart Association (AHA). *Europace*, 2009, 11(6): 771-817
- [47] C. de Chillou, D. Lacroix, D. Klug, I. Magnin-Poull, C. Marquie, M. Messier, M. Andronache, C. Kouakam, N. Sadoul, J. Chen, E. Aliot and S. Kacet. Isthmus Characteristics of Reentrant Ventricular Tachycardia After Myocardial Infarction.

- Circulation*, 2002, 105(6): 726-731
- [48] G.K. Moe. On the multiple wavelet hypothesis of AF. *Arch Int Pharmacodyn Ther*, 1962, 140(4): 183-188
- [49] J. Jalife. Ventricular Fibrillation: Mechanisms of Initiation and Maintenance. *Annu Rev Physiol*, 2000, 62(1): 25-50
- [50] A.V. Panfilov and A. Pertsov. Ventricular fibrillation: evolution of the multiple-wavelet hypothesis. *Phil Trans R Soc Lond A*, 2001, 359(1783): 1315-1325
- [51] F.H. Samie, O. Berenfeld, J. Anumonwo, S.F. Mironov, S. Udassi, J. Beaumont, S. Taffet, A.M. Pertsov and J. Jalife. Rectification of the Background Potassium Current: A Determinant of Rotor Dynamics in Ventricular Fibrillation. *Circ Res*, 2001, 89(12): 1216-1223
- [52] B. Choi, T. Liu and G. Salama. Letter to the Editor: Ventricular Fibrillation: Mother Rotor or Multiple Wavelets? *Circ Res*, 2001, 89(4): e30
- [53] B. Choi, T. Liu and G. Salama. The Distribution of Refractory Periods Influences the Dynamics of Ventricular Fibrillation. *Circ Res*, 2001, 88(5): e49-e58
- [54] J.C. Newton, W.M. Smith and R.E. Ideker. Estimated Global Transmural Distribution of Activation Rate and Conduction Block During Porcine and Canine Ventricular Fibrillation. *Circ Res*, 2004, 94(6): 836-842
- [55] R.E. Ideker and J. Huang. Our Search for the Porcine Mother Rotor. *Ann noninvas Electro*, 2005, 10(s4): 7-15
- [56] M.P. Nash, A. Mourad, R.H. Clayton, P.M. Sutton, C.P. Bradley, M. Hayward, D.J. Paterson and P. Taggart. Evidence for Multiple Mechanisms in Human Ventricular Fibrillation. *Circulation*, 2006, 114(6): 536-542
- [57] H.N. Pak, G.I. Kim, H.E. Lim, Y.H. Fang, J.I. Choi, J.S. Kim, C. Hwang and Y.H. Kim. Both Purkinje cells and left ventricular posteroseptal reentry contribute to the maintenance of ventricular fibrillation in open-chest dogs and swine: effects of catheter ablation and the ventricular cut-and-sew operation. *Circ J*, 2008, 72(7): 1185-1192
- [58] J.B. Nolasco and R.W. Dahlen. A graphic method for the study of alternation in cardiac action potentials. *J Appl Physiol*, 1968, 25(2): 191-196

- [59] J.N. Weiss, A. Karma, Y. Shiferaw, P.S. Chen, A. Garfinkel and Z. Qu. From Pulsus to Pulseless: The Saga of Cardiac Alternans. *Circ Res*, 2006, 98(10): 1244-1253
- [60] Z. Qu, A. Garfinkel, P.S. Chen and J.N. Weiss. Mechanisms of Discordant Alternans and Induction of Reentry in Simulated Cardiac Tissue. *Circulation*, 2000, 102(14): 1664-1670
- [61] L.D. Wilson and D.S. Rosenbaum. Mechanisms of arrhythmogenic cardiac alternans. *Europace*, 2007, 9(suppl_6): i77-i82
- [62] M.L. Koller, M.L. Riccio and R.F. Jr. Dynamic restitution of action potential duration during electrical alternans and ventricular fibrillation. *Am J Physiol Heart Circ Physiol*, 1998, 275(5): H1635-H1642
- [63] M. Courtemanche, J.P. Keener and L. Glass. A Delay Equation Representation of Pulse Circulation on a Ring in Excitable Media. *Siam J Appl Math*, 1996, 56(1): 119-142
- [64] J.N. Weiss, A. Garfinkel, H.S. Karagueuzian, Z. Qu and P. Chen. Chaos and the Transition to Ventricular Fibrillation : A New Approach to Antiarrhythmic Drug Evaluation. *Circulation*, 1999, 99(21): 2819-2826
- [65] O. Berenfeld and J. Jalife. Purkinje-Muscle Reentry as a Mechanism of Polymorphic Ventricular Arrhythmias in a 3-Dimensional Model of the Ventricles. *Circ Res*, 1998, 82(10): 1063-1077
- [66] I.R. Efimov, V.P. Nikolski and G. Salama. Optical Imaging of the Heart. *Circ Res*, 2004, 95(1): 21-33
- [67] A.R. Gelzer, M.L. Koller, N.F. Otani, J.J. Fox, M.W. Enyeart, G.J. Hooker, M.L. Riccio, C.R. Bartoli and R.F. Gilmour. Dynamic Mechanism for Initiation of Ventricular Fibrillation In Vivo. *Circulation*, 2008, 118(11): 1123-1129
- [68] Y.C. Hsieh, T.L. Horng, S.F. Lin, T.C. Lin, C.T. Ting and T.J. Wu. d,l-Sotalol at therapeutic concentrations facilitates the occurrence of long-lasting non-stationary reentry during ventricular fibrillation in isolated rabbit hearts. *Circ J*, 2009, 73(1): 39-47
- [69] M.L. Riccio, M.L. Koller and R.F.J. Gilmour. Electrical Restitution and

- Spatiotemporal Organization During Ventricular Fibrillation. *Circ Res*, 1999, 84(8): 955-963
- [70] E.M. Cherry and F.H. Fenton. Suppression of alternans and conduction blocks despite steep APD restitution: electrotonic, memory, and conduction velocity restitution effects. *Am J Physiol Heart Circ Physiol*, 2004, 286(6): H2332-H2341
- [71] J.N. Weiss, Z. Qu, P.S. Chen, S.F. Lin, H.S. Karagueuzian, H. Hayashi, A. Garfinkel and A. Karma. The Dynamics of Cardiac Fibrillation. *Circulation*, 2005, 112(8): 1232-1240
- [72] J. Weiss, P.S. Chen, T.J. Wu, C. Siegerman and A. Garfinkel. Ventricular Fibrillation: New Insights into Mechanisms. *Ann Ny Acad Sci*, 2004, 1015(1): 122-132
- [73] N.F. Otani. Theory of action potential wave block at-a-distance in the heart. *Phys Rev E*, 2007, 75(2): 21910, 17 pages
- [74] J.M. Cao, Z. Qu, Y.H. Kim, T.J. Wu, A. Garfinkel, J.N. Weiss, H.S. Karagueuzian and P.S. Chen. Spatiotemporal Heterogeneity in the Induction of Ventricular Fibrillation by Rapid Pacing: Importance of Cardiac Restitution Properties. *Circ Res*, 1999, 84(11): 1318-1331
- [75] T.J. Wu, S.F. Lin, J.N. Weiss, C.T. Ting and P.S. Chen. Two Types of Ventricular Fibrillation in Isolated Rabbit Hearts: Importance of Excitability and Action Potential Duration Restitution. *Circulation*, 2002, 106(14): 1859-1866
- [76] Y.B. Liu, H.N. Pak, S.T. Lamp, Y. Okuyama, H. Hayashi, T.J. Wu, J.N. Weiss, P.S. Chen and S.F. Lin. Coexistence of Two Types of Ventricular Fibrillation During Acute Regional Ischemia in Rabbit Ventricle. *J Cardiovasc Electrophysiol*, 2004, 15(12): 1433-1440
- [77] R.E. Ideker, J. Rogers and J. Huang. Types of Ventricular Fibrillation: 1,2,4,5 or 300,000? *J Cardiovasc Electrophysiol*, 2004, 15(12): 1441-1443
- [78] T.J. Wu, S.F. Lin, A. Baher, Z. Qu, A. Garfinkel, J.N. Weiss, C.T. Ting and P.S. Chen. Mother Rotors and the Mechanisms of D600-Induced Type 2 Ventricular Fibrillation. *Circulation*, 2004, 110(15): 2110-2118
- [79] X.W. Han, Y. Chen, W.H. Gao, J. Xue, X.D. Han, Z.X. Fang, C.W. Yang and

- X.M. Wu. Study of the restitution of action potential duration using the artificial neural network. *Math Biosci*, 2007, 207(1): 78-88
- [80] J. Beaumont, N. Davidenko, J.M. Davidenko and J. Jalife. Spiral waves in two-dimensional models of ventricular muscle: formation of a stationary core. *Biophys J*, 1998, 75(1): 1-14
- [81] A.V. Panfilov. Three-dimensional organization of electrical turbulence in the heart. *Phys Rev E*, 1999, 59(6): R6251-R6254
- [82] D. Wei, O. Okazaki, K. Harumi, E. Harasawa and H. Hosaka. Comparative Simulation of Excitation and Body Surface Electrocardiogram with Isotropic and Anisotropic Computer Heart Models. *IEEE Trans Biomed Eng*, 1995, 42(4): 343-357
- [83] D. Wei, O. Okazaki, K. Harumi, E. Harasawa and T. Musha. Inducing And Suppressing Ventricular Fibrillation: A Simulation Study With Three-Dimensional Heart Model And Experimental Data. In: J. P. Morucci, R. Plonsey and J. L. Coatrieux, *et al.* Proceedings of the 14th Annual International Conference of IEEE Engineering in Medicine and Biology Society. Paris, France: IEEE Press, 1992: 400-402
- [84] D. Wei, E. Harasawa, O. Okazaki, K. Harumi and T. Musha. Computer simulation of cardiac arrhythmias by incorporating phase response curve to a three-dimensional heart model. In: Robert Werner. Proceedings of Computers in Cardiology. Durham, NC: IEEE Computer Society Press, 1992: 327-330
- [85] T. Watanabe, M. Yamaki, S. Yamauchi, O. Minamihaba, T. Miyashita, I. Kubota and H. Tomoike. Regional prolongation of ARI and altered restitution properties cause ventricular arrhythmia in heart failure. *Am J Physiol Heart Circ Physiol*, 2002, 282(1): H212-H218
- [86] M. Yamaki, T. Watanabe, K. Yuuki, S. Yamauchi, Y. Hosoya and I. Kubota. Altered regional restitution properties cause ventricular arrhythmia. *IJBEM*, 2004, 6(1): 58-63
- [87] P.S. Chen, T.J. Wu, C.T. Ting, H.S. Karagueuzian, A. Garfinkel, S.F. Lin and J.N. Weiss. A Tale of Two Fibrillations. *Circulation*, 2003, 108(19): 2298-2303
- [88] A.L. Hodgkin and A.F. Huxley. A quantitative description of membrane

- current and its application to conduction and excitation in nerve. *J Physiol*, 1952, 117(4): 500-544
- [89] www.cellml.org. The CellML project
- [90] A. Garny, D. Noble, P.J. Hunter and P. Kohl. Cellular Open Resource (COR): current status and future directions. *Philos T Roy Soc A*, 2009, 367(1895): 1885-1905
- [91] K.H.W.J. ten Tusscher, O. Bernus, R. Hren and A.V. Panfilov. Comparison of electrophysiological models for human ventricular cells and tissues. *Prog Biophys Mol Bio*, 90(1-3): 326-345
- [92] F.H. Fenton and E.M. Cherry. Models of cardiac cell. *scholarpedia*, 2008, 3(8): 1868
- [93] J. Beaumont, F.A. Roberge and L.J. Leon. On the interpretation of voltage-clamp data using the Hodgkin-Huxley Model. *Math Biosci*, 1993, 115(1): 65-101
- [94] R.H. Keldermann, K.H.W.J. ten Tusscher, M.P. Nash, C.P. Bradley, R. Hren, P. Taggart and A.V. Panfilov. A computational study of mother rotor VF in the human ventricles. *Am J Physiol Heart Circ Physiol*, 2009, 296(2): H370-H379
- [95] M. Vaquero, D. Calvo and J. Jalife. Cardiac fibrillation: From ion channels to rotors in the human heart. *Heart Rhythm*, 2008, 5(6): 872-879
- [96] R. Plonsey. Bioelectric Phenomena. In: Duke University. Wiley Encyclopedia of Electrical and Electronics Engineering. Durham, NC: John Wiley & Sons, Inc., 2001
- [97] R. Clayton and P. Taggart. Regional differences in APD restitution can initiate wavebreak and re-entry in cardiac tissue: A computational study. *Biomed Eng Online*, 2005, 4(1): 54, 14 pages
- [98] T. Krogh-Madsen and D.J. Christini. Action Potential Duration Dispersion and Alternans in Simulated Heterogeneous Cardiac Tissue with a Structural Barrier. *Biophys J*, 2007, 92(4): 1138-1149
- [99] F. Xie, Z. Qu, A. Garfinkel and J.N. Weiss. Electrophysiological heterogeneity and stability of reentry in simulated cardiac tissue. *Am J Physiol Heart Circ Physiol*, 2001, 280(2): H535-H545

- [100] M.P. Nash, C.P. Bradley, P.M. Sutton, R.H. Clayton, P. Kallis, M.P. Hayward, D.J. Paterson and P. Taggart. Whole heart action potential duration restitution properties in cardiac patients: a combined clinical and modelling study. *Exp Physiol*, 2006, 91(2): 339-354
- [101] D.X. Tran, M.J. Yang, J.N. Weiss, A. Garfinkel and Z. Qu. Vulnerability to re-entry in simulated two-dimensional cardiac tissue: Effects of electrical restitution and stimulation sequence. *Chaos*, 2007, 17(4): 43111-43115
- [102] T. Ashihara, T. Namba, T. Ikeda, M. Ito, K. Nakazawa and N. Trayanova. Mechanisms of Myocardial Capture and Temporal Excitable Gap During Spiral Wave Reentry in a Bidomain Model. *Circulation*, 2004, 109(7): 920-925
- [103] S.W. Morgan, G. Plank, I.V. Biktasheva and V.N. Biktashev. Low energy defibrillation in human cardiac tissue: a simulation study. *Biophys J*, 2009, 96(4): 1364-1373
- [104] F.H. Fenton, E.M. Cherry, H.M. Hastings and S.J. Evans. Multiple mechanisms of spiral wave breakup in a model of cardiac electrical activity. *Chaos*, 2002, 12(3): 852-892
- [105] P. Colli Franzone, L.F. Pavarino and B. Taccardi. Effects of transmural electrical heterogeneities and electrotonic interactions on the dispersion of cardiac repolarization and action potential duration: A simulation study. *Math Biosci*, 2006, 204(1): 132-165
- [106] L.M. Popp, G. Seemann and O. Dossel. A simulation study of the reaction of human heart to biphasic electrical shocks. *BMC Cardiovasc Disord*, 2004, 4: 9, 14 pages
- [107] Z. Qu, J. Kil, F. Xie, A. Garfinkel and J.N. Weiss. Scroll Wave Dynamics in a Three-Dimensional Cardiac Tissue Model: Roles of Restitution, Thickness, and Fiber Rotation. *Biophys J*, 2000, 78(6): 2761-2775
- [108] R. Plonsey and R.C. Barr. Mathematical modeling of electrical activity of the heart. *J Electrocardiol*, 1987, 20(3): 219-226
- [109] F. Xie, Z. Qu, J. Yang, A. Baher, J.N. Weiss and A. Garfinkel. A simulation study of the effects of cardiac anatomy in ventricular fibrillation. *J Clin Invest*, 2004,

113(5): 686-693

[110] M.C. Trudel, B. Dube, M. Potse, R.M. Gulrajani and L.J. Leon. Simulation of QRST integral maps with a membrane-based computer heart model employing parallel processing. *IEEE Trans Biomed Eng*, 2004, 51(8): 1319-1329

[111] M. Lorange, R.M. Gulrajani, J. de Guise and P. Fortier. A whole-heart model incorporating myocardial anisotropy. In: Proceedings of the Annual International Conference of the IEEE Engineering in Medicine and Biology Society, 1988. New Orleans, LA, USA, 1988: 191-195

[112] D. Wei. Whole Heart Modeling and Computer Simulation. In: Bin He. Modeling and Imaging of Bioelectrical Activity: Springer US, 2005: 81-117

[113] D.L. Weiss, M. Ifland, F.B. Sachse, G. Seemann and O. Dössel. Modeling of cardiac ischemia in human myocytes and tissue including spatiotemporal electrophysiological variations. *Biomed Tech*, 2009, 54(3): 107-125

[114] R.H. Keldermann, K.H.W.J. ten Tusscher, M.P. Nash, R. Hren, P. Taggart and A.V. Panfilov. Effect of heterogeneous APD restitution on VF organization in a model of the human ventricles. *Am J Physiol Heart Circ Physiol*, 2008, 294(2): H764-H774

[115] K.J. Sampson and C.S. Henriquez. Electrotonic influences on action potential duration dispersion in small hearts: a simulation study. *Am J Physiol Heart Circ Physiol*, 2005, 289(1): H350-H360

[116] Y. Belhamadia, A. Fortin and Y. Bourgault. Towards accurate numerical method for monodomain models using a realistic heart geometry. *Math Biosci*, 2009, 220(2): 89-101

[117] M. Potse, B. Dube, J. Richer, A. Vinet and R.M. Gulrajani. A Comparison of Monodomain and Bidomain Reaction-Diffusion Models for Action Potential Propagation in the Human Heart. *IEEE Trans Biomed Eng*, 2006, 53(12): 2425-2435

[118] R.C.P. Kerckhoffs, F. Vadakkumpadan, V. Gurev, J. Constantino, H. Arevalo and N. Trayanova. Modeling of Whole-Heart Electrophysiology and Mechanics: Toward Patient-Specific Simulations. In: Roy C. P. Kerckhoffs. Patient-Specific Modeling of the Cardiovascular System. New York: Springer, 2010: 145-165

- [119] J. Relan, M. Sermesant, H. Delingette, M. Pop, G.A. Wright and N. Ayache. Quantitative comparison of two cardiac electrophysiology models using personalisation to optical and MR data. In: *Biomedical Imaging: From Nano to Macro*, 2009. ISBI '09. IEEE International Symposium on. Boston, MA: IEEE press, 2009: 1027-1030
- [120] I.E. Magnin, J. Montagnat, P. Clarysse, J. Nenonen, T. Katila, L. Geerts, R. Kerckhoffs, P. Bovendeerd and T. Arts. Towards Patient Specific Models of Cardiac Mechanics: A Sensitivity Study. In: Isabelle E. Magnin, Johan Montagnat and Patrick Clarysse, *et al.* *Functional Imaging and Modeling of the Heart*: Springer Berlin Heidelberg, 2003: 81-90
- [121] V. Fijoy, J.R. Lukas, T. Brock, B. Patrick, J.P. Anton, V. Edward, P. Gernot and T. Natalia. Image-based models of cardiac structure with applications in arrhythmia and defibrillation studies. *J Electrocardiol*, 2009, 42(2): 151-157
- [122] R.A. Burton, G. Plank, J.E. Schneider, V. Grau, H. Ahammer, S.L. Keeling, J. Lee, N.P. Smith, D. Gavaghan, N. Trayanova and P. Kohl. Three-Dimensional Models of Individual Cardiac Histoanatomy: Tools and Challenges. *Ann Ny Acad Sci*, 2006, 1080(1): 301-319
- [123] M. Sermesant, K. Rhode, G.I. Sanchez-Ortiz, O. Camara, R. Andriantsimiavona, S. Hegde, D. Rueckert, P. Lambiase, C. Bucknall, E. Rosenthal, H. Delingette, D.L.G. Hill, N. Ayache and R. Razavi. Simulation of cardiac pathologies using an electromechanical biventricular model and XMR interventional imaging. *Med Image Anal*, 2005, 9(5): 467-480
- [124] M. Sermesant, H. Delingette and N. Ayache. An electromechanical model of the heart for image analysis and simulation. *IEEE T Med Imaging*, 2006, 25(5): 612-625
- [125] E.J. Vigmond, C. Clements, D.M. McQueen and C.S. Peskin. Effect of bundle branch block on cardiac output: A whole heart simulation study. *Prog Biophys Mol Bio*, 2008, 97(2-3): 520-542
- [126] J.P. Whiteley. An Efficient Numerical Technique for the Solution of the Monodomain and Bidomain Equations. *IEEE Trans Biomed Eng*, 2006, 53(11):

2139-2147

[127] M. Bendahmane, R. Bürger and R. Ruiz-Baier. A multiresolution space-time adaptive scheme for the bidomain model in electrocardiology. *Numer Meth Part D E*, 2010, 26(6): 1377-1404

[128] D. Wei, M. Aoki, Y. Okamoto, T. Musha and K. Harumi. Computer simulation of the Wolff-Parkinson-White syndrome utilizing a human heart model. *Jpn Heart J*, 1987, 28(5): 707-718

[129] D.M. Wei, G. Yamada, T. Musha, H. Tsunakawa, T. Tsutsumi and K. Harumi. Computer simulation of supraventricular tachycardia with the Wolff-Parkinson-White syndrome using three-dimensional heart models. *J Electrocardiol*, 1990, 23(3): 261-273

[130] E. Ryzhii and D. Wei. Computer simulation of atypical Brugada syndrome. *J Electrocardiol*, 2009, 42(4): 319-327

[131] O. Okazaki, D. Wei and K. Harumi. A simulation study of torsade de pointes with m cells. *J Electrocardiol*, 1998, 31: 145-151

[132] W. Shen, D. Wei, W. Xu, X. Zhu and S. Yuan. Parallelized computation for computer simulation of electrocardiograms using personal computers with multi-core CPU and general-purpose GPU. *Comput. Methods Prog. Biomed.*, 2010, 100(1): 87-96

[133] X. Zhu, D. Wei and O. Okazaki. Computer Simulation of Clinical Electrophysiological Study. *PACE*, 2012, 35(6): 718-729

[134] A.N. Drury. THE EFFECTIVE REFRACTORY PERIOD, FULL RECOVERY TIME, AND PREMATURE RESPONSE INTERVAL OF VENTRICULAR MUSCLE IN THE INTACT UNANAESTHETISED CAT AND RABBIT. *Exp Physiol*, 1936, 26(2): 181-200

[135] S. Sircar. Principles of Medical Physiology. New York: Thieme Stuttgart, 2008

[136] C.S. Henriquez. Simulating the electrical behavior of cardiac tissue using the bidomain model. *Crit Rev Biomed Eng*, 1993, 21(1): 1-77

[137] D. Wei. Whole-heart modeling and simulation. In: Bin He. Modeling and imaging of bioelectrical activity: principles and applications. Norwell, USA: Kluwer

Academic, 2004: 81-117

[138] D. Wei and S. Mashima. Prediction of Accessory Pathway Locations in Wolff-Parkinson-White Syndrome with Body Surface Potential Laplacian Maps: A Simulation Study. *Jpn Heart J*, 1999, 40(4): 451-459

[139] H.N. Pak, S.J. Hong, G.S. Hwang, H.S. Lee, S.W. Park, J.C. Ahn, Y. Moo Ro and Y.H. Kim. Spatial Dispersion of Action Potential Duration Restitution Kinetics Is Associated with Induction of Ventricular Tachycardia/Fibrillation in Humans. *J Cardiovasc Electrophysiol*, 2004, 15(12): 1357-1363

[140] R.J. Selvaraj, P. Picton, K. Nanthakumar and V.S. Chauhan. Steeper restitution slopes across right ventricular endocardium in patients with cardiomyopathy at high risk of ventricular arrhythmias. *Am J Physiol Heart Circ Physiol*, 2007, 292(3): H1262-H1268

[141] J.I. Goldhaber, L.H. Xie, T. Duong, C. Motter, K. Khuu and J.N. Weiss. Action Potential Duration Restitution and Alternans in Rabbit Ventricular Myocytes: The Key Role of Intracellular Calcium Cycling. *Circ Res*, 2005, 96(4): 459-466

[142] M.R. Franz and A. Costard. Frequency-dependent effects of quinidine on the relationship between action potential duration and refractoriness in the canine heart in situ. *Circulation*, 1988, 77(5): 1177-1184

[143] M.R. Franz, D. Burkhoff, H. Spurgeon, M.L. Weisfeldt and E.G. Lakatta. In vitro validation of a new cardiac catheter technique for recording monophasic action potentials. *Eur Heart J*, 1986, 7(1): 34-41

[144] Z. Qu. Nonlinear dynamic control of irregular cardiac rhythms. *J Cardiovasc Electrophysiol*, 2004, 15(10): 1186-1187

[145] M.L. Walker and D.S. Rosenbaum. Repolarization alternans: implications for the mechanism and prevention of sudden cardiac death. *Cardiovasc Res*, 2003, 57(3): 599-614

[146] O. Voroshilovsky, Z. Qu, M.H. Lee, T. Ohara, G.A. Fishbein, H.L. Huang, C.D. Swerdlow, S.F. Lin, A. Garfinkel, J.N. Weiss, H.S. Karagueuzian and P.S. Chen. Mechanisms of Ventricular Fibrillation Induction by 60-Hz Alternating Current in Isolated Swine Right Ventricle. *Circulation*, 2000, 102(13): 1569-1574

- [147] O.H. Tovar and J.L. Jones. Electrophysiological Deterioration During Long-Duration Ventricular Fibrillation. *Circulation*, 2000, 102(23): 2886-2891
- [148] W. Kong, R.E. Ideker and V.G. Fast. Transmural optical measurements of Vm dynamics during long-duration ventricular fibrillation in canine hearts. *Heart Rhythm*, 2009, 6(6): 796-802
- [149] A. Casaleggio, B. Gramatikov and N.V. Thakor. Dynamic differences between ventricular fibrillation types induced in human patients by different types of stimulation. In: *Computers in Cardiology 1997*. 1997: 89-92
- [150] Y. Aizawa, N. Naitoh, T. Washizuka, K. Takahashi, H. Uchiyama, M. Shiba and A. Shibata. Electrophysiological Findings in Idiopathic Recurrent Ventricular Fibrillation: Special Reference to Mode of Induction, Drug Testing, and Long-Term Outcomes. *PACE*, 1996, 19(6): 929-939
- [151] Y. Zheng, D. Wei and Z. Fang. Steeper Action Potential Duration Restitution Slope Increases Risk of Ventricular Fibrillation: A simulation Study. In: *The 4th International Conference on Bioinformatics and Biomedical Engineering*. Chengdu, China, 2010, Paper ID:1011178, CDROM, 4 pages
- [152] S.M. Narayan, M.R. Franz, G. Lalani, J. Kim and A. Sastry. T-Wave Alternans, Restitution of Human Action Potential Duration, and Outcome. *J Am Coll Cardiol*, 2007, 50(25): 2385-2392
- [153] A.M. Pitruzzello, W. Krassowska and S.F. Idriss. Spatial heterogeneity of the restitution portrait in rabbit epicardium. *AJP - Heart and Circulatory Physiology*, 2007, 292(3): H1568-H1578
- [154] F.H. Samie and J. Jalife. Mechanisms underlying ventricular tachycardia and its transition to ventricular fibrillation in the structurally normal heart. *Cardiovasc Res*, 2001, 50(2): 242-250
- [155] J.S. Allison, H. Qin, D.J. Dossall, J. Huang, J.C. Newton, J.D. Allred, W.M. Smith and R.E. Ideker. The Transmural Activation Sequence in Porcine and Canine Left Ventricle Is Markedly Different During Long-Duration Ventricular Fibrillation. *J Cardiovasc Electrophysiol*, 2007, 18(12): 1306-1312
- [156] K. Endresen and J.P. Amlie. Electrical Restitution and Conduction Intervals of

Ventricular Premature Beats in Man: Influence of Heart Rate. *PACE*, 1989, 12(8): 1347-1354

[157] B.S. Koller, P.E. Karasik, A.J. Solomon and M.R. Franz. Relation Between Repolarization and Refractoriness During Programmed Electrical Stimulation in the Human Right Ventricle: Implications for Ventricular Tachycardia Induction. *Circulation*, 1995, 91(9): 2378-2384

[158] A.M. Yue, M.R. Franz, P.R. Roberts and J.M. Morgan. Global Endocardial Electrical Restitution in Human Right and Left Ventricles Determined by Noncontact Mapping. *J Am Coll Cardiol*, 2005, 46(6): 1067-1075

[159] A.M. Yue, J.R. Paisey, S. Robinson, T.R. Betts, P.R. Roberts and J.M. Morgan. Determination of Human Ventricular Repolarization by Noncontact Mapping: Validation With Monophasic Action Potential Recordings. *Circulation*, 2004, 110(11): 1343-1350

[160] C.W. Haws and R.L. Lux. Correlation between in vivo transmembrane action potential durations and activation-recovery intervals from electrograms. Effects of interventions that alter repolarization time. *Circulation*, 1990, 81(1): 281-288

[161] J.M. Herre, D.E. Mann, J.C. Luck, S.A. Magro, S. Figali, T. Breen and C.R. Wyndham. Effect of increased current, multiple pacing sites and number of extrastimuli on induction of ventricular tachycardia. *Am J Cardiol*, 1986, 57(1): 102-107

[162] S. Masse, T. Farid, P. Dorian, K. Umapathy, K. Nair, J. Asta, H. Ross, V. Rao, E. Sevaptisidis and K. Nanthakumar. Effect of global ischemia and reperfusion during ventricular fibrillation in myopathic human hearts. *Am J Physiol Heart Circ Physiol*, 2009, 297(6): H1984-H1991

[163] J.F. Huizar, M.D. Warren, A.G. Shvedko, J. Kalifa, J. Moreno, S. Mironov, J. Jalife and A.V. Zaitsev. Three distinct phases of VF during global ischemia in the isolated blood-perfused pig heart. *Am J Physiol Heart Circ Physiol*, 2007, 293(3): H1617-H1628

[164] G. Salama and B.R. Choi. Imaging ventricular fibrillation. *J Electrocardiol*, 2007, 40(6 Suppl): S56-S61

- [165] N.A. Lever, E.G. Newall and P.D. Larsen. Differences in the characteristics of induced and spontaneous episodes of ventricular fibrillation. *Europace*, 2007, 9(11): 1054-1058
- [166] S. Viskin and B. Belhassen. Idiopathic Ventricular Fibrillation. In: Ihor Gussak, Charles Antzelevitch and Arthur A. M. Wilde, *et al.* Electrical Diseases of the Heart - Genetics, Mechanisms, Treatment, Prevention. London, UK: Springer, 2008: 588-603
- [167] H. Kasanuki, S. Ohnishi, M. Ohtuka, N. Matsuda, T. Nirei, R. Isogai, M. Shoda, Y. Toyoshima and S. Hosoda. Idiopathic Ventricular Fibrillation Induced With Vagal Activity in Patients Without Obvious Heart Disease. *Circulation*, 1997, 95(9): 2277-2285
- [168] M.L. Koller, S.K.G. Maier, A.R. Gelzer, W.R. Bauer, M. Meesmann and R.F.J. Gilmour. Altered Dynamics of Action Potential Restitution and Alternans in Humans With Structural Heart Disease. *Circulation*, 2005, 112(11): 1542-1548
- [169] G.D. Latcu, O. Meste, A. Duparc, P. Mondoly, A. Rollin, M. Delay and P. Maury. Temporal and spectral analysis of ventricular fibrillation in humans. *J Interv Card Electrophysiol*, 2011, 30(3): 199-209
- [170] A. Bueno-Orovio, B.M. Hanson, J.S. Gill, P. Taggart and B. Rodriguez. *In vivo* human left-to-right ventricular differences in rate adaptation transiently increase pro-arrhythmic risk following rate acceleration. *PLoS One*, 2012, 7(12): e52234, 12 pages
- [171] P.S. Spector, D.D. Correa De Sa, E.S. Tischler, N.C. Thompson, N. Habel, J. Stinnett-Donnelly, B.E. Benson, P. Bielau and J.H.T. Bates. Ablation of multi-wavelet re-entry: general principles and in silico analyses. *Europace*, 2012, 14(suppl 5): v106-v111
- [172] S. Ashino, I. Watanabe, M. Kofune, K. Nagashima, K. Ohkubo, Y. Okumura, H. Mano, T. Nakai, S. Kunimoto, Y. Kasamaki and A. Hirayama. Effects of Quinidine on the Action Potential Duration Restitution Property in the Right Ventricular Outflow Tract in Patients With Brugada Syndrome. *Circ J*, 2011, 75(9): 2080-2086
- [173] C.P. Bradley, R.H. Clayton, M.P. Nash, A. Mourad, M. Hayward, D.J. Paterson and P. Taggart. Human Ventricular Fibrillation During Global Ischemia and

- Reperfusion. *Circ Arrhythm Electrophysiol*, 2011, 4(5): 684-691
- [174] C.W. Zemlin and A.V. Panfilov. Spiral waves in excitable media with negative restitution. *Phys Rev E Stat Nonlin Soft Matter Phys*, 2001, 63(4 Pt 1): 41912, 4 pages
- [175] G. Bub, A. Shrier and L. Glass. Spiral wave generation in heterogeneous excitable media. *Phys Rev Lett*, 2002, 88(5): 58101, 4 pages
- [176] F. Alonso Atienza, J. Requena Carrion, A. Garcia Alberola, J.L. Rojo Alvarez, J.J. Sanchez Munoz, J. Martinez Sanchez and M. Valdes Chavarri. A Probabilistic Model of Cardiac Electrical Activity Based on a Cellular Automata System. *Rev Esp Cardiol*, 2005, 58(01): 41-47
- [177] O. Bandman. Simulating Spatial Dynamics by Probabilistic Cellular Automata. *Lect Notes Comput Sci*, 2002, 2493: 10-19
- [178] O. Bandman. Accuracy and Stability of Spatial Dynamics Simulation by Cellular Automata Evolution. *Lect Notes Comput Sci*, 2003, 2763: 20-34
- [179] O. Bandman. Computation properties of spatial dynamics simulation by probabilistic cellular automata. *Future Gener Comp Sy*, 2005, 21(5): 633-643
- [180] A. Nishiyama and T. Tokihiro. Construction of an Isotropic Cellular Automaton for a Reaction-Diffusion Equation by Means of a Random Walk. *J Phys Soc Jpn*, 2011, 80(5): 54003, 6 pages
- [181] K. Harumi, M.J. Burgess and J.A. Abildskov. A theoretic model of the T wave. *Circulation*, 1966, 34(4): 657-668
- [182] B. Benito, E. Guasch, L. Rivard and S. Nattel. Clinical and Mechanistic Issues in Early Repolarization: Of Normal Variants and Lethal Arrhythmia Syndromes. *J Am Coll Cardiol*, 2010, 56(15): 1177-1186
- [183] M. Haïssaguerre, N. Derval, F. Sacher, L. Jesel, I. Deisenhofer, L. de Roy, J. Pasquié, A. Nogami, D. Babuty, S. Yli-Mayry, C. De Chillou, P. Scanu, P. Mabo, S. Matsuo, V. Probst, S. Le Scouarnec, P. Defaye, J. Schlaepfer, T. Rostock, D. Lacroix, D. Lamaison, T. Lavergne, Y. Aizawa, A. Englund, F. Anselme, M. O'Neill, M. Hocini, K.T. Lim, S. Knecht, G.D. Veenhuyzen, P. Bordachar, M. Chauvin, P. Jais, G. Coureau, G. Chene, G.J. Klein and J. Clémenty. Sudden Cardiac Arrest Associated with Early Repolarization. *New Engl J Med*, 2008, 358(19): 2016-2023

- [184] D.S. Rosenbaum, P. Albrecht and R.J. Cohen. Predicting Sudden Cardiac Death From T Wave Alternans of the Surface Electrocardiogram: Promise and Pitfalls. *J Cardiovasc Electrophysiol*, 1996, 7(11): 1095-1111
- [185] N.V. Artyeva, S.L. Goshka, K.A. Sedova, O.G. Bernikova and J.E. Azarov. What does the Tpeak-Tend interval reflect? An experimental and model study. *J Electrocardiol*, 2013, 46(4): 291-296
- [186] B. Hanson, P. Sutton, N. Elameri, M. Gray, H. Critchley, J.S. Gill and P. Taggart. Interaction of Activation-Repolarization Coupling and Restitution Properties in Humans. *Circ Arrhythm Electrophysiol*, 2009, 2(2): 162-170
- [187] V.S. Chauhan, E. Downar, K. Nanthakumar, J.D. Parker, H.J. Ross, W. Chan and P. Picton. Increased ventricular repolarization heterogeneity in patients with ventricular arrhythmia vulnerability and cardiomyopathy: a human in vivo study. *Am J Physiol Heart Circ Physiol*, 2006, 290(1): H79-H86
- [188] D.E. Hurtado and E. Kuhl. Computational modelling of electrocardiograms: repolarisation and T-wave polarity in the human heart. *Comput Meth Biomech Biomed Eng*, 2012, 17(9): 986-996
- [189] J.M.T. de Bakker and T. Opthof. Is the Apico-basal Gradient Larger Than the Transmural Gradient? *J Cardiovasc Pharm*, 2002, 39(3): 328-331
- [190] P. Taggart, P.M.I. Sutton, T. Opthof, R. Coronel, R. Trimlett, W. Pugsley and P. Kallis. Transmural repolarisation in the left ventricle in humans during normoxia and ischaemia. *Cardiovasc Res*, 2001, 50(3): 454-462
- [191] D. Durrer, R.T. Van Dam, G.E. Freud, M.J. Janse, F.L. Meijler and R.C. Arzbaecher. Total Excitation of the Isolated Human Heart. *Circulation*, 1970, 41(6): 899-912
- [192] C. Patel, J.F. Burke, H. Patel, P. Gupta, P.R. Kowey, C. Antzelevitch and G. Yan. Is there a significant transmural gradient in repolarization time in the intact heart?: Cellular Basis of the T Wave: A Century of Controversy. *Circ Arrhythm Electrophysiol*, 2009, 2(1): 80-88
- [193] T. Opthof, R. Coronel and M.J. Janse. Is there a significant transmural gradient in repolarization time in the intact heart?: Repolarization Gradients in the Intact Heart.

Circ Arrhythm Electrophysiol, 2009, 2(1): 89-96

[194] M.J. Janse, R. Coronel, T. Opthof, E.A. Sosunov, E.P. Anyukhovskiy and M.R. Rosen. Repolarization gradients in the intact heart: Transmural or apico-basal? *Prog Biophys Mol Bio*, 2012, 109(1 - 2): 6-15

[195] J. Burdon-Sanderson and F.J.M. Page. On the Time-Relations of the Excitatory Process in the Ventricle of the Heart of the Frog. *J Physiol*, 1880, 2(5-6): 384-435

[196] G. Yan and C. Antzelevitch. Cellular Basis for the Normal T Wave and the Electrocardiographic Manifestations of the Long-QT Syndrome. *Circulation*, 1998, 98(18): 1928-1936

[197] B.H. Van Huysduyven, C.A. Swenne, H.H. Draisma, M.L. Antoni, H. Van De Vooren, E.E. Van Der Wall and M.J. Schalijs. Validation of ECG indices of ventricular repolarization heterogeneity: a computer simulation study. *J Cardiovasc Electrophysiol*, 2005, 16(10): 1097-1103

[198] J. Xue, Y. Chen, X. Han and W. Gao. Electrocardiographic morphology changes with different type of repolarization dispersions. *J Electrocardiol*, 2010, 43(6): 553-559

[199] J. Okada, T. Washio, A. Maehara, S. Momomura, S. Sugiura and T. Hisada. Transmural and apicobasal gradients in repolarization contribute to T-wave genesis in human surface ECG. *Am J Physiol Heart Circ Physiol*, 2011, 301(1): H200-H208

[200] J. Okada, T. Sasaki, T. Washio, H. Yamashita, T. Kariya, Y. Imai, M. Nakagawa, Y. Kadooka, R. Nagai, T. Hisada and S. Sugiura. Patient Specific Simulation of Body Surface ECG using the Finite Element Method. *PACE*, 2013, 36(3): 309-321

[201] D.L. Weiss, G. Seemann, D.U.J. Keller, D. Farina, F.B. Sachse and O. Dossel. Modeling of heterogeneous electrophysiology in the human heart with respect to ECG genesis. In: *Proceedings of Computers in Cardiology*. Durham, NC: IEEE Computer Society Press, 2007: 49-52

[202] D.U.J. Keller, D.L. Weiss, O. Dossel and G. Seemann. Influence of I_{Ks} Heterogeneities on the Genesis of the T-Wave: A Computational Evaluation. *IEEE Trans Biomed Eng*, 2012, 59(2): 311-322

- [203] P.D. Arini and E. Laciari. Quantification of Cardiac Ventricular Repolarization and its Spatial Dispersion through the Surface Electrocardiogram. *Rev Argent Cardiol*, 2009, 77(1): 47-55
- [204] C.L. Gambill, M.L. Wilkins, W.K. Haisty, S.T. Anderson, C. Maynard, N.B. Wagner, R.H. Startt Selvester and G.S. Wagner. T wave amplitudes in normal populations: Variation with ECG lead, sex, and age. *J Electrocardiol*, 1995, 28(3): 191-197
- [205] A.V. Glukhov, V.V. Fedorov, Q. Lou, V.K. Ravikumar, P.W. Kalish, R.B. Schuessler, N. Moazami and I.R. Efimov. Transmural Dispersion of Repolarization in Failing and Nonfailing Human Ventricle. *Circ Res*, 2010, 106(5): 981-991
- [206] D. Emmanuel, C. Flavien, G. Chantal, L. Karine and L.M. Herve. Electrophysiologic characteristics of cells spanning the left ventricular wall of human heart: Evidence for presence of M cells. *J Am Coll*, 1995, 26(1): 185-192
- [207] P. Taggart, P. Sutton, T. Opthof, R. Coronel and P. Kallis. Electrotonic cancellation of transmural electrical gradients in the left ventricle in man. *Prog Biophys Mol Bio*, 2003, 82(1-3): 243-254
- [208] E.P. Anyukhovskiy, E.A. Sosunov, R.Z. Gainullin and M.R. Rosen. The controversial M cell. *J Cardiovasc Electrophysiol*, 1999, 10(2): 244-260
- [209] T. Opthof, R. Coronel, M.J. Janse and M.R. Rosen. A wedge is not a heart. *Heart Rhythm*, 2007, 4(8): 1116-1119
- [210] M.D. Lesh, M. Pring and J.F. Spear. Cellular uncoupling can unmask dispersion of action potential duration in ventricular myocardium. A computer modeling study. *Circ Res*, 1989, 65(5): 1426-1440
- [211] C. Ramanathan, P. Jia, R. Ghanem, K. Ryu and Y. Rudy. Activation and repolarization of the normal human heart under complete physiological conditions. *Proc Natl Acad Sci*, 2006, 103(16): 6309-6314
- [212] S.C. Toal, T.A. Farid, R. Selvaraj, V.S. Chauhan, S. Masse, J. Ivanov, L. Harris, E. Downar, M.R. Franz and K. Nanthakumar. Short-Term Memory and Restitution During Ventricular Fibrillation in Human Hearts: An In Vivo Study. *Circ Arrhythm Electrophysiol*, 2009, 2(5): 562-570

[213] L. Li, X. Zheng, D.J. Dossall, J. Huang, S.M. Pogwizd and R.E. Ideker. Long-Duration Ventricular Fibrillation Exhibits 2 Distinct Organized States. *Circ Arrhythm Electrophysiol*, 2013, 6(6): 1192-1199